Enhancing the oxidation of Li_2O_2 in Li-O_2 batteries: Mechanistic and chemical efficacy probing

By

Koffi Pierre Claver Yao

Bachelor of Science, Mechanical Engineering, University of Delaware, 2010

Master of Science, Mechanical Engineering, Massachusetts Institute of Technology, 2013

Submitted to the Department of Mechanical Engineering in partial fulfillment of the requirements for the degree of

DOCTOR OF PHILOSOPHY IN MECHANICAL ENGINEERING AT THE MASSACHUSETTS INSTITUTE OF TECHNOLOGY

JUNE 2016

© 2016 Massachusetts Institute of Technology. All rights reserved

MASSACHUSETTS INSTITUTE OF TECHNOLOGY
JUN 02 2016
LIBRARIES
ARCHIVES

Signature of Author: Signature redacted
Department of Mechanical Engineering
May 20, 2016

Certified by: Signature redacted
Yang Shao-Horn
W.M. Keck Professor of Energy; SMART Research Professor of Mechanical Engineering,
Professor of Materials Science and Engineering
Thesis Supervisor

Accepted by: Signature redacted
Rohan Abeyaratne
Quentin Berg Professor of Mechanical Engineering
Chair, Departmental Committee on Graduate Student

Enhancing the oxidation of Li_2O_2 in Li-O_2 batteries: Mechanistic probing and process efficacy

By

Koffi Pierre Claver Yao

Submitted to the Department of Mechanical Engineering on May 20, 2016 in Partial Fulfillment of the Requirements for the Degree of Doctor of Philosophy in Mechanical Engineering

Abstract

The wide consensus regarding anthropogenic climate change, the positive correlation between economic growth and greenhouse gas emissions, and the humanitarian need for further global growth urges the decoupling of energy usage and emissions. To power portable electronics, enable electrification of transport, level the load on the current fossil-fuel powered grid, and provide storage for clean but intermittent wind and solar, low-cost and high energy density battery chemistries such as lithium-oxygen (Li-O_2) are being vigorously pursued beyond Li-Ion. The present thesis reports on efforts to devise and understand reaction promoters to enhance the kinetics of charging of Li-O_2 cells for the purpose of boosting round-trip efficiency, one of the most severe issues in the system.

Investigating trends in electrochemical current output during charge in electrodes containing transition metal nanoparticles and metal oxides, we revealed a strong correlation between the conversion enthalpy of the promoter with Li_2O_2 towards formation of a corresponding lithium-rich metal oxide. Experimental evidence of formation of Li_2CrO_4, and Li_2MoO_4 is provided. Ru nanoparticles showed the formation of a surface phase in contact with Li_2O_2 which is assigned to Li_2RuO_3. We postulate solid-state promoters activate the oxidation of Li_2O_2 by enabling the formation of a lithium-rich metal oxide intermediate which proceeds to delithiate with enhanced kinetics compared to the direct decomposition of Li_2O_2. A microkinetics analysis successfully explains the excellent Li_2O_2 oxidation activity of metal nanoparticles such as Cr, Mo, and Ru as well as the relative inactivity at 3.9 V_{Li} of Mn, Co and other derivative oxides. Using differential electrochemical mass spectrometry (DEMS), the same conversion

mechanism appears to result in sub-stoichiometric evolution of oxygen on charging as conversion enthalpy increase.

In the second and last part of this thesis, cobalt bis(terpyridine) metal complex ($Co(Terp)_2$) is demonstrated as redox mediator of the electron transfer to the insulating Li_2O_2. However, chemical probing using DEMS revealed a parasitic Co^{II} to Co^{I} reduction during discharge using the metal complex while the ideal 2.0 e^-/O_2 formation of Li_2O_2 is observed with benchmark mediator tetrathiafulvalene. On charge sub-stoichiometric O_2 regeneration is observed for both mediators; however, improved oxygen regeneration is seen using TTF.

Thesis Supervisor: Yang Shao-Horn

W.M. Keck Professor of Energy; SMART Research Professor of Mechanical Engineering, Professor of Materials Science and Engineering

Thesis committee Member: Martin Z. Bazant

Edwin G. Roos (1944) Professor of Chemical Engineering
Professor of Mathematics

Thesis committee Member: Alexie Kolpak

Rockwell International Career Development Professor of Mechanical Engineering

Acknowledgements

As is evident from the manuscript authorships of the works included in this thesis, I am indebted to a large number of individuals who were instrumental to every insights gained herein. Any one individual whose name is not explicitly listed below is, with certitude, not being excluded explicitly.

I will begin by stating my immeasurable gratitude to Professor Yang Shao-Horn for her mentorship in the past 5 years and 10 months. I am more so thankful because regardless of her many students and her clearly busy schedule, Yang found time to remind me that my work, its scientific rigor, and particularly steady progress thereof mattered. Would I have made it to the finish line without her continued reminders that perseverance was key? With the benefit of hindsight, I would never consider the alternative.

I am further grateful to my committee members, Professors Martin Bazant and Alexie Kolpak. With the benefit of hindsight again, I regret not having had nearly as many committee meetings as I could have. Their challenging of my assumptions was invaluable to the tuning of the science presented herein.

I found being a teaching assistant of design and manufacturing with Professor David Hardt and Dr. Dawn Wendell an excellent experience in teaching and I am immensely grateful for the opportunity.

Beyond my official academic coaches, I would like to thank Professor Yi-Chun Lu currently at the The Chinese University of Hong Kong for getting me started as a researcher in the electrochemical energy lab. Her curiosity and hard work were positively contagious.

At this point, I would like to extend special thanks all my co-authors listed in each chapter. Without their kind help, this thesis would certainly not have achieved this level of completeness. Without pretense of exhaustiveness, I will explicitly mention the following collaborators Dr. Jonathon Harding, Chibueze Amanchukwu, David Kwabi, Dr. Marcel Risch, Dr. Sayed Y. Sayed, Dr. Yueh-Lin Lee, Dr. Nir Pour, Dr. Jigang Zhou, Dr. Alexis Grimaud, Dr. Azzam Mansour, Professor Paula Hammond, Professor Zhichuan Xu, James T. Frith, Professor Nuria Garcia-Araez, and Professor John R. Owen.

I am especially grateful to Dr. Fanny Bardé at Toyota Motors Europe for her continued financial support over the past 5 years and more so for her invaluable scientific contributions and being what amounted to a co-advisor.

Outside the academic confines, I will be remiss not to acknowledge those, who although not authors on my publications, metaphorically held the pen in my hand. There clearly is no amount of thanks for Mr. Yao Yeboué and Mrs. Amoin Yao, my dad and mom, for helping me hold on through the incontrovertible rough patches. My siblings interspersed the needed amount of tried and true silliness (for me that is) that made the deadlines less daunting.

I will finish by extending a thank you to all my colleagues at the electrochemical energy laboratory both for the scientific conversations as well as the comradery on thirsty Fridays.

Content

List of Figures

List of Tables

Chapter 1. Introduction

1.1. Motivation

The drive to devise energy storage systems[1] such as galvanic batteries to accompany humanities energy production and consumption is justified by the need to curtail the generation of greenhouse gases in humanities growing energy activities. As will be discussed in the next few paragraphs, energy, industrial, farming, and agricultural activities in humanities technology-driven, fast paced development accumulates several greenhouse gases (GHG) including CO_2, CH_4, synthetic halocarbons, and N_2O at rates much higher than natural sources (Intergovernmental Panel on Climate Change, IPCC).[2] There is mounting consensus that these anthropogenic gases, chiefly CO_2 are responsible for the rise of the planet temperature, an unprecendented melting of the permafrost, rise in sea levels, ocean acidification as well as pertubation the climate and weather systems.[2]

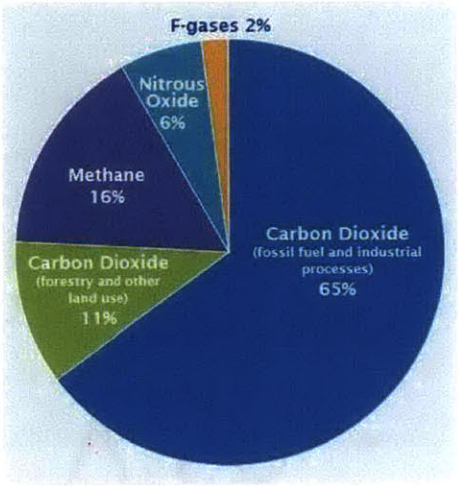

Figure 1-1. Greenhouse gas emissions by gases based on 2010 data. Figure reproduced from Fifth Assessment Report of the Intergovernmental Panel on Climate Change (IPCC).[2]

CO_2 is the main anthropogenic GHG resulting from combustion of fossil fuels and deforestation (Figure 1-1); its atmospheric concentration currently estimated at 402.59 ppm (up from 399.29 ppm in January 2015)[3] accounted for 1.33 to 2.03 $W \cdot m^{-2}$ (~79 %) out of a total of 2.29 $W \cdot m^{-2}$ increase in energy flux to the planet surface (referenced to 1750 levels, named radiative forcing or RF by IPCC).[2] CH_4, the next major anthropogenic GHG, is the product of agriculture, farming, and fossil fuel extraction and use; it current global tropospheric level is estimated at 1.84 ppm in 2014[4] and accounted for a RF of 0.97 $W \cdot m^{-2}$.

1.1.1. Anthropogenic climate change

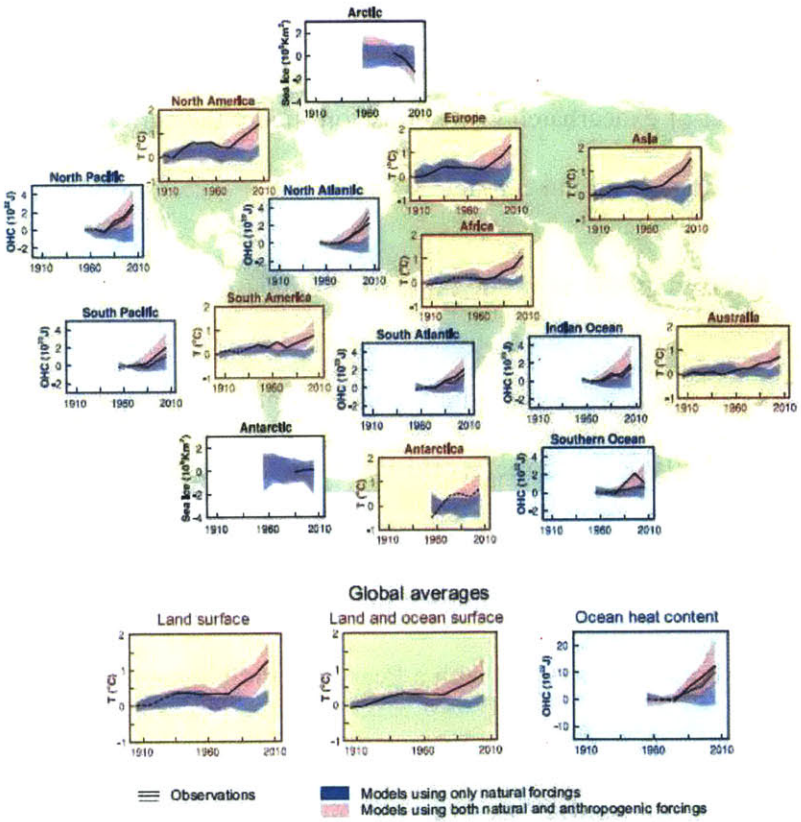

Figure 1-2. Comparison of observed and simulated climate change based on three large-scale indicators in the atmosphere, the cryosphere and the ocean. All time-series

are decadal averages, plotted at the center of the decade. Model results shown are Coupled Model Intercomparison Project Phase 5 (CMIP5) multi-model ensemble ranges, with shaded bands indicating the 5 to 95% confidence intervals. Figure SPM.6 reproduced with permission from 5th climate assessment report by IPCC.[2]

Global temperature rise designated as "global warming" is a well-established empirical observation. In the recent report by the IPCC[2], models in most regions of the globe agreed well with measured change in temperatures only after inclusion of anthropogenic sources; all regional models usually under-predicted temperatures changes with only natural sources (Figure 1-2). Global warming appears to result from human activities releasing chiefly CO_2 as well as CH_4 into the atmosphere. With economic development currently intimately tied to increased energy use as shown in the next section, the prospect of exacerbated GHG emissions under the current energy production and utilization paradigm is all but certain.

1.1.2. Energy, global economy, and greenhouse gases

Global energy demand increases with technology-backed development. Analysis of development data available from the World Bank Group (Figure 1-3) straightforwardly corroborate this assessment.[5] A positive correlation is evident in Figure 1-3a between energy usage and GDP per capita from 1960 to 2013. Globally, per capita, energy use is strongly positively correlated to GDP with a Pearson correlation coefficient between 0.44 and 0.92 and averaging 0.76 (Figure 1-3b). Coupling to that the fact that global GDP per capita is trending steadily upward as seen in Figure 1-3c with a doubling of planetary GDP per capita in the decade of 2000 to 2013, one easily concludes that global energy

demand grows with time and will likely grow in the future. In fact, 133 out of 191 countries examined show a Pearson correlation coefficient greater than +0.4 between passing years and per capita energy usage. The more concerning fact is the almost perfect synchrony between energy usage and CO_2 emission per capita observed in Figure 1-3c. The next section elaborates on the economic potential available within the global economy and the prospect of increased GHG emissions and global warming.

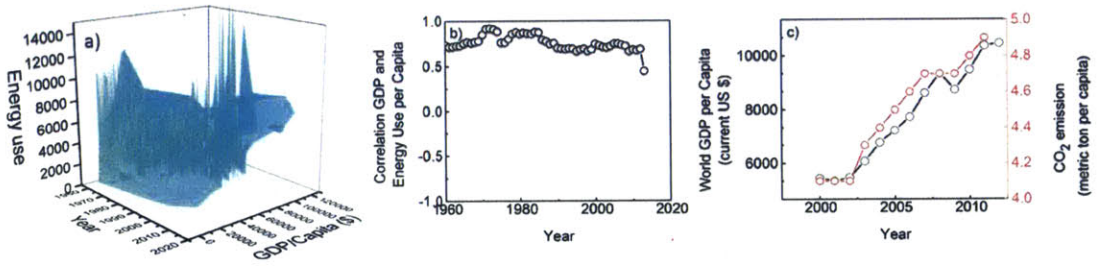

Figure 1-3. Relationship between per capita energy usage and GDP. (a) Energy use per capita plotted against GDP per capita over the years. (b) Correlation coefficient between energy use and GDP per capita from 1960 to 2013. (c) GDP per capita vs. time. Data pooled from for 248 countries in the world between 1960 and 2013. Raw data obtained from the World DataBank.[5]

1.1.3. Economic potential and the need for sustainable energy production and utilization

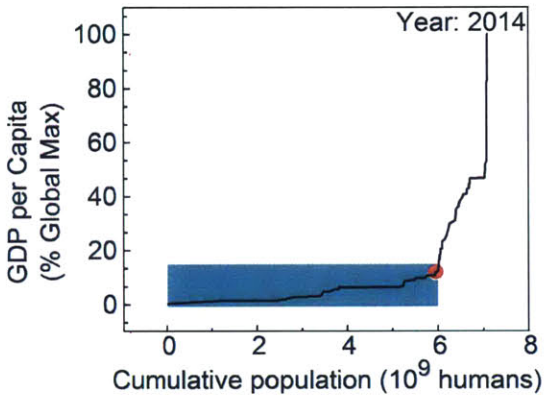

Figure 1-4. Plot of GDP per capita distribution versus cumulative population. Raw data obtained from the World DataBank.[5]

As of 2014, the majority of the world population (approximately 6 out of 7 billion) enjoys less than 12% of the gross domestic product of Luxemburg (blue highlight in Figure 1-4). To first order, 85% of the world population has a significant amount of development ahead. This economic growth potential coupled with the synchronized growth of GDP and energy demand seen in Figure 1-3c predict a vast increase in atmospheric CO_2 unless a major paradigm shift occurs to decouple energy activities from GHGs. In fact, under most socio-economic scenarios considered, the IPCC[2] predicts a worsening of all global warming and climate change parameters (increase in GHG concentrations, rise in sea levels and acidity…) manifested mainly as rising temperature with 95% confidence through to year 2100 (Figure 1-5).

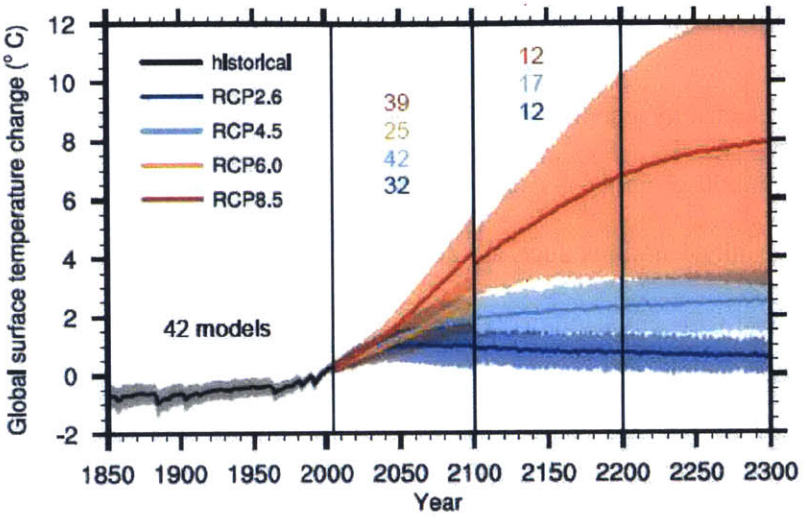

Figure 1-5. Global annual mean surface air temperature change relative to 1986–2005 from Coupled Model Intercomparison Project Phase 5 (CMIP5) concentration-driven experiments. Projections are shown for each representative concentration pathways (RCP) for the multi-model mean (solid lines) and 1.64 standard deviation band (5 to 95%). Figure reproduced with permission from the 5th IPCC report 2013.[2]

It is thereby clear that a major and rapid change in energy production and utilization paradigm need be made to mitigate the impact of global warming. The penetration of renewable, GHG-neutral energy sources such as solar, wind, geothermal, nuclear, and hydroelectric is paramount. However, due to the intermittent nature of solar and wind as well as the need to boost usage efficient of other sources, energy storage is needed in the next generation power grid. Additionally, portable storage is required for mobile consumption of the sustainably generated electric power. Below, the case is made for electrochemical storage drawing on the case of a major global energy consumer, the United States.

1.1.4. Justifying the pursuit of electricity storage

Globally, electricity generation constitutes a major lever in cutting upwards to one quarter of greenhouse emissions from fossil fuel energy generation (Figure 1-6a).[2, 6] In heavily industrialized nations such as the United States, electricity production generates over one third of CO_2 emissions (Figure 1-6b). Moreover, the transportation sector with the extensive use of internal combustion engines is responsible for 14% and 27% of the global and United States CO_2 emissions, respectively. On-site fossil fuel burning for industrial energy needs generates an additional 21% of the CO_2 emissions globally as well as in the United States. These statistics suggests that coupling of fossil-free electricity with electrified transportation could theoretically eliminate up to 58% of CO_2 emissions in the United States alone and 39% of GHGs globally. An additional effort to convert industrial energy needs to clean electricity could feasibly reduce an additional 21% of emissions.

In recent years, penetration of GHG-free solar and wind energy production have been growing exponentially but still linger at only 0.5% and 4.1% of the total generation respectively.[7] *One strong barrier to the use of wind and solar energy sources is undeniably the high cost of the storage required for leveling their intermittence.* Affordable, high-energy, and easily deployable electrical energy storage would speed up the adoption of renewable energy sources by enabling them to be as on-demand as the traditional coal, natural gas, hydroelectric, and nuclear sources.

Moreover, in 2014, the United States generated a total of 4093 TWh (an average of 468 GW) of electricity with 67% generated from fossil fuel.[8] As of summer of the

previous year, the total grid capacity was 996 GW, well in excess of the 786 GW peak demand anticipated by the North American Electric Reliability Corporation (NERC).[9] Certainly, the carbon footprint of the mainly fossil-fueled grid in the United States is adversely affected by the ~112% surplus capacity (26% with respect to peak demand) needed for load matching. Load leveling through electricity storage would inject both production and equipment efficiencies into the current grid of a nation such as the United States. Those efficiencies gain are expected to translate into reduced emissions and a positive effect on climate change.

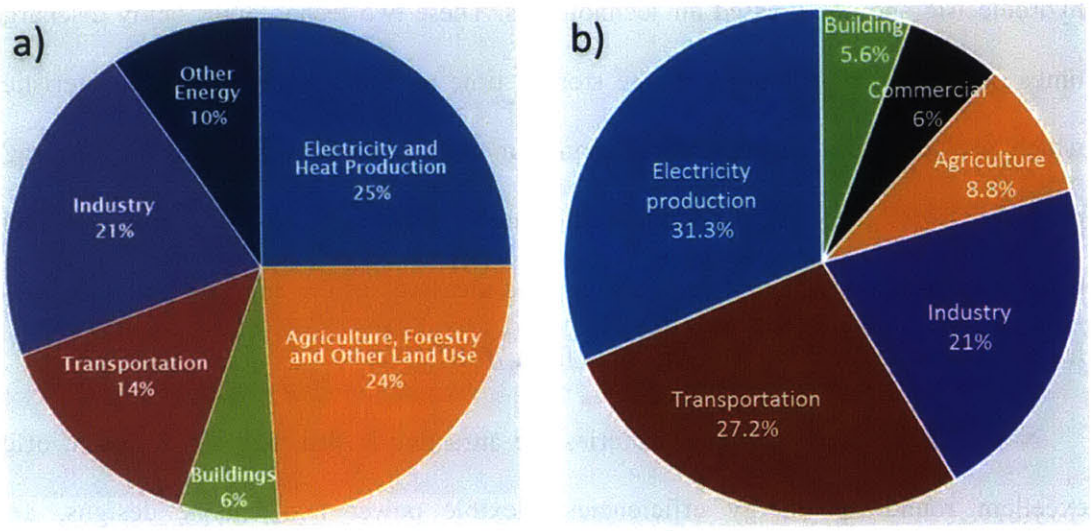

Figure 1-6. Source of greenhouse gas emission by sectors. (a) 2010 global GHG emissions by sectors. Note: Industry GHG production derives mainly from on-site fossil fuel burning for the purpose of energy generation. (b) US 2013 CO_2 emission by sectors from 2015 EPA data.[6]

On the utilization side of energy, transportation relies on internal combustion engines which burn fossil fuels with thermal efficiency usually below 20%.[10] With its significant

contribution to emissions (up to a third of total CO_2) and the number of vehicles predicted to increase with economic development, a clean mobile power solution as offered by batteries is also essential for this sector.

1.1.5. Making the case for electrochemical energy storage specifically

A large set of options are available for electrical energy storage. A non-exhaustive list of the currently mature storage technologies for buffering and leveling the grid are shown in Figure 1-7.[1] The current global grid power is stored mostly using pumped hydroelectric and compressed air technologies. These two technologies enjoy discharge times on the order of hours and idle storage time measured in months; characteristics which are ideal for general power management.[1, 11] These two mechanical storage methods also offer excellent reliability and ease of maintenance that is manifest in their worldwide adoption. Their storage efficiencies measured as the energy recuperated as a fraction of energy used in charging range from 70-89%.[11]

Nonetheless, electrochemical batteries are attractive in that they are compact, offer excellent round-trip energy efficiencies, flexible power and energy designs, and emission-free operation. Some electrochemical battery systems such as lead-acid, sodium-sulfur, lithium-ion (Li-Ion), and nickel metal hydride are already employed in grid storage (Figure 1-7).[1, 11] The advantages of batteries over the popular pumped hydroelectric and compressed air storage are: (i) their compactness allows for deployment in space-constrained application such as rooftop solar or residential on-site electric storage for decentralized power, (ii) they offer mobile power to substitute internal

combustions in electric vehicles, and (iii) their round-trip efficiencies which approaches 94% for Li-Ion means better energy utilization in all use cases.

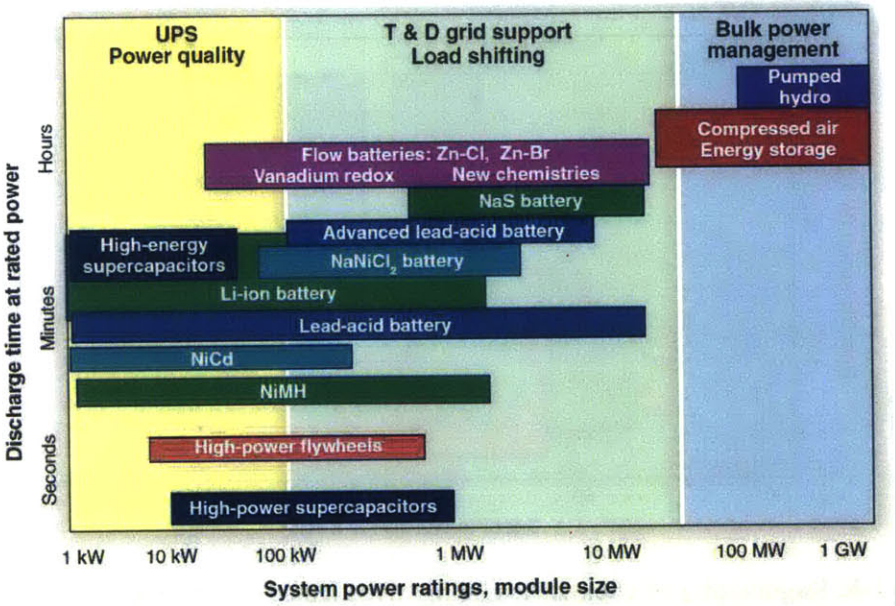

Figure 1-7. Comparison of discharge time and power rating for various electrical energy storage technologies. Figure reproduced with permission from American Association for the Advancement of Science (AAAS).[1]

1.2. Lithium based galvanic electrochemistries

1.2.1. Conventional galvanic chemistries and their potential

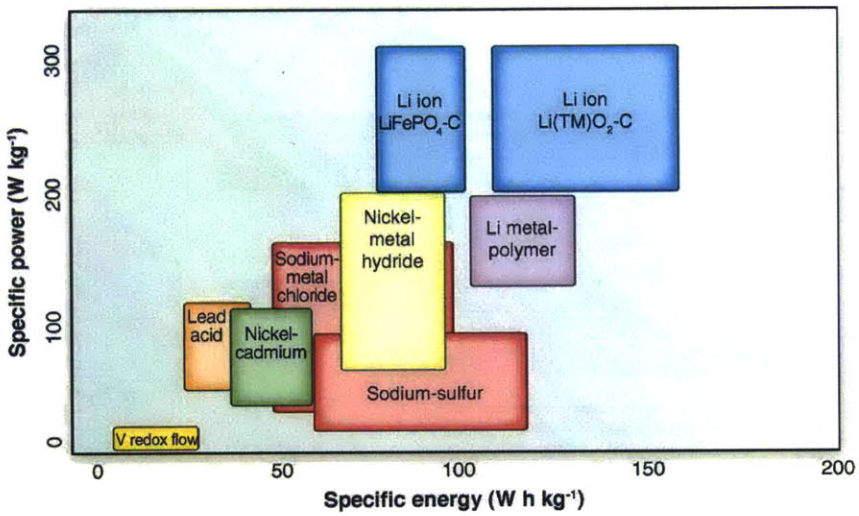

Figure 1-8. Ragone plot of chemistries being investigated and/or employed for storage application at grid or portable power level. Figure reproduced with permission from American Association for the Advancement of Science (AAAS).[1]

As noted above, several battery chemistries are candidate for grid storage in particular. However, of the systems under consideration, Li-Ion batteries skew to higher values of gravimetric energy density and power as seen in Figure 1-8. The lead in terms of storage potential of lithium-based chemistries is rooted in their use of lithium, the lightest alkali metal available with its large negative reduction potential (fifth most negative in the published electrochemical series) of -3.04 V versus the standard hydrogen electrode (SHE).[12] Consequently, the Li-Ion battery system has taken center-stage in high-energy and high-power applications; it is currently the chemistry of choice for powering portable electronics and the upcoming electric vehicles. The Li-Ion electrochemistry essentially

relies on the rocking exchange of Li^+ cations from an anode usually of a layered carbon host, LiC_6, and cathode of a layered transition metal (Figure 1-9). Whereby the anode is usually based on LiC_6 (anode host materials of the periodic table group IVA elements Si, Ge, Sn are in development[13]), cathodes such as $LiCoO_2$, spinel $LiMn_2O_4$, olivine $LiFePO_4$, $LiNi_{1/2}Co_{1/2}O_2$ (NMC), and $Li(Ni_{0.8}Co_{0.15}Al_{0.05})O_2$ (NCA) are in commercial use.

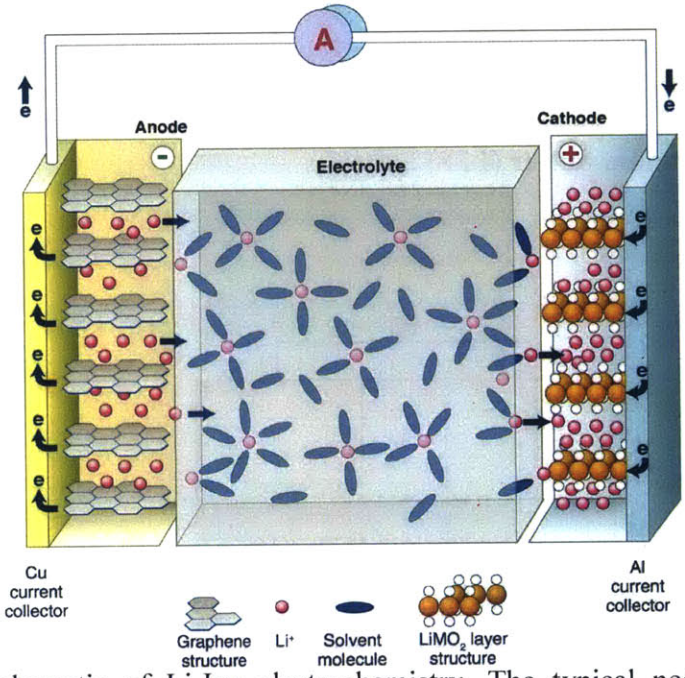

Figure 1-9. Schematic of Li-Ion electrochemistry. The typical negative electrode (anode) is made of graphitic carbon capable of hosting Li^+ cations in its layers. The positive electrode (cathode) consists of layered lithium metal oxide. Figure reproduced with permission from American Association for the Advancement of Science (AAAS).[1]

However popular and energy dense, Li-Ion batteries are costly at \$600 kWh^{-1} requiring approximately 0.7 trillion dollars investment to store say one tenth of the 2014

US average daily consumption of 11.3 GWh.[8, 14] *Affordable and high energy battery storage are needed to both facilitate penetration of intermittent renewables, reduce the required grid surplus and offset the associated excess emission, and enable the electrification of transportation.* To achieve this goal several new electrochemistries that go beyond the fundamental limitations of Li-Ion batteries have been proposed including multivalent-cations batteries, lithium-sulfur (Li-S), lithium-air (also named lithium-oxygen, Li-O_2). This thesis is concerned with the latter Li-O_2 electrochemistry. A brief discussion of the Li-S system is provided for reference.

1.2.2. Lithium-Sulfur (Li-S) batteries

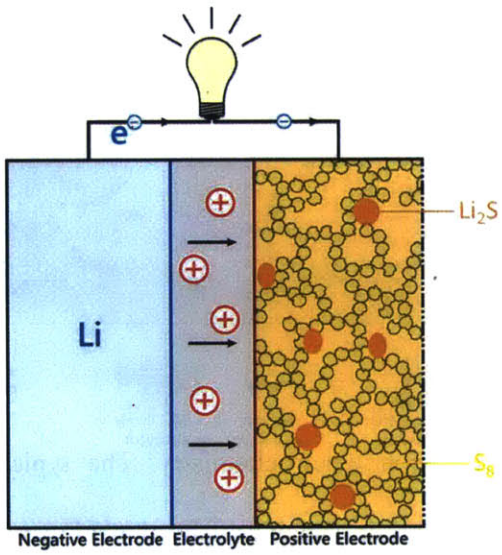

Figure 1-10. Schematic of Li-S cell shown during discharge. Dark network in the positive electrode represent the typical porous carbon structure. The carbon structure is filled with sulfur (S_8) shown as transparent yellow. Dark orange ellipses represent Li_2S which grows as the final product of the lithium conversion with sulfur in the pore structure during discharge.

Lithium sulfur batteries rely on the conversion of lithium with elemental sulfur towards formation of Li_2S. The fundamental reaction which lends galvanic energy storage and release property to the Li-S cell is $2Li^+ + 2e^- + S \rightarrow Li_2S$. This reaction is spontaneous with negative free energy and a cell voltage of 2.15 V vs. lithium is observed.[15] The theoretical gravimetric capacity of sulfur is evaluated at 1675 $mAh \cdot g^{-1}_{Sulfur}$ and therefore energy densities of ~2500 $Wh \cdot g^{-1}_{Li2S}$ (gravimetric) and ~2800 $Wh \cdot g^{-1}_{Li2S}$ (volumetric) is reported.[14, 15] The challenges facing Li-S batteries are, in quasi-order of acuity: (i) polysulfides shuttling from anode to cathode resulting in progressive energy loss, (ii) insulating nature of the final Li_2S product causing significant discharge to charge hysteresis, and (iii) volumetric expansion of cathodes post-discharge due to the low density of Li_2S compared to sulfur which constrains practical sulfur loading and impact volumetric energy density.[15] These issues still prevent the Li-S from entering mainstream use.

1.2.3. Lithium-Oxygen ($Li-O_2$) batteries

$Li-O_2$ or Li-air batteries have the potential to revolutionize energy storage with an estimated practical gravimetric energy density three times greater than current Li-Ion batteries.[16] A $Li-O_2$ cell stores the electrochemical energy of the reaction between lithium and oxygen towards usually the formation of Li_2O_2 ($2Li^+ + O_2 + 2e^- \leftrightarrow Li_2O_2$) as illustrated schematically in Figure 1-11. This conversion reaction is thermodynamically spontaneous with a negative free energy and electrochemical potential of 2.96 V versus lithium.[17] The smaller molecular weight of gaseous oxygen compared to transition metal oxides culminate in greater theoretical gravimetric capacity (1168 $mAh \cdot g^{-1}_{Li2O2}$)[14] and energy densities (3500 $Wh \cdot kg^{-1}_{Li2O2}$) for $Li-O_2$ compared to contemporary Li-Ion (544

$Wh \cdot kg^{-1}_{LiFePO4}$, 548 $Wh \cdot kg^{-1}_{LiMn2O4}$, and 1013 $Wh \cdot kg^{-1}_{LiCoO2}$ as reported by Lu et al.[18]). As a consequence the Li-O_2 battery chemistry currently enjoys great scientific attention as a next-generation rechargeable battery.

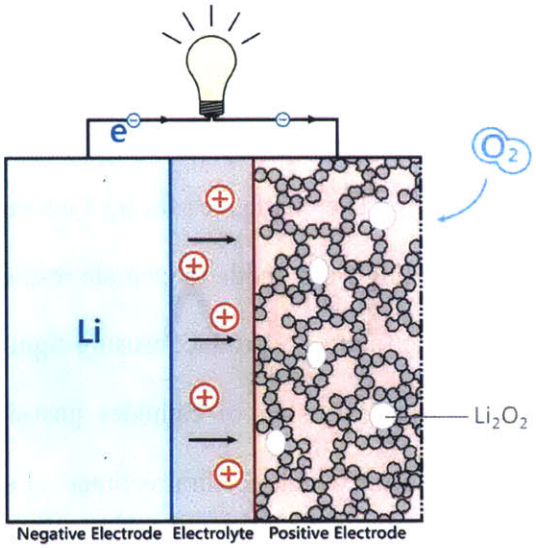

Figure 1-11. Schematic of Li-O_2 cell shown during discharge. Dark network in the positive electrode represent the typical porous carbon structure. White ellipses represent Li_2O_2 which grows as the final product of conversion of lithium with oxygen in the pore structure during discharge.

As it is the entire scope of the present thesis, we will further elaborate on the specific promises of Li-O_2 batteries relative to other chemistries, chiefly versus Li-Ion. Since Li-S is still under research and development, it suffice to note that the 3500 $Wh \cdot kg^{-1}_{Li2O2}$ is sufficiently larger than the 2500 $Wh \cdot g^{-1}_{Li2S}$ to justify parallel pursuit of Li-O_2 development. Figure 1-12 shows the cell-level gravimetric and volumetric energy densities of Li-Ion, Li-O_2, referred to the USCAR electric vehicle (EV) target; "cell" consist of a graphite intercalation anode (LiC_6) paired with the designated cathode.

Theoretically, at the cell level, the Li-O_2 system holds approximately twice the gravimetric and twice the volumetric energy sought for EVs. It is interesting to note that, on a theoretical basis, most common Li-Ion battery systems have the potential to fulfill the USCAR EV target; however, at the system level Li-Ion are still far from the EV target; this fact demands the consideration of more promising battery systems such as Li-O_2.

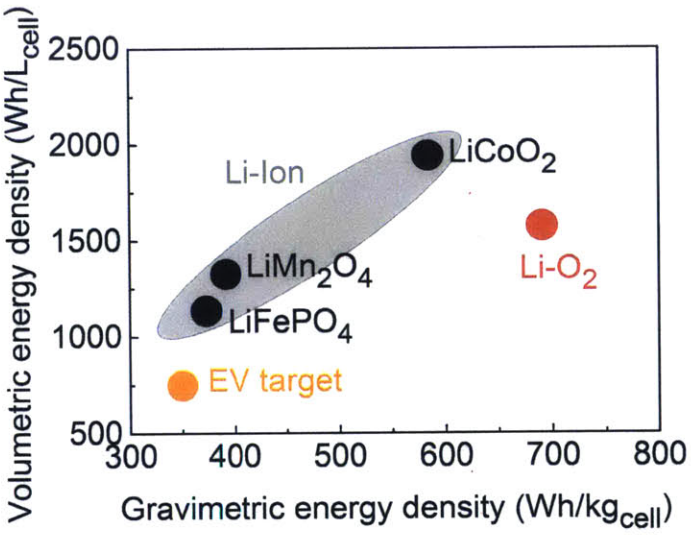

Figure 1-12. The potential of Li-O_2 batteries. Theoretical cell-level (LiC_6 anode excluding excess lithium + cathode) gravimetric energy vs. power density of Li-O_2 visualized against current Li-Ion and USCAR targets[19]. This plot is generated through synthesis of data available from Lu *et al.*[18]

Computational analysis by Gallagher *et al.*[16] predicts gravimetric energy densities of ~300 Wh·kg^{-1} for system-level applications in electric vehicles, a twofold increase in energy density relative to Li-Ion cells. As illustrated in Figure 1-13, the Li-O_2 system has better inbuilt capability to approach the USCAR EV goal; more so than current Li-Ion.

Finally, by virtue of low to zero cost of oxygen, the Li-O_2 system could offer batteries at the estimated price point of \$150 kWh^{-1}, a fourfold lower price than current Li-Ion.[14]

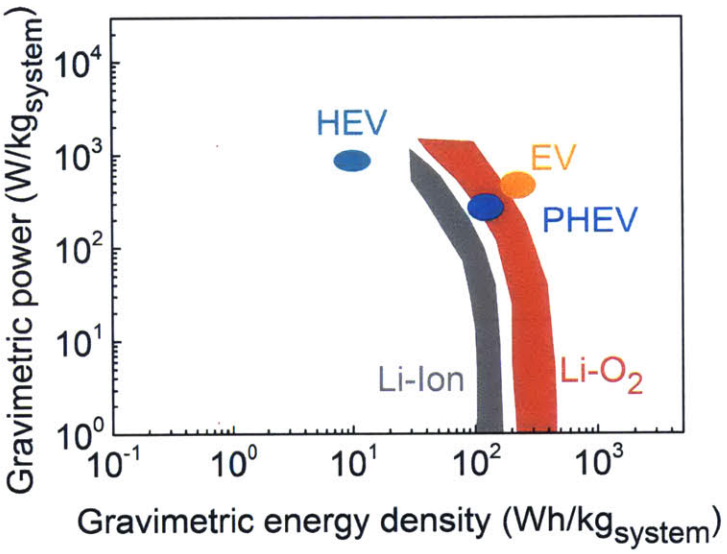

Figure 1-13. The potential of Li-O_2 batteries. Estimated system-level gravimetric energy vs. power density of Li-O_2 visualized against current Li-Ion and USCAR targets[19]. This plot is generated through synthesis of data available from Lee et al.,[20] Gallagher et al.,[16] and USCAR[19]. The power vs. energy profile is approximated from cathode trend data available in Figure 2 of Lu *et al.*[18]

1.3. The challenges to a practical Li-O_2 cell

Notwithstanding all its theoretical promise, many challenges must be resolved before practical Li-O_2 devices can be produced. In particular, Li-O_2 batteries suffer from high charging potentials, low round-trip efficiency, and limited cycle life, which have been attributed to the reactivity of Li-O_2 discharge products[21-24] and poor oxidation kinetics of Li_2O_2 formed upon discharge.[18, 25]

1.3.1. Reactivity in the Li-O_2 battery

Arguably one of the most challenging issue in Li-O_2 batteries is the degradation of most organic solvents used in the electrolyte. Early work on the Li-O_2 system employed the carbonate solvents familiar in Li-Ion batteries. However, it became evident that those carbonate electrolyte solvents, although stable for thousands of cycle in state-of-the-art Li-Ion batteries, degrade to Li_2CO_3, and alkyl carbonates such as $CH_3H_6(OCO_2Li)_2$, HCO_2Li, CH_3CO_2Li on the first discharge of Li-O_2 cells.[26]. This unanticipated instability of carbonate solvents during discharge of Li-O_2 cells is due to the formation of superoxide O_2^-; the strong nucleophile superoxide[27, 28] attacks positively charged centers of the solvents resulting in the poor stability of carbonate solvent[29] otherwise stable in the superoxide-free Li-ion batteries. In fact, the superoxide formed during the first reaction step is highly reactive towards most organic carbonates such as propylene carbonate (PC), ethylene carbonate (EC), Dimethyl carbonate (DMC), and ethyl-methyl carbonate (EMC).[23, 26, 30, 31] Similar nucleophilic attack by occurs at a reduced rate using ether solvents such as 1,2 dimethoxethane, tetraglyme (TEGDME), 1,3-dioxylane, 2-methyltetrahydrofuran.[22, 32] Although ethers such as glymes and dimethoxyethane are relatively stable against decomposition in Li-O_2 cells,[33, 34] steady buildup of parasitic solvent degradation (not Li_2O_2) products occurs during cycling of Li-O_2 cells.[22, 32] Additionally, the porous carbon structure prevalent in Li-O_2 is subject to corrosion forming Li_2CO_3.[22-24]

1.3.2. Poor conductivity of the discharge product Li_2O_2

The discharge product of Li-O_2 batteries as mentioned above is Li_2O_2. Li_2O_2 in its known chemical form (hexagonal symmetry, space group $P6_3/mmc$)[35, 36] is electrically

insulating with a band gap estimated in the range of 2 to 5 eV.[37-39] Experimental measurement of chemically synthesized Li_2O_2 estimates its electronic conductivity at 10^{-12}-10^{-11} $S \cdot cm^{-1}$ at the elevated temperature of 100 °C.[40] Ion transport is estimated at 10^{-10}-10^{-9} $S \cdot cm^{-1}$ at the same temperature. These charge transport numbers are not conducive to fast electrochemical charge transport.

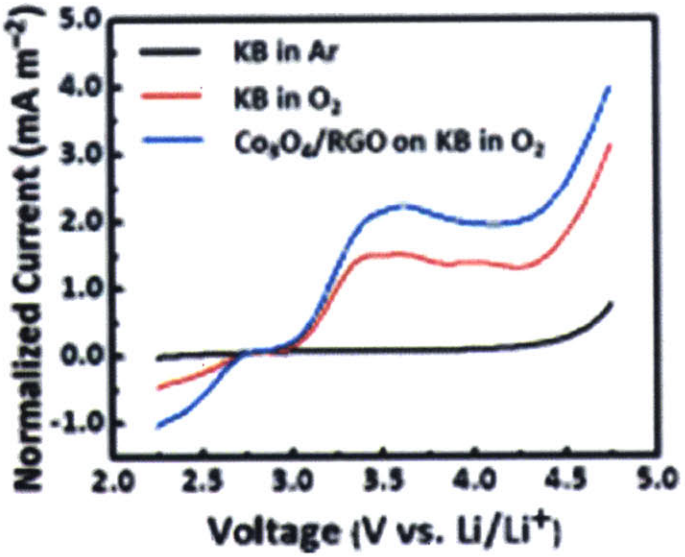

Figure 1-14. Linear sweep voltammetry performed for oxidation of Li_2O_2 oxidation on charge in Li-O_2 batteries following discharge in O_2 atmosphere. Reproduced with permission from Nazar et al.[41]

1.3.3. Poor charging kinetics as a consequence of reactivity and insulating Li_2O_2

Current laboratory Li-O_2 cells using relatively stable ether electrolytes require over 1 V overpotential for charging of carbon based electrodes in the absence of reaction promoters at rates above 70 $mA \cdot g^{-1}_{Carbon}$[24, 42] although Gallant et al.[42] have resolved an influence of the morphology of the Li_2O_2 formed on discharge. This high required

overpotential is in disagreement with the calculated 0.2-0.6 V minimum overpotential of oxidative decomposition of Li_2O_2.[43, 44] Experimentally, using linear sweep voltammetry, onset of oxidation of Li_2O_2 deposited on discharge is observed at ~3.0 V vs. lithium as seen in Figure 1-14.[41] The poor charging kinetics of Li-O_2 batteries is likely the result of parasitic discharge products and the low charge conduction through Li_2O_2 discussed above.

1.4. Thesis scope

This thesis focuses on the utilization of electrode or electrolyte additives as reaction promoters for the oxidation of the discharge product (Li_2O_2) with the goal of identifying avenue to improve the charging efficiency of Li-O_2 batteries. As noted above, the charging kinetics of Li-O_2 is one of the major hurdles facing the technology currently.

We begin in Chapter 2 by introducing chromium-based oxides as high activity metal (oxides) towards the Li_2O_2 oxidation reaction. The presence of unwanted discharge products from degradation of the electrolyte solvent impedes fundamental investigation of the Li_2O_2 decomposition during recharge. Therefore, electrodes fabricated in the discharged state by preloading with commercial chemically synthesized Li_2O_2 at fabrication are used to bypass discharge. Primarily, it is found that the large number of oxidation states available to the chromium metal center (Cr^{3+} and Cr^{6+} in particular) in powders of $LaCrO_3$, Cr_2O_3 and bulk Cr nanoparticles results in enhanced metal/Li_2O_2 chemical interactions. These chemical interactions appear to result in enhanced electro-oxidation of Li_2O_2 as gauged through measured faradaic current. It is explicitly shown using ex situ X-ray absorption spectroscopy that the enhanced electro-oxidation of Li_2O_2 is accompanied by intermediate change in the oxidation state of surface chromium. As a

result of the clear chemical change in the catalyst nanoparticle, we refer to the solid-state metal nanoparticles added for the purpose of enhancing the Li_2O_2 reaction kinetics as 'promoters' since permanent modification of the catalyst is possible.

Upon discovery of a chemical participation of the 'catalyst' (referred to as promoters in this thesis), it became necessary to establish the underlying mechanism or pathway through which the solid promoter interacts with the solid Li_2O_2 to facilitate electron extraction during oxidation of the latter. Consequently, Chapter 3 deals with understanding the pathway of activation of the Li_2O_2 oxidation reaction using metal (oxides) nanoparticles. A survey of a large number of metal and metal oxide nanoparticles allowed establishing a trend of relative enhancement effect across compounds. It is found that molybdenum with similarly wide change in oxidation state as chromium is correspondingly highly active towards Li_2O_2 oxidation. Once again, using X-ray adsorption spectroscopy, we establish the formation of Li_2CrO_4 and Li_2MoO_4 during oxidation of Li_2O_2 in presence of Cr and Mo respectively. A strong correlation between the enthalpy of formation of a lithiated metal oxide from thermodynamically favorable conversion of Li_2O_2 and high activity promoters ($Li_2O_2 + M_aO_b \pm O_2 \rightarrow Li_xM_yO_z$) is established. A model assuming a chemical conversion followed by electrochemical delithiation is found to fit well with the data set generated.

Under this mechanism of "chemical conversion followed by electrochemical delithiation", we proceed to investigate the oxygen consumption and regeneration in Li-O_2 batteries in presence of high activity promoters such as Mo, Cr, and Ru in Chapter 4. Attention is paid to the number of electrons per oxygen (O_2) consumed on discharge or evolved on charge. It is elucidated that in the same way as no influence of the metal

promoter is seen on the discharge kinetics, the oxygen consumption adhere to the expected 2 e^-/O_2 reaction ($2Li^+ + O_2 + 2e^- \leftrightarrow Li_2O_2$) which is attributable to the porous carbon structure supporting the promoter. On charge, however, Mo with a significantly large enthalpy of conversion with Li_2O_2 displays much less O_2 evolution per electrons compared to electrodes containing Cr, Ru, or purely carbon. The conversion reaction encountered with metal nanoparticle promoters appear to reduce the stoichiometry of oxygen evolution on charging of Li-O_2 cells.

In Chapter 5, we explore a second means of enhancing the Li-O_2 charging reaction based on the use of electrolyte soluble redox agents with facile electro-oxidation and formal potential slightly above that of Li_2O_2. These redox agents called 'redox mediators' or 'redox shuttles' operate by oxidizing first above the 2.95 V (versus Li) reversible potential of Li_2O_2; by virtue of its potential being above that of Li_2O_2, the oxidized form of the redox mediator is expected to chemically oxidize Li_2O_2, essentially creating and indirect and kinetically faster electron transfer path for Li_2O_2 oxidation. In Chapter 5, the metal complex cobalt bis(terpyridine) generally soluble in organic solvents was investigated and benchmarked against tetrathiafulvalene which is a mediator well known in the Li-O_2 literature. It is found that the two mediators reduce the potential required for oxidation of Li_2O_2 to values as low as 3.5 V versus lithium. However, using differential electrochemical mass spectrometry (DEMS), it is further found that although oxygen evolution occurs at these much reduced charging overpotentials (< 600 mV), the amount of oxygen is significantly sub-stoichiometric, particularly with the cobalt metal complex.

The current thesis highlights the need for careful probing and understanding of the chemical response of the Li-O_2 cell to external faradaic loading in order to design truly secondary Li-O_2 batteries.

Chapter 2. High activity of chromium-based metal oxides towards Li_2O_2 oxidation

Adapted with permission from K. P. C. Yao, Y.-C. Lu, C. V Amanchukwu, D. G. Kwabi, M. Risch, J. Zhou, A. Grimaud, P. T. Hammond, F. Bardé, Y. Shao-Horn (2014). The influence of transition metal oxides on the kinetics of Li_2O_2 oxidation in Li-O_2 batteries: high activity of chromium oxides. *Physical Chemistry Chemical Physics : PCCP*, *16*(6), 2297–304. doi:10.1039/c3cp53330a

2.1. Introduction

As stated in the introduction to this thesis, non-aqueous lithium-oxygen ($Li\text{-}O_2$) batteries, which form lithium peroxide (Li_2O_2) on discharge, have the potential to deliver gravimetric energy three to five times greater than that of current state of the art Li-ion batteries.[14, 17, 45] Unfortunately, charging of $Li\text{-}O_2$ batteries requires large overpotentials, even with ether-based electrolytes, which are relatively stable against reaction intermediates upon oxygen reduction such as superoxide,[29, 32, 34, 46, 47] notwithstanding the minor presence of electrolyte decomposition products during the first cycle.[22, 32, 48] The following sets of chapters are concerned with the incorporation and understanding of the influence of solid-state nanoparticles and soluble redox molecules as catalytic agents for the charging of $Li\text{-}O_2$ batteries. For reasons that will be clarified in Chapter 3, we refer to the solid-state catalytic nanoparticles as reaction promoters.

The kinetics of electro-oxidation of Li_2O_2 is shown to be dependent on the average thickness of the deposit formed within the electrode.[49] Thin Li_2O_2 deposits (averaging less than ~1 nm on the extended surface of the electro-active material)[18, 50-53] or at the early stage of charging[42] can proceed with overpotentials smaller than ~500 mV. In contrast, large overpotentials greater than ~1000 mV are noted typically on the electro-oxidation of Li_2O_2 deposits with average thicknesses greater than ~5 nm and at high rates (~1 $\mu A\ cm^{-2}_{true}$).[18, 42, 51, 52, 54-56] As demonstrated by Yi-Chun et al.[49], a first stage during oxidation of Li_2O_2 (labeled "I" in Figure 2-1) which is associated with a delithiation/disproportionation of Li_2O_2 is insensitive to applied rate, and thereby likely not be influenced by the presence of a reaction promoter. In contrast, a second and third stages (labeled "II" and "III" in Figure 2-1) are strongly rate dependent and thereby

expected to be influenced by a reaction promoter such as added transition metals. To realize the gravimetric energy advantage of Li-O_2 batteries to Li-ion batteries, it is necessary to enable facile formation and oxidation kinetics of Li_2O_2 deposits (with thicknesses greater than a few nanometers) within the electrode pore volume during discharge and charge.

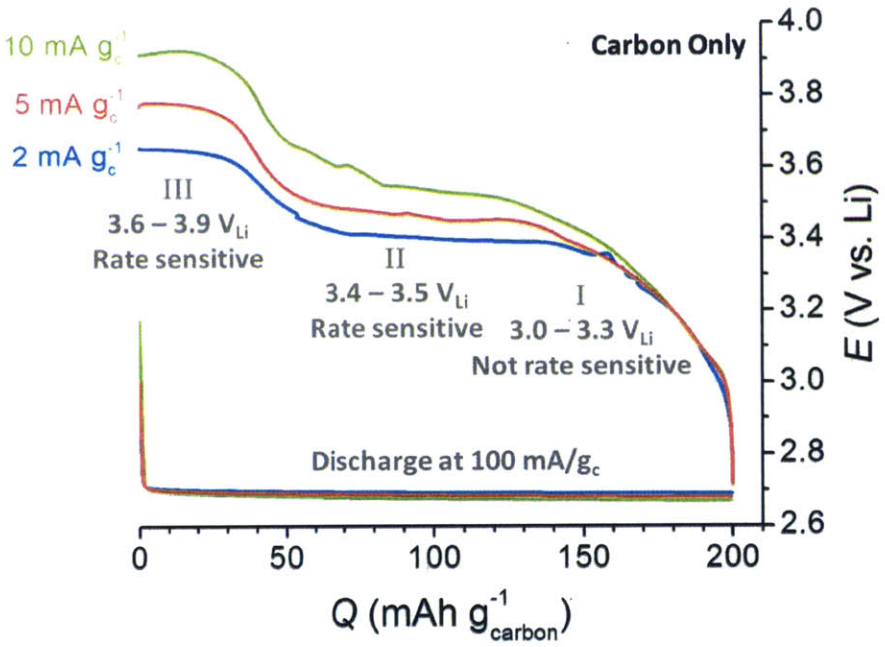

Figure 2-1. Rate dependence of charging voltage of Li-O_2 batteries using Vulcan carbon based electrodes. Each color represents a particular discharge and charge experiment. All cells discharged at 200 mA·g$^{-1}_{Carbon}$ to 200 mAh·g$^{-1}_{Carbon}$. Charging rates are noted besides each charging curve. Figure adapted from work performed by Yi-Chun et al.[49]

Although the physical origin of the large overpotentials associated with Li_2O_2 oxidation is not well understood, the following factors have been shown to influence the

charging voltage from previous studies. First, electrolyte solvents such as dimethylformamide[57] and dimethylsulfoxide[58] provide lower charging voltages (~3.6 V_{Li} at 0.1 $\mu A\ cm^{-2}_{carbon}$ or 70 $mA\ g^{-1}_{carbon}$) compared to ether-based solvents using carbon electrodes. Unfortunately these solvents are not stable against lithium metal.[58, 59] Second, redox mediators have recently enabled charging of carbon cathodes in Li-O_2 cells at ~3.6 V_{Li}.[60, 61] Third, Harding et al.[62] have shown that noble metals such as Pt and Ru nanoparticles supported on carbon can promote the oxidation kinetics of Li_2O_2 particles (~345 nm) and achieve oxidation currents hundredfold higher than that of carbon-only electrodes using 0.1 M $LiClO_4$ 1,2 dimethoxyethane (DME) electrolyte, allowing Li_2O_2 oxidation at ~3.5 V_{Li}. Unfortunately, the greater kinetics for Li_2O_2 electrochemical oxidation with these noble metal catalysts are accompanied with enhanced electrolyte oxidation. Fourth, non-noble metal oxides have been used to lower the charging voltages of Li-O_2 cells[54, 55, 63] or Li_2O_2-filled[64, 65] electrodes, as summarized in Table 2-1, where only studies with ether-based electrolytes are included. For example, $Na_{0.44}MnO_2$ (ref. [55], 70 $mA\ g^{-1}_{carbon}$, carbon/oxide weight ratio of 1:0.4), and $Pb_2[Ru_{1.7}Pb_{0.3}]O_{6.5}$ pyrochlores[54, 66] (70 $mA\ g^{-1}_{carbon}$, carbon/oxide weight ratio of 1:1) have shown ~3.9 V_{Li} for Li_2O_2 oxidation while layered-perovskite-based[65] $La_{1.7}Ca_{0.3}Ni_{0.75}Cu_{0.25}O_4$ provides charging at ~3.6 V_{Li}, albeit at a lower rate of 20 $mA\ g^{-1}_{carbon}$ and carbon/oxide weight ratio of 1:0.3. As carbon/oxide ratios, oxide/Li_2O_2 ratios, and the surface area of oxides and Li_2O_2 in these previous studies[54, 55, 66] vary greatly, ambiguities exist in deducing the oxide activities for Li_2O_2 oxidation kinetics by comparing the reported charging voltages of different oxides across these studies.

In this second chapter, we begin our investigation of the influence of solid-state promoters on the Li_2O_2 oxidation kinetics using chromium based nanoparticles. Chromium is a transition metal in the group VI of the periodic table and therefore has available oxidations ranging from +1 to +6. The oxidation of Li_2O_2 during charging of Li-O_2 cells is an oxygen evolving reaction (OER). Prior work of aqueous fuel cell systems[67-69] and even ammonia synthesis[70] shows a deterministic effect of the electronic interactions of the catalyst surface with reaction intermediates. These electronic factors have led to the realization of the Sabatier principle using electronic descriptors such as metal-adsorbate bond strength,[67, 71], d-band center,[72, 73] and e_g-filling.[69] The wide range of chromium oxidation states is anticipated to lead to electronic interactions with the oxidant Li_2O_2 which could enhance its oxidation kinetics. We observed that chromium based solid-state promoters such as Cr nanoparticles (Cr NP), $LaCrO_3$ and Cr_2O_3 indeed display much higher Li_2O_2 oxidation currents compared to Vulcan carbon (VC).

Table 2-1. Literature values for Li_2O_2 oxidation activities under various cell conditions

Catalyst	Electrolyte used	Rate (mA g^{-1}_{Carbon})	Rate (mA g^{-1}_{Li2O2})*	Rate (μA cm^{-2}_{Carbon})	Rate (μA cm^{-2}_{Cat})	Rate (μA $cm^{-2}_{Carbon+Cat}$)	Charging voltage (V)	Cathode structure
Pt/VC	0.1 M $LiClO_4$ DME	70	70	0.070	0.114	0.043	~3.6	Li_2O_2-prefilled (VC:Catalyst:Li_2O_2 = 1:0.66:1)[62]
Ru/VC				0.070	0.088	0.039	~3.6	
Au/VC				0.070	0.482	0.061	~4.2	
Vulcan Carbon (VC)				0.070	0.070	0.035	~4.1	
KB/Acid leached $Na_{0.44}MnO_2$	1 M $LiPF_6$ TEGDME	70	7.4	0.009	0.255	0.008	~3.8	Li-O_2 cell (KB:Catalyst = 1:0.4)[55]
KB/Pristine $Na_{0.44}MnO_2$			14	0.009	0.384	0.008	~4.0	
Ketjen black (KB)			41	0.009	0.009	0.008	~4.1	
KB/Lead ruthenate	1 M $LiPF_6$ TEGDME	70	14	0.009	0.106	0.008	~4.0	Li-O_2 cell (KB:Catalyst = 1:1)[54]
KB/Bismuth ruthenate			14	0.009	0.068	0.008	~4.0	
Ketjen Carbon (KB)			27	0.009	0.009	0.004	~4.2	
KB/ $La_{1.7}Ca_{0.3}Ni_{0.75}Cu_{0.25}O_4$	1 M $LiPF_6$ TEGDME	20	67	0.008	1.811	0.008	~3.6	Li_2O_2-prefilled (KB:Catalyst:Li_2O_2 = 1:0.3:0.3)[65]
Super P (No catalyst)	0.1M $LiClO_4$, DMF	70	54	0.113	0.113	0.113	~3.6	$LiFePO_4$-O_2 cell[57]
Super P (No catalyst)	0.1M $LiClO_4$, DMSO	70	164	0.113	0.113	0.113	~4.1	Li-O_2 cell[58]
Super P/Gold nano composite electrode	0.1M $LiClO_4$, DMSO	70	164	0.113	1.120	0.103	~3.8	Li-O_2 cell (Super P:PTFE:Au = 8:1:1)[58]
Nanoporous Gold	0.1M $LiClO_4$, DMSO	500 mA/g_{Au}	1947	N/A	1.000	1.000	~3.5	Li-O_2 cell[58]

2.2. Experimental Procedure

2.2.1. Synthesis of $LaCrO_3$

$LaCrO_3$ were synthesized by nitrate combustion methods.[68, 69, 74] Lanthanum (III) nitrate hexahydrate ($La(NO_3)_3 \cdot 6H_2O$, >99.9%, Alfa Aesar) and chromium nitrate nonahydrate ($Cr(NO_3)_3 \cdot 9H_2O$, 99.99%, Alfa Aesar) were mixed in de-ionized water (Milli-Q water, 18 MΩ·cm) at metal molar ratio of 1:1 and total concentration of 0.2 M. The solution was subsequently titrated using an aqueous 1.2 M solution of tetramethylammonium hydroxide (Alfa Aesar) resulting in precipitation. The precipitate was then filtered and collected to dry. Finally, the precipitate powder was heat treated in a tube oven at ~1000 °C under dry air for approximately 10 hours.

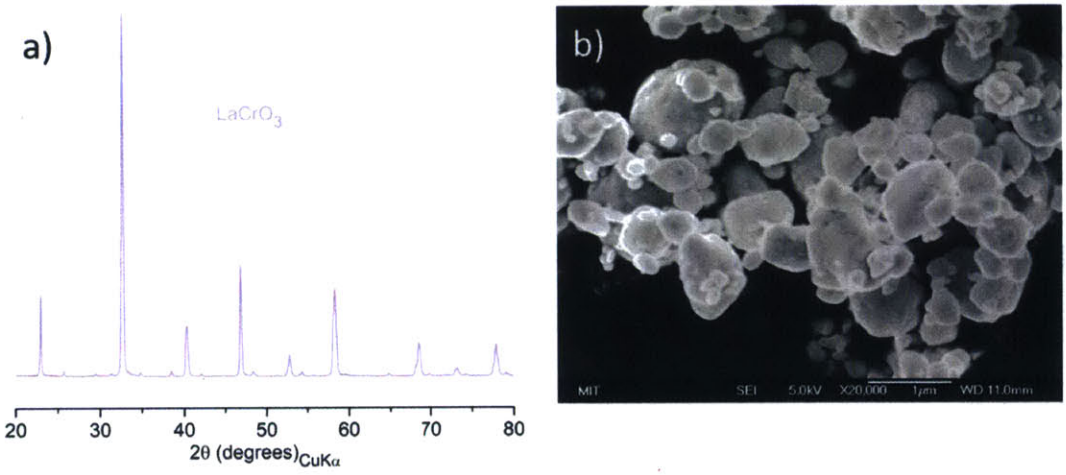

Figure 2-2. Characterization of synthesized $LaCrO_3$. (a) XRD spectrum of $LaCrO_3$ synthesized by nitrate combustion. (b) SEM of ball-milled $LaCrO_3$ powder.

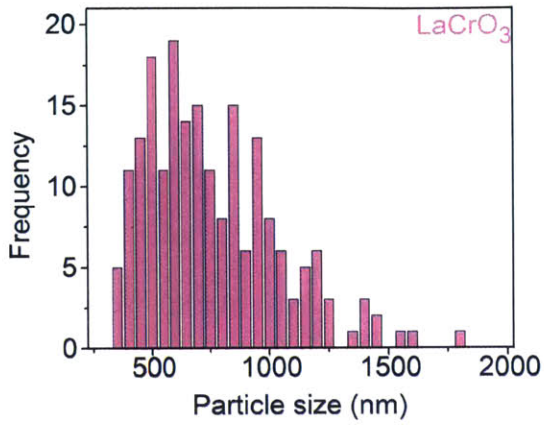

Figure 2-3. Particle size distribution of $LaCrO_3$ post ball-milling. Size quantification of 200 particles was done with using ImageJ.[75]

The obtained $LaCrO_3$ was sufficiently phase pure with less than 1% impurities observed by X-ray diffraction (Figure 2-2a). $LaCrO_3$ was then ball-milled using a planetary ball mill (Pulverisette 6, Fritsch Inc., zirconia crucible sealed under argon) at 500 rpm. Ball milling resulted in a broad distribution of $LaCrO_3$ particles as seen in the SEM micrograph (Figure 2-2b) and by size quantification (Figure 2-3). The average particle size of $LaCrO_3$ after balling was estimated at ~951 nm. This particle size is used to estimate the powder surface area at 0.95 $m^2 \cdot g^{-1}_{LaCrO3}$.

2.2.2. Electrode fabrication

Carbon-containing electrodes

Cr_2O_3 (Sigma Aldrich, <100 nm, ~20 m^2 g^{-1}) and chromium nanoparticles (Cr NP, US Research Nanomaterials Inc., ~40 nm, ~24 m^2 g^{-1}) were acquired commercially. Electrodes containing Vulcan XC72 (VC Premetek Inc., ~100 $m^2 \cdot g^{-1}_{Carbon}$) as the conductive matrix and lithium-exchanged Nafion® (LiNafion, Ion Power USA, LITHion™, 7.2 wt% in isopropanol) as electrode binder were fabricated. Li_2O_2 (Alfa

Aesar, Purity > 90%) powder was also ball milled at 500 rpm under argon atmosphere to yield an average particle size of ~345 nm. For $LaCrO_3$ and Cr_2O_3 electrodes, mass ratios were set to ($LaCrO_3$, Cr_2O_3):VC:Li_2O_2:Nafion® = 3:1:1:1 to yield a carbon loading of 0.21±0.05 mg cm^{-2}. For the more conductive and smaller particle Cr NP, components mass ratios were set to (Cr:VC:Li_2O_2:LiNafion = 0.66:1:1:1), and carbon loading to 0.51±0.03 mg cm^{-2}. In the case of chromium oxides $LaCrO_3$, and Cr_2O_3, the large ratio of the promoter was chosen so as to reduce the potential conductivity and surface-area effects of the VC-matrix and maximize the chances of eliciting the enhancement due to the oxide promoter. The expected capacity for complete oxidation of Li_2O_2 in all these electrodes was 1168 $mAh \cdot g^{-1}_{Li2O2}$ = 1168 $mAh \cdot g^{-1}_{carbon}$.

Additionally, VC-only Li_2O_2-preloaded electrodes with a mass ratio of VC:Li_2O_2:LiNafion = 1:1:1 were fabricated for comparison. Lastly, electrodes containing VC, $LaCrO_3$, or Cr_2O_3, LiNafion, but free of Li_2O_2 were fabricated to determine the background oxidation current of electrodes upon charging, which might result from parasitic reactions such as electrolyte oxidation.

Prior to electrode fabrication, VC and chromium promoter powders were dried at 100 °C in a Buchi® B-585 vacuum oven for 24 hours. Transfer to an argon-filled glovebox (MBraun®, H_2O < 0.1 ppm and O_2 < 1%) from the Buchi® glass oven occurred with samples still under vacuum. All fabrication tools were dried at 70 °C overnight prior to use. VC, Cr-based promoters (Cr NP, Cr_2O_3, or $LaCrO_3$), Li_2O_2, and LiNafion were homogenized in anhydrous 2-propanol (IPA) by probe pulse sonication at 40 W for one hour. Electrodes were fabricated by liquid film coating on an aluminum foil using a #50 Mayer rod. O_2-electrodes for Li-O_2 cells (not containing commercial Li_2O_2) were

prepared by coating ultrasonicated inks composed of VC, LiNafion, with and without Cr NP and IPA onto the separator (Celgard C480) inside the argon-filled glovebox. Mass ratio in the oxygen electrodes was set to Cr:VC:Nafion® = 2:1:0.5, which is compared to carbon electrodes of VC:Nafion® = 1:0.5.

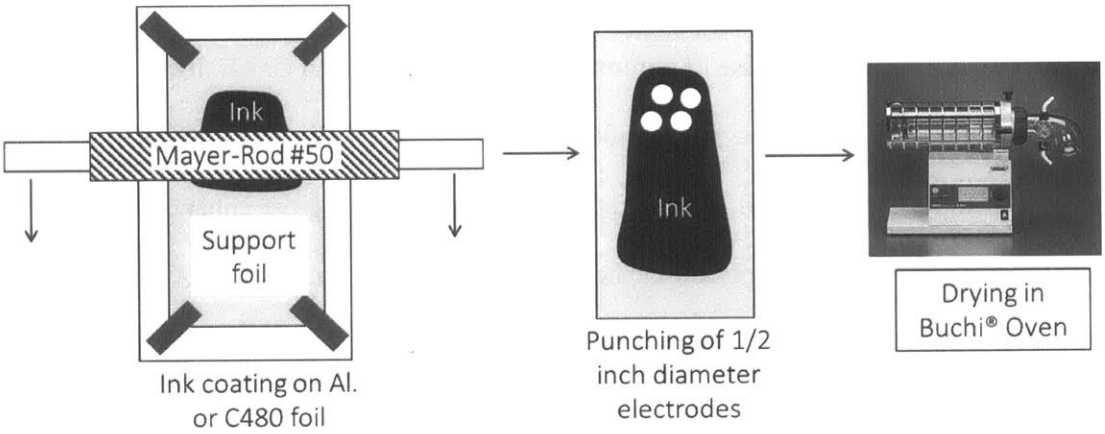

Figure 2-4. Illustration of electrode casting process.

Half-inch-diameter electrodes were punched after complete evaporation of the IPA and dried at 70 °C in the Buchi® vacuum oven for at least 12 hours prior to use (see illustration in Figure 2-4). Dried electrodes were directly transferred to the glove box without exposure to air. Synthesis and handling of electrodes were entirely performed in the argon-filled MBraun® glovebox. No instance of exposure to atmospheric moisture occurred from powder drying to electrode fabrication to cell construction.

Carbon-free electrodes for X-ray absorption (XAS) probing

Carbon-free electrodes of Cr:Li_2O_2 = 0.66:1 were prepared for soft X-ray absorption (XAS) studies. The absence of carbon allowed unambiguous investigation of the effect of Cr on the Li_2O_2 oxidation. Cr NP and Li_2O_2 were mixed at the desired mass ratio (no

added LiNafion binder) and homogenized by sonication in IPA. After homogenization, the slurry was drop casted onto one-centimeter diameter gold disks at a target loading of ~1 $mg_{Cr} \cdot cm^{-2}$. After evaporation of the IPA, two gold disks were stacked, sandwiching the Cr:Li_2O_2 deposit. The sandwich structure is sealed in a heat-seal bag before removing from the glovebox to be pressed at ~600 MPa under a hydraulic press. The gold-supported electrodes prepared entirely under inert argon are dried similarly to the LiNafion-bonded, carbon-containing electrodes before electrochemical and XAS studies.

2.2.3. Cell making and electrochemical testing

The Li_2O_2-preloaded electrodes were charged potentiostatically in a two-electrode cells (TJ-AK; Tomcell Japan Inc.) as described elsewhere.[62] The cells consisted of a stack of metallic lithium anode (Chemetall, Germany, 18 mm diameter), two Celgard 2500 separators (Celgard, USA, 21 mm diameter) and the electrode of study. Separators were wetted with ~125 µL of the electrolyte (0.1 M $LiClO_4$ in DME, Novolyte USA, $H_2O < 20$ ppm). The cells were assembled in the argon-filled glovebox. The activity as measured by specific current towards electrochemical oxidation of Li_2O_2 in presence of each chromium (oxide) promoter was defined as the net oxidation current after subtracting the background oxidation current associated with charging Li_2O_2-free electrodes. An illustration of the background subtraction using the example of $LaCrO_3$ is provided in Figure 2-5. Additionally electrochemical activities as normalized to carbon or promoter surface area are discussed.

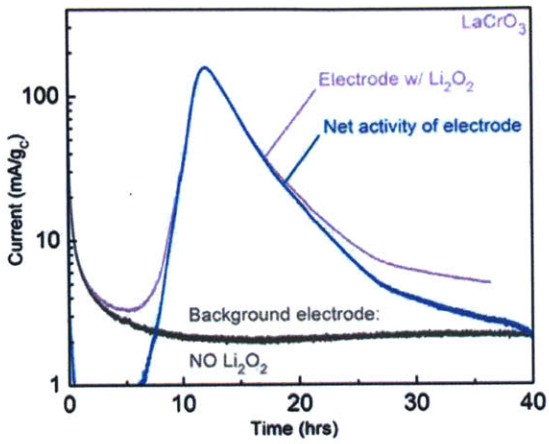

Figure 2-5. Example of background subtraction performed on $LaCrO_3$:VC:Li_2O_2:LiNafion = 3:1:1:1 electrodes at 4.0 V_{Li}. Little change is observed in the final current (net activity of electrode), which highlights the negligible magnitude of parasitic currents compared to actual Li_2O_2 oxidation currents. Negligible and featureless current curves of the electrode with no Li_2O_2 compared to electrode with Li_2O_2 shows that the observed performance of Li_2O_2-preloaded electrodes is due to effective oxidation of Li_2O_2.

Li-O_2 cells consisted of a lithium metal anode (Chemetall, Germany, 15 mm in diameter) and a VC-based O_2 electrode (12.7 mm in diameter). All Li-O_2 single cells were assembled with 0.1 M $LiClO_4$ in DME electrolyte in the glovebox. The assembling procedures of Li-O_2 cells were reported previously.[76] The assembled cells were purged with oxygen for ten minutes before testing. These Li-O_2 cells were tested galvanostatically using a Solartron 1470 (Solartron Analytical, UK).

2.2.4. Electrode characterization

X-ray diffraction (XRD) patterns of $LaCrO_3$ and Cr nanoparticles promoted Li_2O_2-preloaded electrodes were collected before and after charging at 4.0 V_{Li} using a PANanalytical X'Pert Pro^{TM} diffractometer in Bragg-Brentano geometry. XRD was also used to characterize the discharge product(s) of Li-O_2 cells.

The oxidation state of surface chromium in $LaCrO_3$, Cr_2O_3 and Cr NP was probed using X-ray photoelectron spectroscopy (XPS, Physical Electronics Versaprobe II). Spectra collected in the Cr 2p binding energy-range (570 to 600 eV) were analyzed using the CasaXPS software. The electrode morphologies of Li_2O_2-preloaded electrodes before and after charging, and of the O_2-electrode with Cr NP before and after discharge were investigated using a JEOL 6320F high-resolution scanning electron microscope (SEM) at an acceleration voltage of 5 kV.

XAS studies of carbon-free chromium electrodes were performed at the SGM beamline of the Canadian Light Source.[77] O K and Cr $L_{2,3}$ edges spectra were collected in total electron yield (TEY) mode under vacuum below 10^{-7} torr at room temperature. The energy axis was calibrated using the simultaneously measured L_2-edge of metallic Cr. The O K and Cr L-edge absorption were extracted by fitting a first order polynomial in the pre-edge region, extrapolating over the entire range of the spectrum and subtracting this background from the spectrum. The edge height of the XAS was normalized to unity by division of a constant obtained by fitting the post-edge spectrum. Spectra for the as-purchased Cr NP, and the gold-supported Cr:Li_2O_2 electrodes in the pristine, partially charged, and fully charged states were of interest.

2.3. Results and discussion

2.3.1. Electrochemical behavior of Cr-based promoters

We examine the electrochemical net current displayed by electrodes preloaded with commercial Li_2O_2 (Li_2O_2-preloaded) in presence of the chromium (oxides) particles in Figure 2-6. First, the current profile in Li_2O_2-preloaded electrodes display a characteristic dip then rise to a maximum current as seen in Figure 2-5. This phenomenon which will be referred to as electrode activation in this thesis was noted and reported by Harding et al.[62] who tentatively assigned it to the nucleation of active oxidation sites coupled with the presence of a surface impurities. Further discussion of this activation process will be provided in Chapter 3. The current output of electrodes in presence of $LaCrO_3$ ranged from 10 $mA \cdot g^{-1}_{Carbon}$ to 120 $mA \cdot g^{-1}_{Carbon}$ as voltage was toggled from 3.8 V_{Li} to 4.0 V_{Li} (Figure 2-6a). Utilizing Cr NP with higher surface area, much higher mass-specific currents for Li_2O_2 oxidation were found. For the same voltage range of 3.8 V_{Li} to 4.0 V_{Li}, mass normalized current varied between 100 $mA \cdot g^{-1}_{Carbon}$ to 1000 $mA \cdot g^{-1}_{Carbon}$ (Figure 2-6b). Cr NP with a surface area of 24 $m^2 \cdot g^{-1}_{Cr}$ offer an order of magnitude increase in electrochemical activity for Li_2O_2 oxidation compared to $LaCrO_3$ with ~1 $m^2 \cdot g^{-1}_{LaCrO3}$. To ascertain the pattern of high electrochemical activity of Cr-based metal (oxide) promoters towards Li_2O_2 oxidation, $LaCrO_3$, Cr_2O_3, and Cr NP promoted Li_2O_2-preloaded electrodes are compared to a VC-only electrode at 4.0 V_{Li} potentiostatic charging in Figure 2-6c. It is apparent that mass-activity of all three Cr-based promoters is significant greater than that of a non-metal-promoted VC-only Li_2O_2-preloaded electrode. The order of activity was found to be Cr NP > Cr_2O_3 > $LaCrO_3$. At initial observation, this order agrees with the order of specific surface areas of 24, 20, and 1 $m^2 \cdot g^{-1}$ for Cr NP, Cr_2O_3,

and $LaCrO_3$, respectively. Mass-specific activity is found to increase by ~50 times in the presence of Cr NP relative to the baseline non-promoted VC electrode.

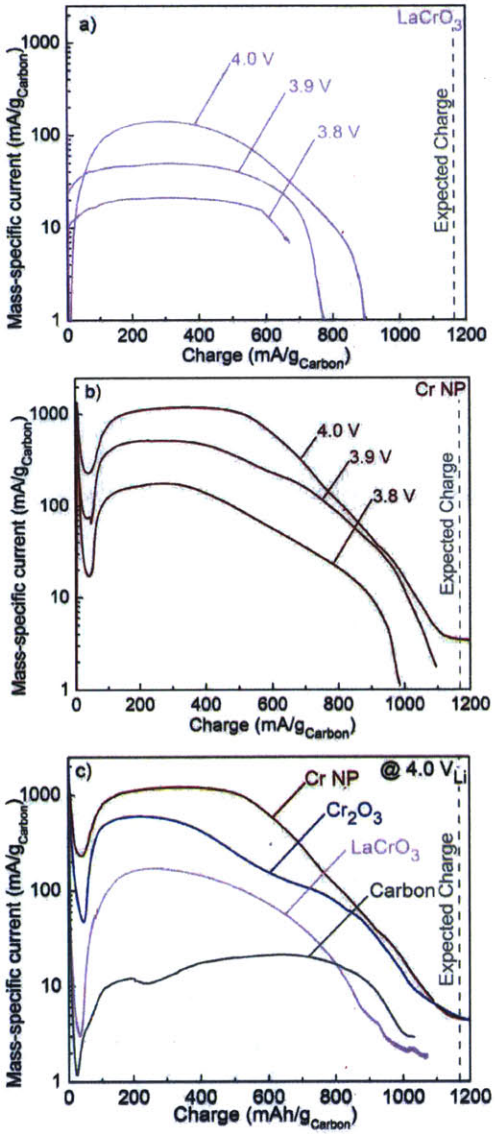

Figure 2-6. Net currents normalized to carbon mass from potentiostatic charging of (a) $LaCrO_3$:VC:Li_2O_2 (3:1:1 mass ratio), (b) Cr-nanoparticles:VC:Li_2O_2 (0.66:1:1 mass ratio) . (c) Mass-specific activity of electrodes with chromium oxides and Cr NP (Cr-Oxide:VC:Li_2O_2 = 3:1:1 and Cr nanoparticles:VC:Li_2O_2 = 0.66:1:1 mass ratio) charged at 4.0 V_{Li}.

It was necessary to spectroscopically and microscopically confirm the effective removal of the preloaded commercial Li_2O_2 in electrodes promoted by Cr-based particles. Using XRD, removal of Li_2O_2 was confirmed in Cr NP, $LaCrO_3$ and VC-only promoted Li_2O_2-preloaded electrodes as shown in Figure 2-7. Furthermore, Utilizing SEM, one can observe the presence of Li_2O_2 particles in pristine (as-made, not yet charged) $LaCrO_3$ and Cr NP Li_2O_2-preloaded electrodes Figure 2-8a, c (blue circle). Once again, post galvanostatic charging, no Li_2O_2 particles can be seen in the electrode structure. SEM evidence of removal of Li_2O_2 by electro-oxidation agrees with XRD measurements showing the disappearance of the spectral features assigned to Li_2O_2 near 34.97 degrees. These measurements once again agree with previous work.[62]

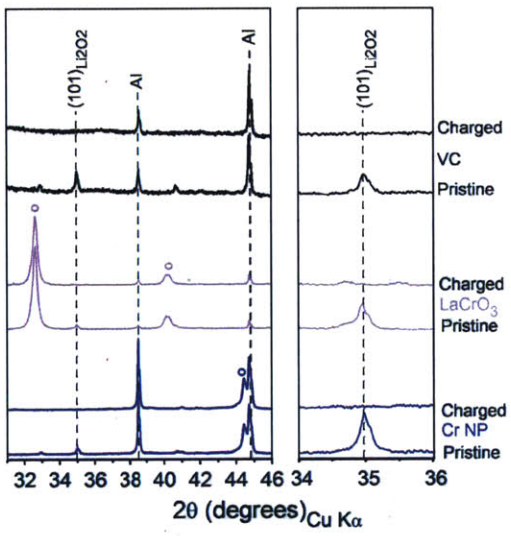

Figure 2-7. XRD patterns of Li_2O_2-preloaded electrodes before and after potentiostatic charging at 4.0 V_{Li} (Figure 2-6c). (Left): XRD scan in the 31 to 46 degrees in 2θ showing the presence of the reflections from the oxide catalysts (open colored circles) and Li_2O_2. (Right): XRD scans magnified in the region with the strongest Li_2O_2 peak

at ~34.97° of Li_2O_2 from the (101) plane which was found to disappear in charged electrodes, indicating effective oxidation of the preloaded commercial Li_2O_2.

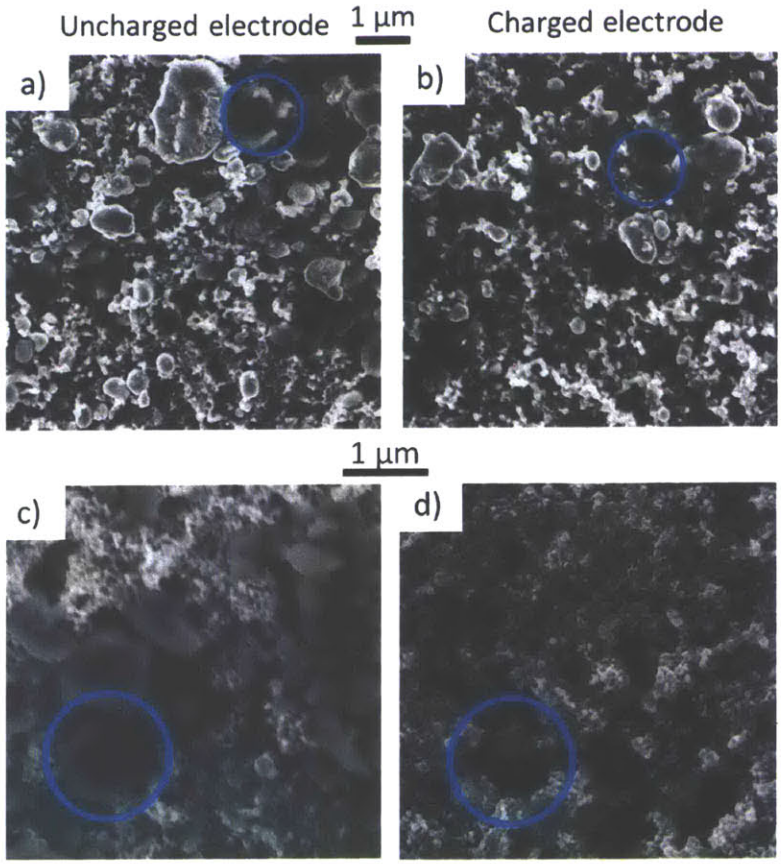

Figure 2-8. SEMs of $LaCrO_3$:VC:Li_2O_2:LiNafion = 3:1:1:1 and Cr:VC:Li_2O_2:Nafion® = 0.66:1:1:1 electrodes with preloaded Li_2O_2. (a, c, left): Pristine electrodes displaying Li_2O_2 and promoter particles surrounded by carbon. (b, d, right): Charged electrodes contains no visible Li_2O_2 particles after completing charging. Blue circle highlights Li_2O_2 particles location. No Li_2O_2 particles are visible by SEM after charging; instead holes corresponding to the ~350 nm Li_2O_2 are observed.

2.3.2. Influence of Cr-based catalysts on the kinetics of Li_2O_2 oxidation.

A potential dependent, Tafel plot, of $LaCrO_3$, Cr_2O_3, and Cr NP is provided in Figure 2-9. The Li_2O_2 electro-oxidation activity of $LaCrO_3$ in Figure 2-9 is of note in that it provides the highest oxidation currents among five perovskites studied,[78] having ~4 times higher area-specific oxidation currents than $Ba_{0.5}Sr_{0.5}Co_{0.8}Fe_{0.2}O_{3-\delta}$ (BSCF) with the record intrinsic activity for oxygen evolution (OER) in aqueous media.[69] The surface area of equivalently ball-milled BSCF particles estimated at ~1.6 $m^2 \cdot g^{-1}_{BSCF}$ was comparable if not greater than the ~1.0 $m^2 \cdot g^{-1}_{LaCrO3}$ of $LaCrO_3$. Although net mass-specific oxidation currents of $LaCrO_3$ (Figure 2-9a) for Li_2O_2 oxidation were lower than those of Pt/C and Ru/C reported previously,[62] the surface-area-specific currents of $LaCrO_3$ (Figure 2-9b) rivals those of Pt/C and Ru/C[62]. The low mass-specific activity of $LaCrO_3$ compared to that of Pt/C and Ru/C is likely due to its much larger particle size (0.5-1 μm for $LaCrO_3$ vs. 3-4 nm for Pt nanoparticles and Ru nanoparticles) and thus lower specific surface area (~1 $m^2\ g^{-1}$ for $LaCrO_3$ vs. ~100 $m^2\ g^{-1}$ for Pt and Ru nanoparticles supported on VC).

The apparent Tafel slopes of Li_2O_2 electrochemical oxidation with the Cr-based promoters were ~250 mV/decades, which are comparable to those of Li_2O_2-preloaded electrodes with VC, Au/C, Pt/C and Ru/C.[62] The physical origin of such large Tafel slopes for Li_2O_2 oxidation is not well understood; it is much larger than the typically quoted 120 $mV \cdot decades^{-1}$ for one-electron reactions such as hydrogen evolution.[79] However, the microkinetics of dissolution of Li_2O_2 are rather complex, involving site nucleations, species diffusion, uncompensated ohmic losses etc. As stated by Viswananthan et al.[80] "The complicated origin of the Tafel curves [in Li-O_2 cells] also

indicates that a traditional Tafel analysis to extract characteristic electrochemical

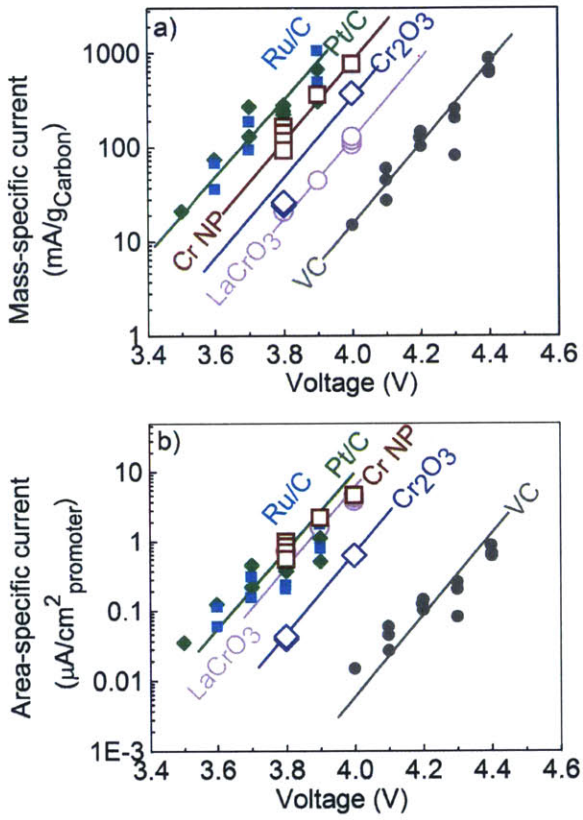

Figure 2-9. (a): Net mass-specific activity vs. potential for $LaCrO_3$, Cr_2O_3, and Cr NP compared to Pt/C, Ru/C and VC-only Li_2O_2-preloaded electrodes reported previously[62] (Cr,Pt,Ru:VC:Li_2O_2 = 0.66:1:1; $LaCrO_3$:VC:Li_2O_2 = 3:1:1, mass ratios) (b): Net surface-area specific activity vs. potential. Specific activity of Cr NP was in good agreement with that of $LaCrO_3$.

parameters is doomed to failure." It should be noted that the ~250 mV·decades^{-1} Tafel slopes during electro-oxidation of commercial Li_2O_2 are considerably smaller than the 300 to 340 mV·decades^{-1} found for charging of Li-O_2 cells following discharge.[42, 51] Possible "poisoning" effects associated with parasitic reaction products formed in Li-O_2

cells such as Li_2CO_3 on the Li_2O_2 surface can be responsible for the greater Tafel slope measured for the charging of electrochemically-formed Li_2O_2 compared to Li_2O_2-preloaded electrodes.

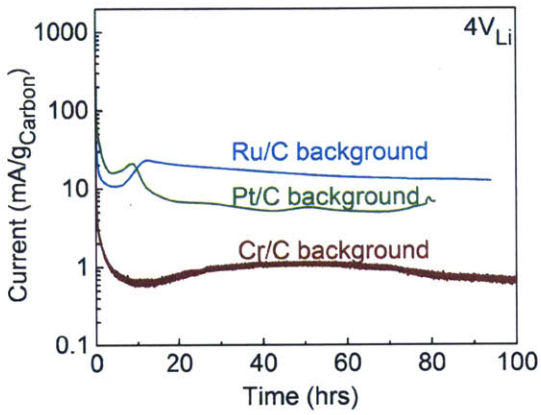

Figure 2-10. Comparison of background oxidation currents at 4 V_{Li} in presence of Cr, Pt and Ru (Cr,Pt,Ru:C:LiNafion = 0.66:1:0.5) without Li_2O_2. The observed parasitic oxidation current is a factor of 10 higher on the surfaces of noble metal Pt and Ru.

Cr NP promoted electrodes are competitive versus noble metal Pt/C and Ru/C in terms of mass-activity (Figure 2-9a) and remained active for Li_2O_2 oxidation at 3.8 V_{Li}. Similar to $LaCrO_3$, the surface area activities of Cr NP are also comparable to those of Pt/C and Ru/C (Figure 2-9b). Unlike Pt/C and Ru/C that promote electrolyte oxidation in addition to Li_2O_2 oxidation,[62] no evidence on the enhanced electrolyte oxidation was found having Cr NP relative to VC. Much lower background oxidation currents of the electrolyte were found in presence of Cr NP as compared to Pt/C and Ru/C (Figure 2-10).

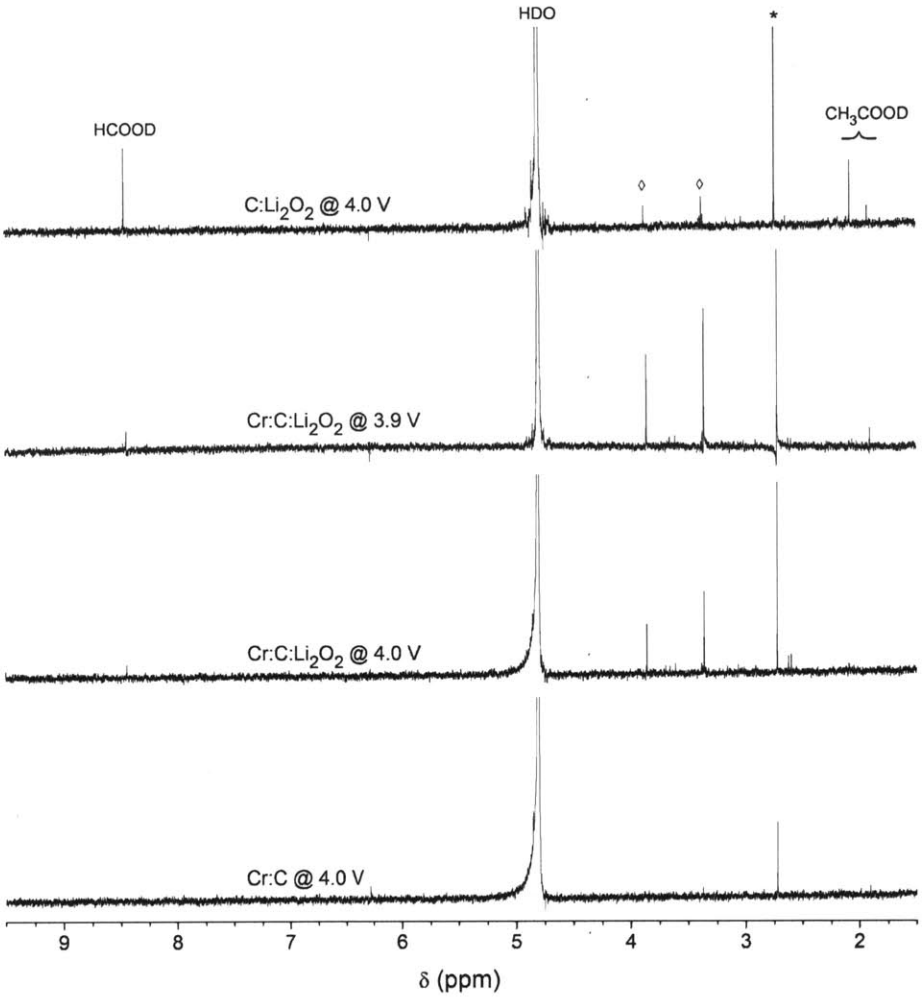

Figure 2-11. (top to bottom) NMR spectra of C:Li_2O_2:LiNafion = 1:1:1 charged at 4.0 V_{Li}, Cr:C:Li_2O_2:Nafion® = 0.66:1:1:1 charged at 3.9 V_{Li}, Cr:C:Li_2O_2:Nafion® = 0.66:1:1:1 charged at 4.0 V_{Li} and Cr:C:LiNafion = 0.66:1:1 polarized at 4.0 V_{Li}. Unidentified peaks at δ = 3.86 and 3.36 ppm (◊) appear tied to the presence of Li_2O_2 as they are absent from the Cr:C:LiNafion without Li_2O_2. These unidentified peaks were also noted in the work by Freunberger et al.[3] The peak at δ = 2.72 (*) is tied to the presence of carbon as it is observed in all electrodes with and without chromium and was not observed in electrodes without carbon (spectrum not shown).

This observation is in agreement with the findings of ^{1}H NMR analysis of organic salts in the charged Cr:C background electrode (without Li_2O_2) (Figure 2-11), which showed the absence of lithium formate (HCOOLi) and lithium acetate (CH_3COOLi)[32, 34] typically found upon electrolyte decomposition. Although lithium formate (HCOOLi) and lithium acetate (CH_3COOLi) were detected by ^{1}H NMR in the charged Cr:C:Li_2O_2 and C:Li_2O_2 electrodes to 4.0 V_{Li}, Cr NP were found not to enhance electrolyte decomposition. This hypothesis is supported by the termination capacity of Cr:C:Li_2O_2 electrodes (Figure 2-6b) being reasonably close (85-98%) to the expected preloaded Li_2O_2 capacity unlike preloaded Li_2O_2 electrodes catalyzed by Pt/C and Ru/C which showed significant overcharge beyond 100% of the expected charge.[62] Minimal electrolyte oxidation is seen using Cr NP as a Li_2O_2 oxidation promoter equally as active as the noble metals.

All Cr-based solid-state promoters display significant activity as measured by surface-area normalized current towards Li_2O_2 electro-oxidation (Figure 2-9b). XPS analysis revealed Cr^{3+} and Cr^{6+} as the oxidation states common to all Cr-based promoters investigated, i.e, $LaCrO_3$, Cr_2O_3 and Cr NP (Figure 2-12a). It is proposed that the mixed valence states of Cr ions on the surfaces of Cr-containing catalysts is involved in promoting Li_2O_2 oxidation kinetics. The fast kinetics for Li_2O_2 oxidation on Cr NP mechanically mixed with VC was further confirmed in Li-O_2 cells discharged and charged at 100 mA g^{-1}_{carbon} (Figure 2-12b). On discharge, of the Cr NP promoted O_2-electrodes showed no enhancement effect of the oxygen reduction to Li_2O_2. A discharge voltage plateau at ~2.7 V_{Li} is observed that is characteristic of the VC conductive support as shown by the black curve of VC-only O_2-electrode matching that of the purple curve

of 67% Cr NP. On charge, however, a voltage plateau occurred at ~3.8 V_{Li} in presence of Cr while the approximately 4.2 V_{Li} was necessary to charge in VC-only O_2-electrodes; a ~400 mV reduction in overpotential was achieved using Cr NP (Figure 2-12b). XRD collected upon discharge of Cr NP promoted electrode shown in Figure 2-13 confirms the formation of desired crystalline Li_2O_2 particles of approximately ~200 nm in size by SEM (Figure 2-14).

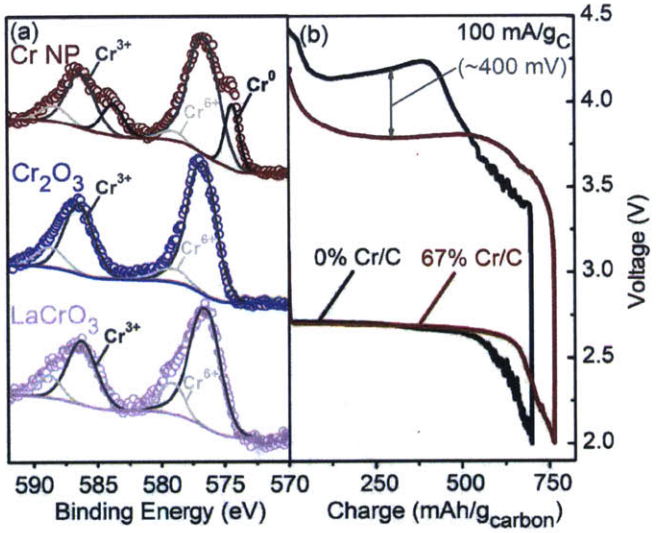

Figure 2-12. XPS spectra of Cr-based catalysts, where the surfaces of Cr NP, Cr_2O_3 and $LaCrO_3$ contain both Cr^{3+} and Cr^{6+}. (b) Discharge and charge voltage profiles of Li-O_2 cells with Cr NP (Cr NP:VC:Nafion® = 2:1:0.5) and VC (VC:Nafion® = 1:0.5) in the oxygen electrode tested at 100 mA g^{-1}_{carbon}.

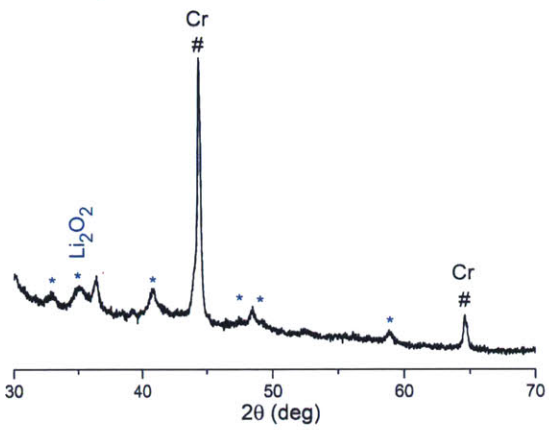

Figure 2-13. Post-discharge XRD of Cr:C (Cr:C:LiNafion = 2:1:1) Li-O_2 electrode. The discharge is confirmed to be crystalline Li_2O_2.

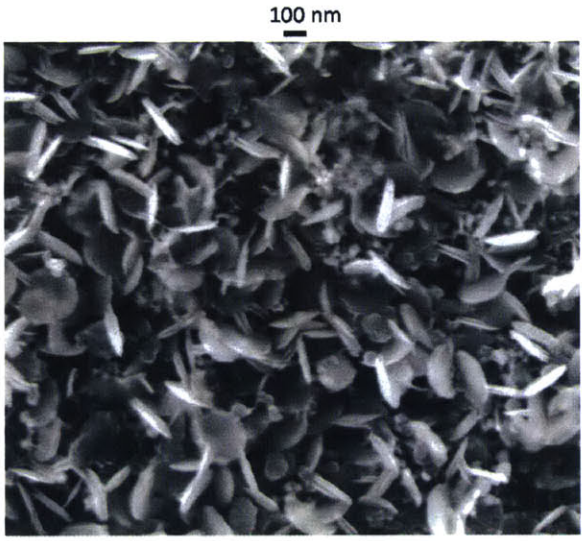

Figure 2-14. SEM of discharged Cr:C (Cr:C:LiNafion = 2:1:0.5) Li-O_2 electrode. ~200 nm particles of Li_2O_2 confirmed by XRD (Figure 2-13) are visible and covering the carbon structure. Smaller ~40 nm point-particles are Cr NP.

2.3.3. Proposed mechanism for enhanced Li_2O_2 oxidation kinetics with Cr.

At this stage of experimental investigation, we postulate that the kinetics of Li_2O_2 oxidation is influenced by the ability to promote the presence of oxygen-rich $Li_{2-x}O_2$ species to enhance electron transfer in the first-electron-oxidation step can be rate-limiting ($Li_2O_2 \rightarrow LiO_2 + Li^+ + e^-$). Oxygen-rich Li_2O_2 surfaces have been shown by density functional theory calculations to be half-metallic.[39, 81] LiO_2-like species can disproportionate chemically or get oxidized electrochemically to evolve O_2 gas.[43, 51] Upon the formation of LiO_2-like surfaces ($Li_{2-x}O_2$),[43, 51] further decomposition can proceed through disproportionation reactions ($2LiO_2 \rightarrow Li_2O_2 + O_2$) or through further oxidation of the LiO_2-like species. This hypothesis is relevant to but different from previous work,[41] which has suggested enhanced transport of Li_xO_2 and not necessarily enhanced electron transfer to be responsible for greater kinetics for Li_2O_2 oxidation on Co_3O_4. The following observations are provided in support of this hypothesis: (i) oxidation of very thin Li_2O_2 (< 1 nm in thickness),[18, 50-53] where electron transfer to the Li_2O_2 surface can be facilitated by electron tunneling,[52] occurs at low charge potentials of ~3.3 V_{Li}. (ii) charging Li_2O_2 deposits (with particle sizes of 10-20 nm) at exceptionally low rates (5 mA g^{-1}_{CNT} or 0.001 μA cm^{-2}_{CNT})[42] can proceed at ~3.3 V, where electron transfer in the first-oxidation step is no longer limiting. (iii) it is been shown that facilitating electron transfer to Li_2O_2 using molecular catalysts can lower the charge voltages to ~3.5 V.[60, 61] Moreover, we use XAS data of charged electrodes to show the redox of $Cr^{3+} \leftrightarrow Cr^{6+}$ and possible formation of LiO_2 superoxide, which will discussed below.

XAS analysis of charged preloaded Li_2O_2 electrodes with Cr NP revealed that the oxidation of Cr^{3+} to Cr^{6+} accompanied Li_2O_2 oxidation. Carbon-free, preloaded Li_2O_2 electrodes were used in these XAS experiments, which had comparable Li_2O_2 oxidation current densities normalized to the mass of Cr NP compared to electrodes with VC, as shown in Figure 2-15. The XAS O K and Cr $L_{2,3}$-spectra of as-purchased Cr NP, pristine, partially charged, and fully-charged Cr:Li_2O_2 supported on Au electrodes are shown in Figure 2-16. Both O K and Cr $L_{2,3}$ spectra of as-purchased Cr NP resemble those of Cr_2O_3 reported in the literature,[82-84] (see Figure 2-17) indicating pronounced oxidation on the surface of Cr NP in agreement with XPS results in Figure 2-12a.

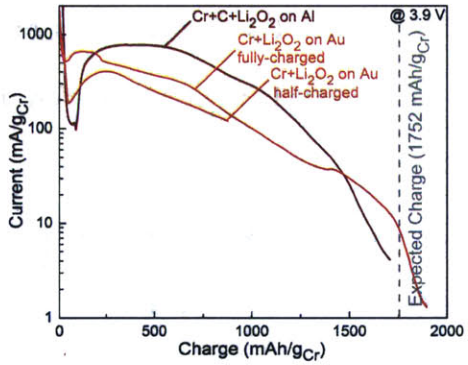

Figure 2-15. Currents normalized to Cr NP mass from potentiostatic charging of Cr NP:VC:Li_2O_2 (0.66:1:1 mass ratio) and carbon-free Cr NP:Li_2O_2 (0.66:1 mass ratio) pressed into Au disk The carbon-free electrodes were used for XAS.

Pristine (not yet charged) Cr:Li_2O_2 electrodes showed the expected features of both Cr NP and Li_2O_2 (Figure 2-16). After partially charging the electrodes, new peaks labeled (1), (2) and (3) in the O K-edge (Figure 2-16a) and (4) and (5) in the Cr $L_{2,3}$-edges (Figure 2-16b) appeared. Using the reference spectra of Li_2CO_3,[16] Li_2O_2,[42, 85] and LiO_2,[86] after appropriate shifts to a common energy scale (Figure 2-18), Peak (1) could be

attributed to ligand hole in the O p band associated with Cr^{6+} (ref. [87]) or the π^* resonance of superoxide $(O=O)^-$ bonds such as in LiO_2,[86, 88] which may have formed on Li_2O_2 oxidation.[51] This presence of Cr^{6+} is further supported by the presence of peaks (4) and (5) in the Cr L_3 and L_2 edges, which is characteristic to Cr^{6+}.[89]

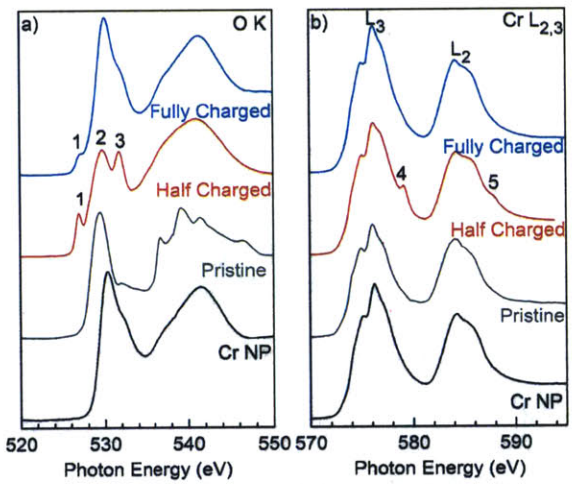

Figure 2-16. XAS TEY spectra at the O K and Cr $L_{2,3}$ edges for as-purchased Cr NP, pristine, half-charged, and fully charged carbon-free Cr:Li_2O_2 electrodes. Electrochemical data for the half-charged and fully-charged Cr:Li_2O_2 electrodes are shown in Figure 2-15. Energies are calibrated to the Cr L_2-edge positions. Processing of spectral intensities is described in the experimental section.

Peak (2) results from the convolution of pre-edge features of Li_2O_2 and ligand hole in the O p band associated with Cr^{3+} such as Cr_2O_3 appearing around 530 eV, and (3) can be assigned to Li_2CO_3 formed from electrolyte decomposition during charging. Upon complete charging of the Cr:Li_2O_2 electrode, peaks (2), (3), (4), and (5) disappeared but peak (1) remained (Figure 2-16a). The XAS evidence of Cr^{3+} oxidation to Cr^{6+} and possible formation of LiO_2 support the previous hypothesis that the kinetics of Li_2O_2

oxidation can be enhanced by the rate-limiting step in the first delithiation step ($Li_2O_2 \rightarrow LiO_2 + Li^+ + e^-$).[90] The ability of Cr NP to accommodate mixed valence states on the surfaces can facilitate electron removal from Li_2O_2 through the redox of $Cr^{3+} \leftrightarrow Cr^{6+}$ during the first-electron oxidation step, promoting the Li_2O_2 oxidation kinetics.

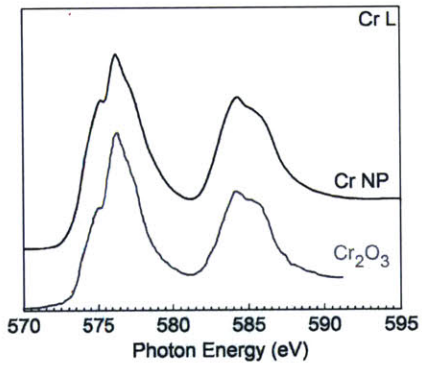

Figure 2-17. Cr L edge TEY XAS of Cr nanopowder versus Cr_2O_3. Both edges show that the surfaces of Cr is oxidized to Cr^{3+} in a Cr_2O_3-like environment. This observation is corroborated by XPS as reported previously.

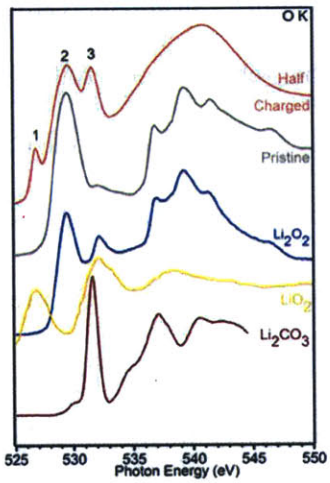

Figure 2-18. Comparison of O K-edge XANES spectra of the pristine and half-charged Cr:Li_2O_2 electrodes to reference spectra of Li_2CO_3,[16] Li_2O_2,[42, 85] and LiO_2.[86] Energies are calibrated to the spectral features of Li_2O_2 in the as-made Cr:Li_2O_2 electrode.

2.4. Conclusions

In this chapter, the significant influence upon charging of Cr-based promoters on the electrochemical oxidation of Li_2O_2, the discharge product of Li-O_2 batteries was probed using electrochemical measurements, SEM, XRD, XPS, and XAS. Cr-based promoters such as $LaCrO_3$, Cr_2O_3 and Cr NP with oxidized surfaces, which have negligible activity for aqueous OER, have shown surface-area-specific Li_2O_2 oxidation activities that rival that of highly active noble metal catalysts such as Pt/C and Ru/C but without promoting electrolyte oxidation. The mass-specific activity of Cr NP is ~50 times higher than VC, and remained active for Li_2O_2 oxidation at 3.8 V_{Li}. Such facile kinetics for Li_2O_2 oxidation is confirmed in Li-O_2 cells, where a significant ~400 mV reduction on the charging voltage is achieved in presence of 40-nm Cr NP mechanically mixed with VC. At this stage, it is tentatively proposed that the ability of Cr-compounds to accommodate mixed valence states of Cr^{3+} and Cr^{6+} ions on their surfaces can promote Li_2O_2 oxidation kinetics by facilitating electron removal necessary to carry out the first-electron oxidation step of Li_2O_2 to LiO_2-like species. XAS data of pristine, partially charged, and fully charged electrodes support this hypothesis by revealing $Cr^{3+}\leftrightarrow Cr^{6+}$ interconversion at different stages of Li_2O_2 oxidation and possible formation of oxygen species akin to LiO_2-superoxide.

Chapter 3. Mechanistic understanding of the solid-state activation of Li_2O_2 oxidation

Adapted with permission from K. P. C. Yao, M. Risch, S. Y. Sayed, Y.-L. Lee, J. R. Harding, A. Grimaud, N. Pour, Z. Xu, J. Zhou, A. Mansour, F. Bardé and Y. Shao-Horn, Solid-state activation of Li_2O_2 oxidation kinetics and implications for Li-O_2 batteries, *Energy Environ. Sci.*, 2015, **8**, 2417.

3.1. Introduction

In Chapter 2, the strong influence of Cr-based metal (oxide) particles was observed and tied to interconversion of the transition metal oxidation state from Cr^{3+} to Cr^{6+}. In this chapter, we will examine trends in electrochemical activities of several transition metal compounds and search for correlations to potentially explain the origin of the promoter transition metal effect on the dissolution of Li_2O_2. Let us start by providing some background on efforts to understand the origin of "catalysis" in Li_2O_2 oxidation. The kinetics of Li_2O_2 oxidation in Li-O_2 batteries have been investigated by a number of groups,[44, 49, 50, 91, 92] who show that the charging performance is strongly impacted by the morphology of the Li_2O_2 produced during discharge. For thin layers of Li_2O_2, McCloskey *et al.* have computed[44, 50] and experimentally measured low charging overpotentials (< 0.2 V by cyclic voltammetry) to posit that electrocatalysis for the oxygen evolution reaction (OER) from Li_2O_2 oxidation may not be necessary.[91, 92] Similarly, Lu *et al.*[18, 49] have reported evidence showing that electrocatalysis is unnecessary during the removal of the first sub-nanometer of deposited Li_2O_2, where electrochemical oxidation of Li_2O_2 can proceed from first delithiation to form lithium-deficient $Li_{2-x}O_2$ followed by oxygen evolution from $Li_{2-x}O_2$. This concept is consistent with DFT findings[43] and recent results by Ganapathy *et al.*[93] showing solid-solution lithium deficient $Li_{2-x}O_2$ using *in operando* X-ray diffraction during charge.

Thicker deposits of Li_2O_2 (*i.e.* greater depth of discharge) have been shown to require greater overpotentials to oxidize, particularly on carbon electrodes.[22, 24, 41, 49, 56, 94, 95] This phenomenon is attributed to two different effects: (1) the formation of byproducts during discharge that require a greater potential to oxidize[22-24, 32, 96] and (2) the insulating nature

of Li_2O_2, which increases the potential needed to drive the oxidation reaction.[25, 38, 39, 52] One group of the main byproducts is carbonates such as Li_2CO_3, which can form from electrolyte decomposition and/or from an interaction between Li_2O_2 and carbon electrodes.[23, 24] High charging overpotentials (typically greater than 1 V) have been reported for a variety of carbon electrodes, from simple porous carbon[24, 49, 94] to graphene,[95, 97] to carbon nanofibers[56] and nanotubes[22] at moderate rates 50 to 100 $mA \cdot g^{-1}_{carbon}$. In contrast, several groups have reported improved charging performance when carbon-free electrodes were used, such as nanoporous gold,[58] TiC,[21] and Ru on $TiSi_2$.[98] Regarding, the insulating nature of Li_2O_2, Viswanathan *et al.*[52] have estimated that 5-10 nm layers of insulating Li_2O_2 is sufficient to drive overpotentials greater than 0.6 V.

Several reports have shown that the addition of metal nanoparticles (using either noble or transition metals) show a quantifiable reduction in charging overpotential,[41, 62, 78, 94, 99-104] and can enhance the kinetics of the Li_2O_2 oxidation reaction, yet the origin of this enhancement is not fully understood. No soluble species derived from solid Li_2O_2 have yet been identified on charge using electron paramagnetic resonance,[105] Raman,[106] and rotating ring-disk techniques,[107, 108] which would support a heterogeneous catalysis mechanism.[109] McCloskey *et al.* attribute the measured enhancement to the catalysis of electrolyte decomposition and efficient removal of parasitic products.[91] In addition, Black *et al.*[41] proposed that catalyst surfaces promote efficient transport of $Li_{2-x}O_2$ species on the electrode surfaces. Moreover, experiments with soluble redox mediators[60] such as tetrathiafulvalene,[61] 2,2,6,6-tetramethylpiperidinyloxyl,[110] and iodine[111] have shown to greatly reduce the overpotential required to charge Li-O_2 batteries, which suggests that the Li_2O_2 oxidation kinetics can be directly influenced by redox exchange with a

promoter for surface charge transfer. In summary, it is not yet understood how solid-state metal nanoparticles can alter the reaction pathways and enhance the kinetics of Li_2O_2 oxidation.

Similar to Chapter 2, we examine the enhancement of Li_2O_2 oxidation kinetics with metal nanoparticles of Co, Mo, Cr and Ru using electrodes preloaded with commercial crystalline Li_2O_2 in both carbon-free and carbon-containing electrodes.[62, 78] Using Li_2O_2-loaded electrodes minimizes the interference of catalyst-dependent parasitic discharge products[22, 32] as well as crystallinity and morphology variations in electrochemically formed Li_2O_2[104] on the Li_2O_2 oxidation kinetics. As the surfaces of these nanoparticles are likely oxidized, we also compare the activation of Li_2O_2 oxidation kinetics using corresponding metal oxides including MoO_3, Cr_2O_3, RuO_2, Co_3O_4, and α-MnO_2. *Ex situ* X-ray absorption spectroscopy (XAS) and inductively coupled plasma atomic emission spectra (ICP-AES) of electrodes before and after charging are used to provide insights into processes potentially responsible for the activation of Li_2O_2 kinetics. Correlating the enhanced Li_2O_2 oxidation kinetics with the enthalpy of conversion $Li_2O_2 + M_aO_b \pm O_2 \rightarrow Li_xM_yO_z$ allows us to propose a unifying descriptor and a pathway for the solid-state activation of Li_2O_2 electro-oxidation activity across transition metal nanoparticles and oxides. In light of our proposed mechanism, we refer to the added nanoparticles as "promoters" throughout the text.

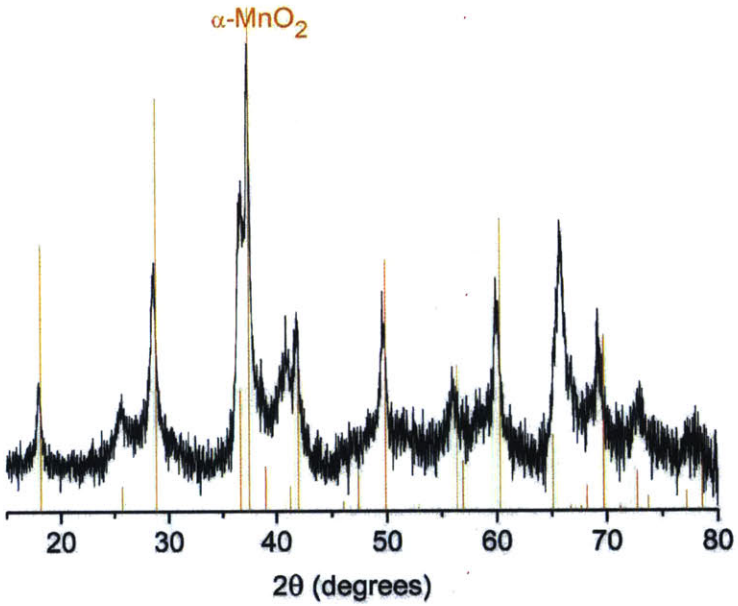

Figure 3-1. X-ray diffraction pattern of in-house synthesized α-MnO_2 nanowires. All major peaks of α-MnO_2 are resolved confirming the effective synthesis of the intended phase.

3.2. Experimental

3.2.1. Electrode preparation

The electrochemical oxidation kinetics of Li_2O_2 were studied using promoters including metal nanoparticles of Mo (US Research Nanomaterial Inc., Purity = 99.9%, SSA_{BET} = 4 $m^2 \cdot g^{-1}$), Cr (US Research Nanomaterial Inc., 99.9%, 26 $m^2 \cdot g^{-1}$), Co (US Research Nanomaterial Inc., 99.8%, 21 $m^2 \cdot g^{-1}$), Ru (Sigma Aldrich, ≥ 98%, 23 $m^2 \cdot g^{-1}$), Mn (American Elements, Mn_3O_4 shell, 99.9%, 24 $m^2 \cdot g^{-1}$) and metal oxide particles of MoO_3 (Sigma Aldrich, 99.98%, 1.8 $m^2 \cdot g^{-1}$) Cr_2O_3 (Sigma Aldrich, 99%, 20 $m^2 \cdot g^{-1}$), Co_3O_4 (Sigma Aldrich, 99.5%, 36 $m^2 \cdot g^{-1}$), RuO_2 (Sigma Aldrich, 99.9%, 16.2 $m^2 \cdot g^{-1}$) nanoparticles and α-MnO_2 nanowires,[112] (Synthesized, SSA_{BET} = 85 $m^2 \cdot g^{-1}$, X-ray

diffraction pattern provided in Figure 3-1). BET surface areas were determined using a Quantachrome ChemBET. Carbon-free, gold-foil (Sigma Aldrich, 99.99%) supported, and carbon-containing, aluminum-foil (Targray Inc.) supported electrodes were entirely prepared in an argon-filled glovebox (MBraun, water content < 0.1 ppm, O_2 content < 1%). All fabrication tools were dried at 70 °C prior to use. All nanoparticles and Vulcan XC72 carbon (Premetek, ~100 $m^2 \cdot g^{-1}$) were dried under 30 mbar vacuum, at 100 °C, in a Buchi® B585 glass oven and transferred into the glovebox without further exposure to air.

Carbon and binder free gold-supported electrodes, having a fixed promoter:Li_2O_2 mass ratio of 0.667:1, were prepared using the following method reported previously.[78] Due to embrittlement of the gold foil in presence of Mo, Mo-promoted electrodes were deposited on battery grade aluminum foil. Masses of 10 mg promoter and 15 mg of ball-milled Li_2O_2 (Alfa Aesar, ≥ 90%, ~345 nm after ball-milling) were mixed in 1 mL anhydrous 2-propanol (IPA, Sigma Aldrich, 99.5%) and horn-sonicated at 50% pulses of 30 W for 30 minutes. After sonication, 40 µL of the slurry is dropcasted onto ½ inch diameter gold foil, resulting in a material loading of ~0.8 $mg \cdot cm^{-2}$. Upon evaporation of the IPA, the gold disk was enclosed between two dried aluminum sheets and sealed in an argon-filled heat-seal bag. The sealed bag was removed from the glovebox and pressed at 5 tons under a hydraulic press to secure the promoter:Li_2O_2 mixture onto the gold foil.

Carbon-containing electrodes, with Vulcan XC72 carbon as electrically conducting backbone, were deposited on battery grade aluminum foil at a mass ratio of promoter:VC:Li_2O_2:LiNafion binder = 0.667:1:1:1 using a #50 Mayer rod.[62, 78] Prior to ink casting, 75 mg of Vulcan XC72, 50 mg of promoter, 75 mg of Li_2O_2, and 75 mg

equivalent of IPA-dispersed lithium-substituted Nafion (LiNafion, Dupont) were horn-sonicated in IPA at 50% pulses of 30 W for 30 minutes. All electrodes were dried at 70 °C in the Buchi® vacuum oven for a minimum of 12 hours and transferred into the glove box without ambient exposure. The fabrication of electrochemical cells was performed without atmospheric exposure in an Argon-filled glovebox (Mbraun, $H_2O < 0.1$ ppm, $O_2 < 0.1\%$).

3.2.2. Electrochemical testing

The oxidation kinetics of Li_2O_2 was studied in electrochemical cells consisting of an 18 mm diameter lithium foil (Chemetall Germany), 150 µL of 0.1 M $LiClO_4$ in 1,2 dimethoxyethane (0.1 M $LiClO_4$/DME, BASF, $H_2O < 20$ ppm by Karl Fischer titration), two pieces of Celgard C480, and an Li_2O_2-preloaded electrode. These cells were tested potentiostatically using a VMP3 potentiostat (BioLogic Inc.).

3.2.3. X-ray absorption spectroscopy (XAS)

Ex situ X-ray absorption spectroscopy was performed at the SGM beamline of the Canadian Light Source at first-row transition metal L edges in vacuum. Molybdenum L edges were recorded in vacuum at the SXRMB beamline of the Canadian Light Source and in a helium atmosphere at the 9-BM-B beamline station at the Advanced Photon Source. Chromium K-edges were collected in a helium atmosphere at beamline X11A of the National Synchrotron Light Source. All spectra were acquired in the surface sensitive electron yield mode at room temperature. The spectra were processed as reported previously.[78, 113] Energy axes are calibrated to appropriate metal references. The promoter metal (Mo, Cr, Co, Mn) L-edges were collected for the nanoparticle powder, a pristine

electrode, a partially charged electrode, and fully charged electrode. Mo L edge spectra of MoO_2 (Alfa-Aesar, 99%), MoO_3 (Sigma Aldrich, 99.98%), Li_2MoO_4 (Alfa Aesar, 99.92%), Mo foil (Sigma Aldrich, 99.9%) and Cr K edge K_2CrO_4 (Alfa Aesar, 99%) were collected and used as references.

3.2.4. Inductively coupled plasma atomic emission spectra (ICP-AES)

Inductively coupled plasma atomic emission spectra (ICP-AES) were collected from the electrolyte after electrochemical oxidation of Li_2O_2 in presence of Mo, Cr, Co, Co_3O_4, and α-MnO_2. As any dissolution of transition-metal-containing species could plate on the lithium anode, we utilized "2-compartment" cell reported by Gasteiger et al.,[114] which consists of lithium foil||Celgard C480 with 50 µL 0.1 M $LiClO_4$/DME||Ohara solid electrolyte||Celgard C480 with 100 µL 0.1 M $LiClO_4$/DME||Carbon-free Li_2O_2-loaded electrode. The C480 separator in contact with the Li_2O_2 electrode was collected post charging, and was immersed in DME (BASF, H_2O < 20 ppm by Karl Fischer titration), which was combined with DME that was used to rinse the surface of the solid electrolyte for a total of 3 mL DME. The resulting DME solution was then centrifuged at 7000 rpm for 10 minutes to remove solid particulates, which was pipetted subsequently out into a new vial and evaporated slowly at 40 °C on a hot plate. 0.5 mL of 37 wt% HCl was added to the dried vial to dissolve any solid precipitates, which was then evaporated slowly on a hot plate. Finally, the vial was rinsed with 10 mL of 2 wt% nitric acid (Sigma Aldrich, TraceSelect®) to create the ICP sample. ICP standards at 0, 1, 2, and 5 ppm were also generated for Mo (RICCA CHEMICAL COMPANY® 1000 ppm in 3% HNO_3 with trace HF), Cr, Co, and Mn from standard solutions (Fluka TraceCERT®, 1000 ppm in 2% HNO_3). ICP-AES data were collected using a Horiba ACTIVA-S spectrometer.

3.3. Results and discussion

3.3.1. Increased Li_2O_2 oxidation kinetics with nonprecious transition metal nanoparticles

Carbon-containing and carbon-free Li_2O_2-loaded electrodes promoted by bulk transition metals nanoparticles Mo, Cr, Ru, Co, and Mn were examined, which revealed high activities of group VI Mo and Cr nanoparticles. Figure 3-2a compares the gravimetric Li_2O_2 oxidation current (normalized per mass of promoter) of Cr and Mo compared to Co, Mn, and Ru in carbon-containing electrodes at 3.9 V vs. Li (V_{Li}). Cr and Mo were found to exhibit activities on the orders of 1000 $mA \cdot g^{-1}_{Promoter}$ at 3.9 V_{Li}, which is comparable to noble metal Ru in this work and previous studies,[62] and more than an order of magnitude greater than those of Co and Mn. This enhancement of the Li_2O_2 oxidation kinetic is confirmed, in Figure 3-3, during galvanostatic charging at 100 $mA \cdot g^{-1}_{Carbon}$ after discharge where approximately 600 and 200 mV reduction in the charging voltage compared to the base carbon support is observed for Mo and Cr electrodes, respectively. Once again, it is observed that the discharge voltage plateau at 2.7 V_{Li} is independent by the presence of the metal promoter. Mo-promoted electrodes had higher oxidation currents than those by Cr at 3.7, 3.8, and 3.9 V_{Li}, as shown in Figure 3-2b; complete voltage profiles vs. time and capacity are provided in Figure 3-4. We further analyzed the gravimetric oxidation currents of Li_2O_2 promoted by Mo, Cr, Ru, Co, and Mn in carbon-free electrodes (Figure 3-2c), where a similar trend of Mo > Cr ≈ Ru > Co > Mn to that shown in Figure 3-2a was observed. This result suggests that the reported reactivity of Li_2O_2 with carbon support[23, 115] does not alter the metal promoter activity trend as examined at 3.9 V_{Li}. Furthermore, this result cannot be explained by the

hypothesis previously reported by McCloskey *et al.*[91] that kinetic enhancement of the Li_2O_2 oxidation by carbon-supported Pt, MnO_2 and Au during Li-O_2 cells charging is mainly an artefact of enhanced removal of parasitic discharge products

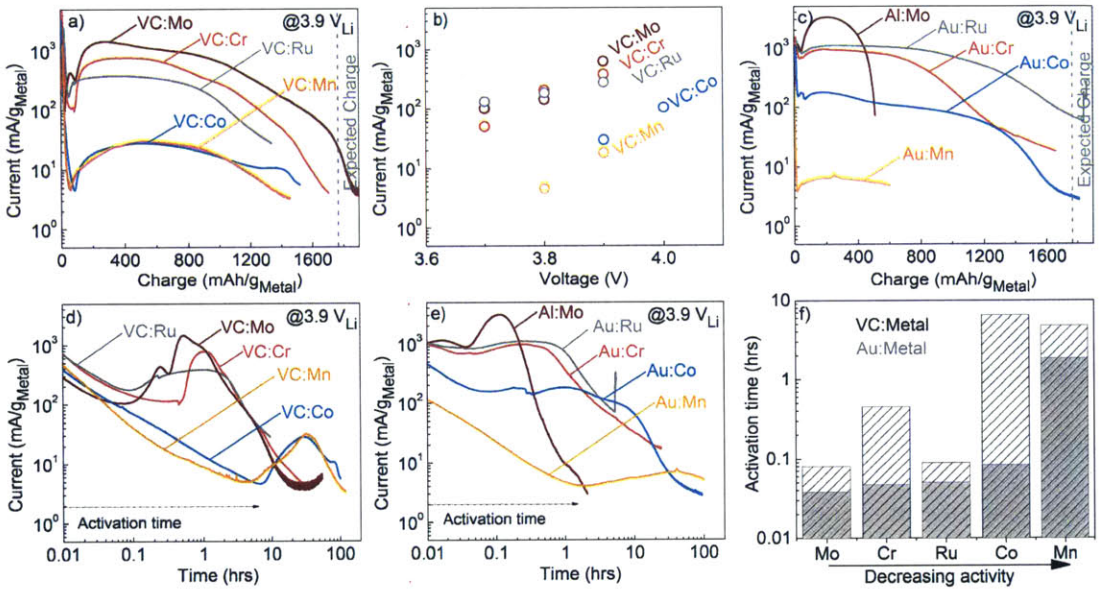

Figure 3-2. Electrochemical performance of metal nanoparticles carbon-containing VC:promoter:Li_2O_2:LiNafion = 1:0.667:1:1 and carbon-free promoter:Li_2O_2 = 0.667:1 (mass ratios) electrodes at 3.9 V_{Li}. (a) Current normalized per mass of promoter *vs.* capacity for carbon-containing electrodes. (b) Potential dependent current normalized per mass of promoter at 3.7, 3.8, 3.9 and 4.0 V_{Li}. (c) Current per mass of promoter *vs.* charge in carbon-free electrodes. (d), (e) Current per mass of promoter *vs.* time for carbon-containing and carbon-free electrodes, respectively. (f) Activation time in carbon-free *vs.* carbon-containing electrodes. Note that aluminium foil was used as support for carbon-free Mo electrodes due to embrittlement of the Au support in presence of Mo.

since the significant sources of Li_2CO_3 (electrolyte decomposition and carbon support[23]) were circumvented using preloaded (to avoid discharge) and carbon-free electrodes (to avoid high-voltage carbon corrosion). We note that considerably lower capacities than the expected (1168 $mAh \cdot g^{-1}_{Li2O2} \equiv$ 1751 $mAh \cdot g^{-1}_{metal}$) were observed for carbon-free Mo-promoted electrodes while recharge was reasonably complete in carbon and binder containing electrodes (purple curve in Figure 3-2a vs. Figure 3-2c). This can be tentatively attributed to poor mixing of high-density Mo nanoparticles (10.3 $g \cdot cm^{-3}$) and the lower-density Li_2O_2 (2.31 $g \cdot cm^{-3}$) in isopropanol prior to fabrication of the carbon-free electrode. However, reactivity of Mo towards Li_2O_2 might also be the source of reduced oxidation capacity as seen later in this chapter.

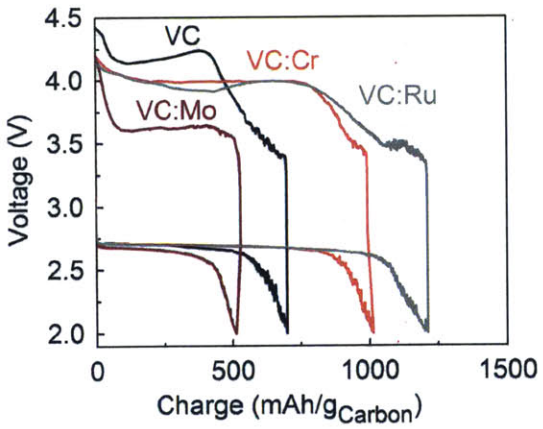

Figure 3-3. Galvanostatic performance of carbon-containing VC: promoter:LiNafion = 1:0.667:1 (mass ratios) O_2-electrodes at 100 $mA \cdot g^{-1}_{Carbon}$. The increased activity of Cr and Mo promoted is confirmed during charging after discharge (in operando formation of Li_2O_2 followed by its oxidation).

The current profile versus time for the same five representative metal nanoparticle promoters are further analyzed in Figure 3-2d, e, f. The time delay incurred from the start

of charging up to the first local minimum (initial current dip) is designated as "activation time" and graphed in Figure 3-2f for carbon-free and carbon-containing electrodes. Except for Mn, the delay in electrode activation increased from carbon-free to carbon-containing electrodes from the order of tens of minutes in the absence of carbon to the order of hours in presence of a carbon support. This difference is likely due to the reactivity between carbon and Li_2O_2[23, 24, 35] resulting in the formation of a Li_2CO_3 coating on the Li_2O_2 particles in the carbon-containing electrodes, which both decreases the exchange current of the Li_2O_2 oxidation reaction[23] but also presents a high reversible redox potential of 3.5 V_{Li}[116] adversarial to its oxidative removal.[26] This phenomenon is well illustrated in the work of Thotiyl *et al.*[21, 24] showing as much as a 40-fold increase in Li_2CO_3 formation using a carbon electrode compared to a carbon-free TiC electrode. The impaired kinetics of Li_2O_2 oxidation in carbon-containing electrodes as compared to carbon-free electrodes reinforces the general trend of improved cell performance and cycling in carbon-free electrodes such as TiC[21] and nanoporous gold.[58] Noteworthy is the general reduction in activation time (and time to current maximum) as the promoter activity increases. The delay prior to rise to peak current follows activity, hinting at more rapid nucleation of active species at the interface of the promoter and reactant Li_2O_2 for higher activity electrodes.

Metal oxides including MoO_3, Cr_2O_3, RuO_2, Co_3O_4 and α-MnO_2, were investigated in carbon-containing electrodes (Figure 3-5). Interestingly, the spread in the gravimetric activity among all the oxides examined is much smaller than that found for metal nanoparticles. This clustering of activities in the metal oxide was similarly observed using perovskites $Ba_{0.5}Sr_{0.5}Co_{0.8}Fe_{0.2}O_{3-\delta}$, $LaCrO_3$, $LaNiO_3$, $LaFeO_3$, and $LaMnO_{3+\delta}$.[78] In

addition, the gravimetric activities of metal oxides are lower than those of transition metals presented in Figure 3-2a, especially for Cr and Mo-based particles. Moreover, in agreement with the "activation time" trend observed for metal nanoparticles, the delay to the Li_2O_2 oxidation current peak increases as activity decreases for the metal oxides (Figure 3-5b). We note the activity of α-MnO_2 at 3.9 V_{Li} herein is in agreement with the work of Kavakli *et al.*[101] using similarly preloaded electrodes and rates.

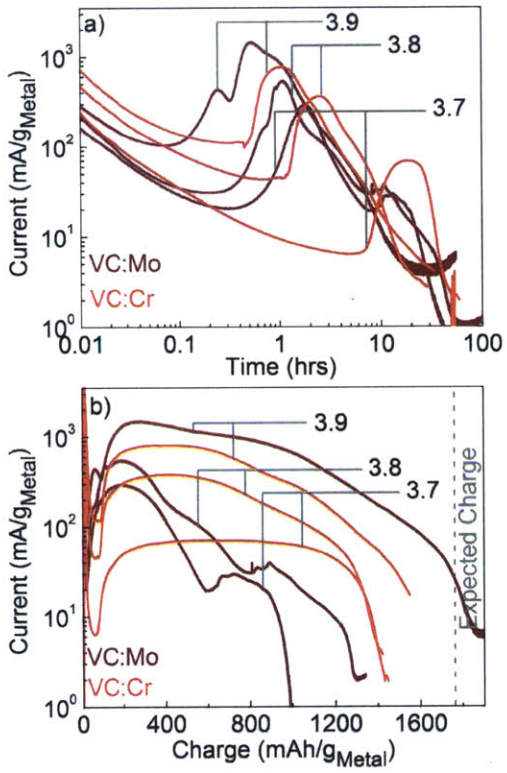

Figure 3-4. Potential dependent Li_2O_2 oxidation activity of carbon-containing VC:Cr,Mo:Li_2O_2:LiNafion = 1:0.667:1:1 electrodes compared at 3.7, 3.8, and 3.9 V_{Li}. (a) Current profile vs. time; (b) Current profile vs. charge.

To examine the intrinsic activities across all the promoters studied, area-specific activities (normalized to the BET surface area of the promoter) in carbon-containing

electrodes are shown in Figure 3-6a for bulk metal nanoparticles and Figure 3-6b for metal oxides. The following trend can be resolved: Mo > Cr ≈ Ru > MoO_3 ≈ RuO_2 ≈ Cr_2O_3 > Co ≈ Co_3O_4 ≈ α-MnO_2 > Mn.

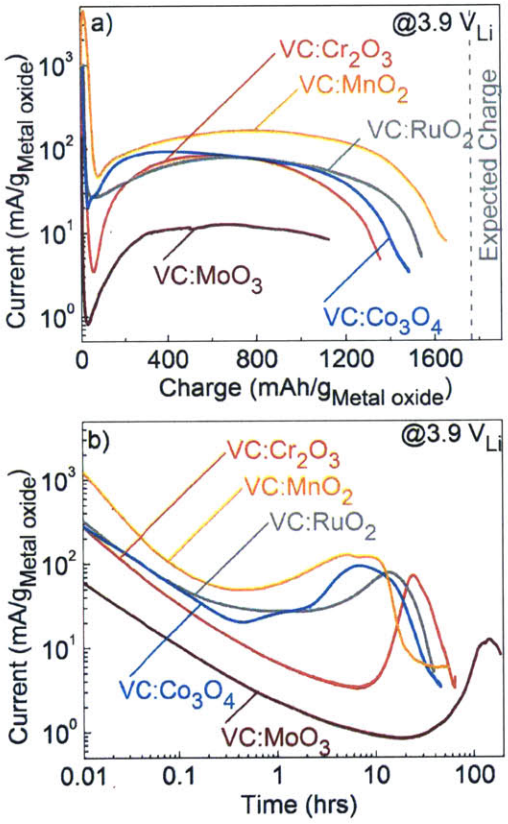

Figure 3-5. Electrochemical performance of metal oxide nanoparticles in carbon-containing VC:promoter:Li_2O_2:LiNafion = 1:0.667:1:1 (mass ratios) electrodes at 3.9 V_{Li}. (a) Current per mass of promoter *vs.* capacity. (b) Current per mass of promoter *vs.* time.

Of particular interest is the fact that bulk transition metal nanoparticles consistently have higher specific activities and shorter activation time than their corresponding oxides, particularly for highly active transition metals: Mo > MoO_3, Cr > Cr_2O_3 and Ru > RuO_2. The reduction in activity from metal to oxide cannot be explained fully by decreased

electrical conductivity of oxides in the carbon network, especially considering that Ru and RuO_2 have resistivity of ~8 $\mu\Omega\cdot cm$[117] and ~40 $\mu\Omega\cdot cm$[118] respectively, both being relatively conductive. Here we hypothesize that the observed activity trend is related to the relative surface reactivity of the promoter with Li_2O_2 towards an intermediate product as investigated through XAS below. We later detail a mechanism for the observed promotion of the Li_2O_2 oxidation reaction, which goes beyond the work initiated previously by our group[78] and Black *et al.*[41]

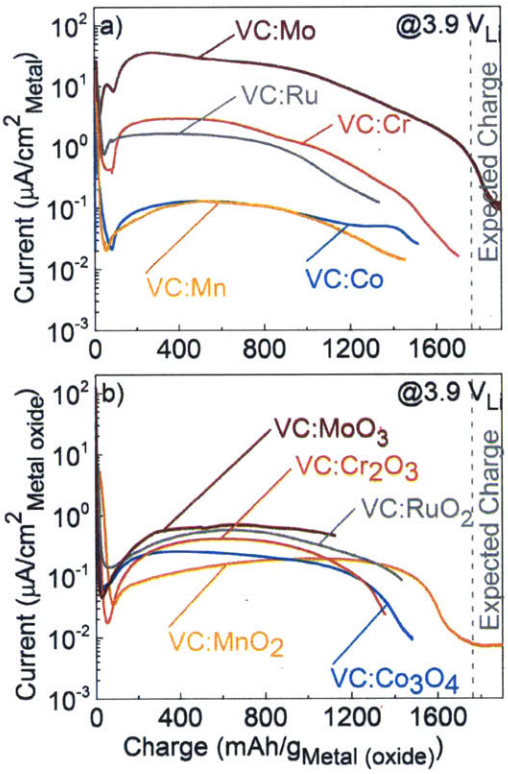

Figure 3-6. Electrochemical performance of carbon-containing VC: promoter:Li_2O_2:LiNafion = 1:0.667:1:1 (mass ratios) electrodes at 3.9 V_{Li}. (a) Current per promoter BET surface area *vs.* capacity for metal nanoparticles promoted electrodes. (b) Current per promoter BET surface area *vs.* capacity for metal oxide nanoparticles promoted electrodes. Separation of (a) and (b) is for clarity purposes.

3.3.2. Chemical evolution of promoter surface in preloaded Li_2O_2 electrodes during electrochemical oxidation

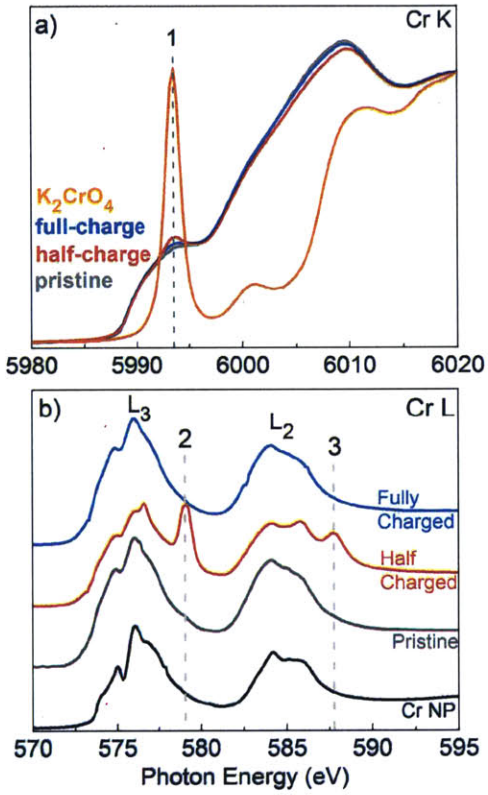

Figure 3-7. Experimental evidence of Cr^{6+} in tetrahedral environment using Cr K and L edge XAS in carbon-free Cr-promoted electrodes charged at 3.8 V_{Li}. (a) Cr K edge spectra of carbon-free pristine, half-charged and fully charged Cr:Li_2O_2 electrodes with reference K_2CrO_4. (b) Cr L edge spectra of Cr nanoparticles, pristine, half-charged, and fully charged electrodes in the surface sensitive total electron yield (TEY) mode.

Here we discuss considerable changes in the oxidation state of Cr and Mo particles during charging using XAS data. We probed the chemical changes in charged carbon-free Cr:Li_2O_2 electrodes at 3.8 V_{Li} using XANES spectra of the Cr K edge, as shown in Figure 3-7a. XANES Cr K edge data from the pristine electrode to the partially and fully

charged electrodes in Figure 3-7a show that the peak labelled as (1) at 5993.5 eV grows in intensity, which matches well with that of reference K_2CrO_4, indicating the formation of a CrO_4^{2-} environment on the surface of Cr nanoparticles. The small intensity of peak (1) found in the charged electrodes suggests that the conversion to CrO_4^{2-} environment such as Li_2CrO_4 might be localized to the surface of Cr nanoparticles as XANES at the Cr K edge probes mainly the bulk of Cr nanoparticles. This hypothesis is further supported by Cr L edge data in Figure 3-7b. Not only does the Cr L edge spectra of Cr particles and pristine electrode reveal Cr_2O_3-like surfaces[78] (see Figure 2-17) but also the Cr L edge spectrum of an electrode charged at 3.8 V_{Li} shows strong conversion of Cr^{3+} to Cr^{6+} (peaks (2) and (3)), which is more visible than that shown previously at 3.9 V_{Li}.[78]

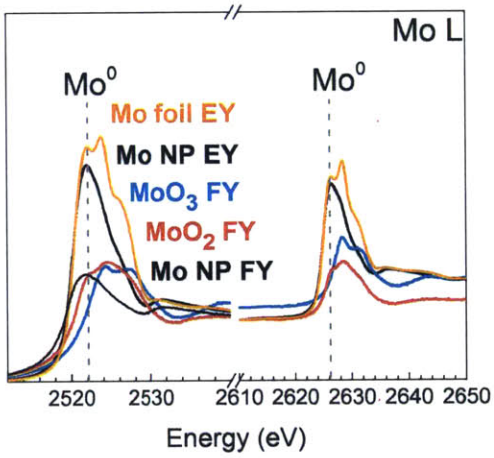

Figure 3-8. Mo L edge spectra of Mo nanopowder compared with those collected from reference MoO_3, MoO_2 and Mo foil, which indicate that the oxide layer on Mo powder is relatively thin. This thin Mo layer likely allowed access to the bulk Mo metal for the formation of XRD detectable Li_2MoO_4 as shown below in Figure 3-10.

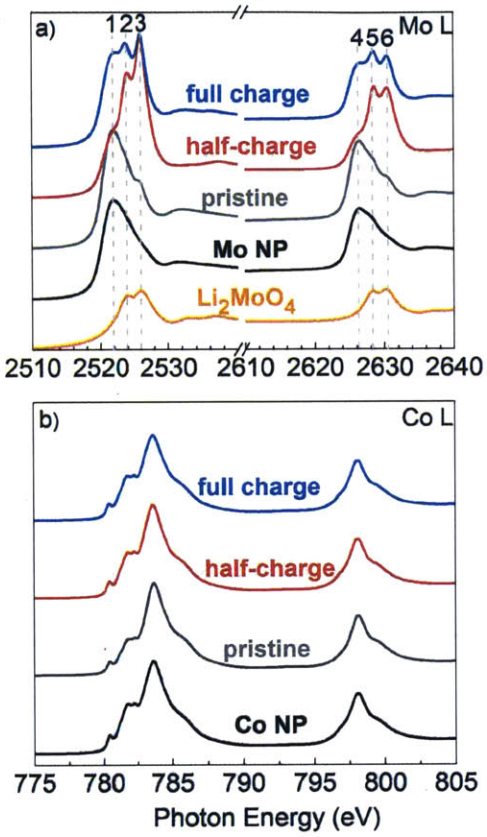

Figure 3-9. Surface sensitive transition metal L edge TEY spectra of Mo:Li_2O_2 and Co:Li_2O_2 for the metal nanopowder, pristine, half-charged, and fully charged electrodes at 3.9 V_{Li}. (a) Mo L edge spectra of Mo nanopowder, pristine, half-charged, and fully charged electrodes along with a reference spectrum of Li_2MoO_4. Note that due to incomplete charging of carbon-free Mo electrodes, partial charging was defined at 300 $mAh \cdot g^{-1}_{Mo}$. The fully charged Mo electrode terminated at ~600 $mAh \cdot g^{-1}_{Mo}$, which may explain the persistence of oxidized Mo in the electrode labelled "fully charged". (b) Co L edge spectra of Mo nanopowder, pristine, half-charged, and fully charged electrodes.

Comparing the Mo L edge spectra of MoO_2 and MoO_3 and a Mo foil, a significant fraction of Mo on the surface of Mo powder can be assigned to metallic Mo in addition to some with oxidation states of Mo^{4+} and Mo^{6+} (Figure 3-8). Considering a signal depth of ~75 Å (estimated as three times the electron mean free path)[119, 120] during L edge probing of Mo, the oxide shell on Mo nanoparticles here appears less than ~75 Å thick (or covers the surface incompletely), which likely allowed chemical conversion of the underlying Mo metal as shown by XRD. Comparing XAS data of the pristine carbon-free Mo:Li_2O_2 electrode with those of Mo powder, two new peaks labelled (3) and (6) in Figure 3-9a at higher photon energies of 2526.0 and 2630.4 eV appear, which signals an increased oxidation of the Mo surface in contact with Li_2O_2. The two new peaks match a reference Li_2MoO_4 in Figure 3-9a.

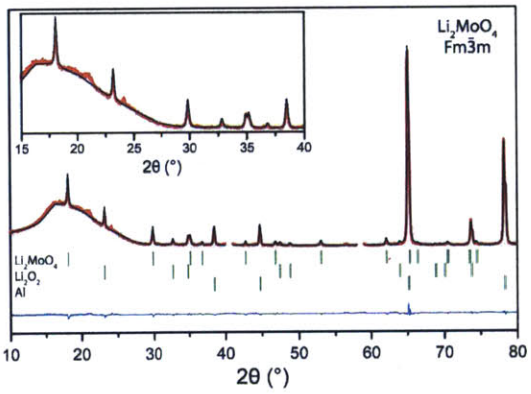

Figure 3-10. XRD of pristine Mo:Li_2O_2 (0.667:1) electrode. Clear evidence of Li_2MoO_4 is observed prior to electrochemical treatment which attests of the strong chemical conversion of Mo with Li_2O_2.

The spontaneous chemical reaction of Mo with Li_2O_2 was confirmed by the presence of Li_2MoO_4 XRD (Figure 3-10). After half and 'full' charge, the Mo L edge spectra

shows obvious growth of these peaks in Figure 3-9a (L_3: 2523.9 (2) and 2526 eV (3); L_2: 2628.6 (5) and 2630.4 eV (6)) compared to the Mo powder and pristine electrode, which indicates further oxidation of Mo. These new peaks can be matched to tetrahedrally coordinated Mo^{6+} in reference compound Li_2MoO_4 as shown by peaks (2), (3), (5), and (6). Ratios of peaks (1) through (6) in the fully charged compared to the half charged Mo electrodes shows signs of shift back to lower oxidation states of Mo which indicates a potential reversal as seen with Cr. Incomplete reversal of Mo^{6+} back to lower oxidation state is likely as a result of incomplete charging in Al:Mo electrodes seen in Figure 3-2c.

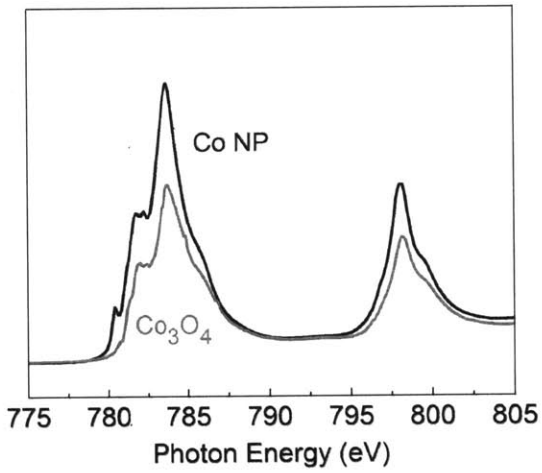

Figure 3-11. Co L edge TEY spectra of Co nanoparticles compared to Co_3O_4 shows that the surfaces of Co nanoparticles are mostly oxidized to a Co_3O_4 layer.

Analysis of the L edge spectra of the promoter powder, pristine, half-charged and fully charged electrodes for Co nanoparticles (Figure 3-9b) shows no resolved changes in the oxidation state of Co. Comparing the XAS spectra of Co and Co_3O_4 powder in Figure 3-11, the surfaces of Co nanoparticles are identified as Co_3O_4-like. Similar XAS probing

of α-MnO_2 (Figure 3-12a) and Co_3O_4-promoted (Figure 3-12b) electrodes shows no visible changes in oxidation state of Co or Mn during charge.

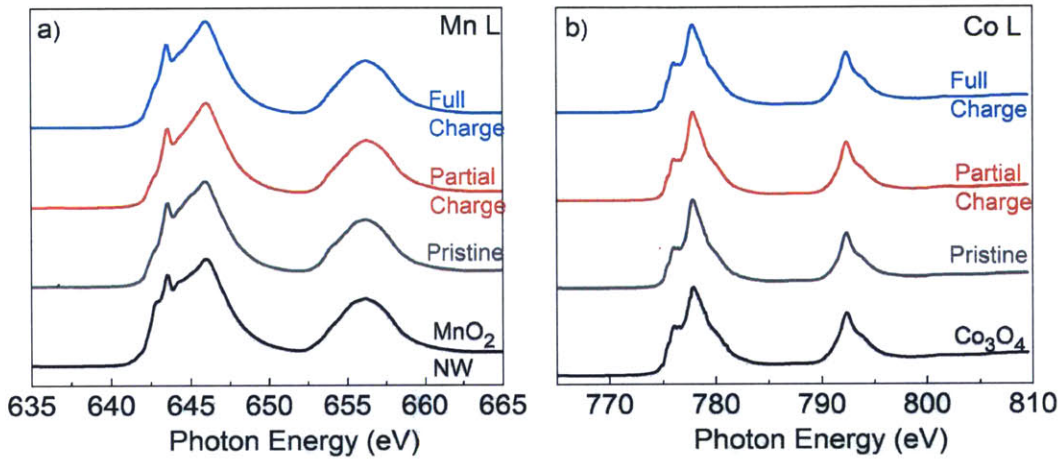

Figure 3-12. Metal L edge spectra of oxides MnO_2 and Co_3O_4 nanoparticles, pristine, half-charged, and fully charged carbon-free electrodes in the surface sensitive total electron yield (TEY) mode. Half and full charging for the electrodes examined here was performed at 3.9 V_{Li}.

Unfortunately, no L edge spectra could be reported for Ru electrodes at the time of this report. However, Figure 3-13 focuses on the surface microscopy of Ru nanoparticles in their pristine state and after mixing with Li_2O_2 using transmission electron microscopy (TEM). In Figure 3-13a, a Ru particle is observed with clear crystalline lattice fringes ending on a relatively clean surface. Comparing the pristine particle in Figure 3-13a to the Ru particle exposed to Li_2O_2 in Figure 3-13b, a distinct halo of a new phase is observed as highlighted in red. Chemical transformation appear to have occurred on the Ru surface and for reason that will be discussed further below, we assign this new surface phase to Li_2RuO_3. It is interesting to observe that prominent changes in Mo and Cr, and Ru during Li_2O_2 oxidation coincide with greater activity compared to the apparently

stable Co, Co_3O_4 and α-MnO_2. As the changes in oxidation observed during Li_2O_2 oxidation could result in metal dissolution into the electrolyte, the presence of transition metal in the electrolyte after charging was investigated in carbon-free electrodes using ICP-AES.

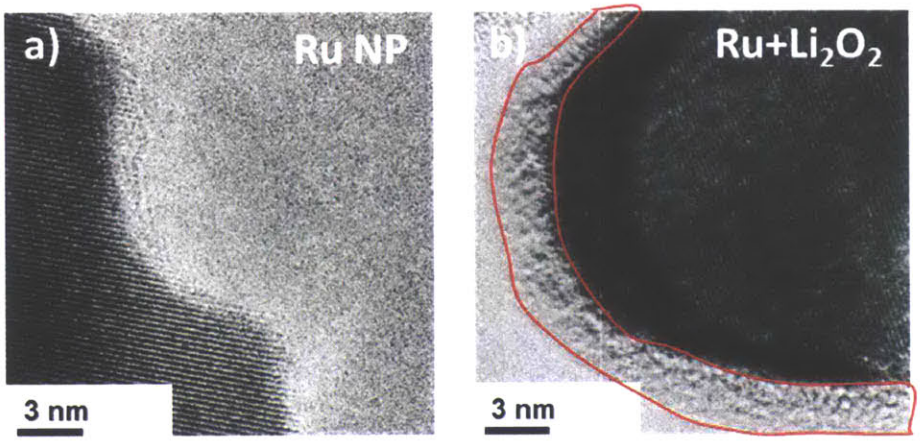

Figure 3-13. Transmission electron microscopy of the Ru particles before (a) and after (b) mixing with Li_2O_2. The region outlined in red represents a new material phase on the surface of the Ru nanoparticles after exposure to Li_2O_2.

3.3.3. III. Promoter dissolution during Li_2O_2 oxidation and implication on the Li_2O_2 oxidation kinetics

Table 3-1 summarizes the results of probing the presence of soluble metal species in the electrolyte post-charging. The molar amount of soluble metal in the electrolyte generally increases with greater activation of Li_2O_2 oxidation and XAS-resolved oxidation state changes in the promoter: Mo > Cr > Co ≈ Co_3O_4 > α-MnO_2. It is conceivable that dissolved promoter-derived complexes in the electrolyte are acting as redox mediators to the electrochemical oxidation of Li_2O_2. However, the measured

concentrations of dissolved species are one order of magnitude lower compared to the typical concentrations of more than 10 mM of redox mediators used in the literature.[61, 110]

Table 3-1. Summary of ICP-AES investigation post-charging of carbon-free promoter:Li_2O_2 = 0.667:1 electrodes

Promoter	**Mo**	**Cr**	**Co**	**Co_3O_4**	**α-MnO_2**
ppm in 10 mL solution	0.58	0.4	0	0	0.1
Conc. in 100 μL (mM)	0.61	0.77	0	0	0.18

To examine the influence of these soluble species on the observed enhancement of Li_2O_2 oxidation with Cr, Mo and Ru, we devised an experiment, wherein a promoted high activity electrode (Mo, Cr, and Ru) was allowed to fully charge at 3.9 V_{Li} in 0.1 M $LiClO_4$/DME electrolyte (see experimental section), likely resulting in dissolved transition metal species in the electrolyte. Immediately afterwards, a carbon electrode (VC:Li_2O_2 = 1:1, without promoter) was substituted into the cell (reusing the exact previous electrolyte layer containing the dissolved metal species) and similarly charged at 3.9 V_{Li}. The absence of electrochemical activation in all three non-promoted VC:Li_2O_2 electrodes in Figure 3-14a, b, c suggests that the leached metal species in the electrolyte are not responsible for the enhanced kinetics of Li_2O_2 with Cr, Mo, and Ru.

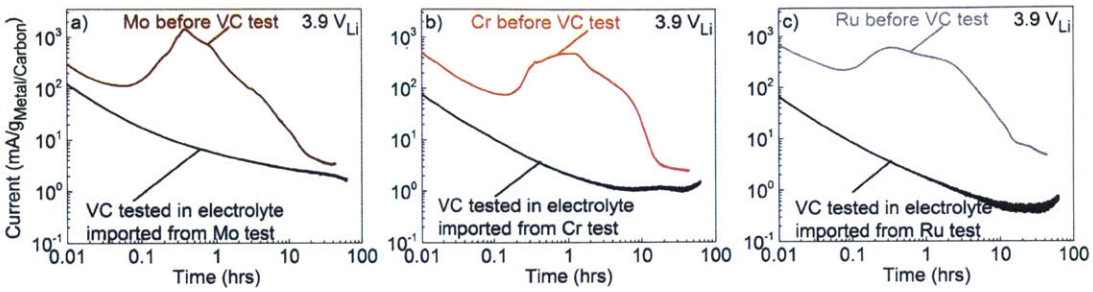

Figure 3-14. Effect of impurities (transition metal species dissolved in the electrolyte, water, and other in operando impurities) during Li_2O_2 oxidation in (a) Mo-promoted electrodes, (b) Cr-promoted electrodes, and (c) Ru-promoted electrodes tested by substituting a VC-promoted (VC:Li_2O_2:LiNafion = 1:1:1) electrode into the cell immediately after full charge of a VC: promoter:Li_2O_2:LiNafion = 1:0.667:1:1. ICP-AES data revealed that dissolved metal cations from the preceding promoted electrodes charged at 3.9 V_{Li} were present. The inactivity of the VC-only electrode thus tested suggests that the dissolved cations are not the source of activity in promoted electrodes.

3.3.4. Influence of water on the Li_2O_2 oxidation kinetics

Meini et al.[121] demonstrate that impurities such as water (produced from electrolyte degradation in operando) can enhance the electrode activation. Similarly to observations made for the leached metal species, the absence of electrochemical activation in all three VC:Li_2O_2 electrodes in Figure 3-14a, b, c suggests that water potentially produced in operando is not the origin of the enhanced kinetics of Li_2O_2 oxidation with Cr, Mo, and Ru. We separately investigate the influence of increased water content (baseline 20 ppm, 100 ppm, and 5000 ppm) on the activation of a promoter-free VC:Li_2O_2 as well as the least active VC:Mn:Li_2O_2 at 3.9 V_{Li} (Figure 3-15a, b). An earlier dip-then-rise in current

(~8 hours) is observed in VC:Li_2O_2 electrodes which might indicate electrode activation from less than 100 ppm to 5000 ppm in agreement with the work of Mieni et al.[121] However, no reduction in activation time was observed in the case of VC:Mn:Li_2O_2 electrodes. In agreement with Mieni et al.,[121] the overall activity (average current at the applied voltage of 3.9 V_{Li}, < 20 $mA \cdot g^{-1}_{promoter}$) was not greatly enhanced at higher water contents in both types of electrodes tested. In the case of Mn-promoted electrodes, addition of water appears detrimental to activity (Figure 3-15b). Overall, in operando increase in water-content and other impurities cannot explain the two order of magnitude enhancement in electrode performance using nanoparticles such as Mo, Cr, and Ru. Below, we discuss a unifying descriptor for the solid-state activation of the Li_2O_2 oxidation reaction.

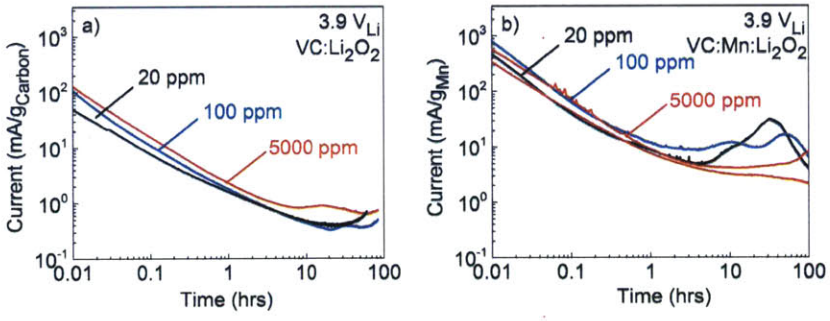

Figure 3-15. Effect of electrolyte water (baseline 20 ppm, 100 ppm, and 5000 ppm) content on the activation of Li_2O_2 oxidation in (a) VC-promoted (VC:Li_2O_2:LiNafion = 1:1:1) and (b) the least active Mn-promoted (VC:Mn:Li_2O_2:LiNafion = 1:0.667:1:1).

Table 3-2. List of potential reactions of the type $Li_2O_2 + M_aO_b \pm O_2 \rightarrow Li_xM_yO_z$ and associated enthalpy of reaction using the materials project database.[122] Reactions with highest enthalpies are highlighted in blue.

Reaction Number	Catalyst	Reaction	Enthalpy of reaction per mole of Catalyst (kJ/mol)
1	MnO_2	$Li_2O_2 + MnO_2 \leftrightharpoons 1/2\ O_2 + Li_2MnO_3$	-104.5
2		$Li_2O_2 + 2/3MnO_2 \rightleftharpoons 1/3O_2 + 2/3Li_3MnO_4$	-56.5
3		$Li_2O_2 + 4MnO_2 \leftrightharpoons O_2 + 2LiMn_2O_4$	-13.5
4	Mn_3O_4	$Li_2O_2 + 1/3Mn_3O_4 \leftrightharpoons 1/6\ O_2 + Li_2MnO_3$	-492
5		$Li_2O_2 + 2/9Mn_3O_4 \rightleftharpoons 1/9O_2 + 2/3Li_3MnO_4$	-349
6		$Li_2O_2 + 4/3Mn_3O_4 + 1/3O_2 \rightleftharpoons 2Li_3MnO_4$	-218
7	Co_3O_4	$Li_2O_2 + 2/3Co_3O_4 \leftrightharpoons 1/3O_2 + 2LiCoO_2$	-151
8	Cr_2O_3	$Li_2O_2 + Cr_2O_3 + O_2 \leftrightharpoons Li_2Cr_2O_7$	-247
9		$Li_2O_2 + 3Cr_2O_3 + 5/2O_2 \leftrightharpoons 2LiCr_3O_8$	-137.17
10		$Li_2O_2 + Cr_2O_3 \leftrightharpoons 1/2O_2 + 2LiCrO_2$	-82
11		$Li_2O_2 + 1/2Cr_2O_3 + 1/4O_2 \leftrightharpoons Li_2CrO_4$	-440
12		$Li_2O_2 + 1/3Cr_2O_3 \leftrightharpoons 1/6O_2 + 2/3Li_3CrO_4$	-338
13		$Li_2O_2 + Cr_2O_3 + O_2 \leftrightharpoons Li_2Cr_2O_7$	-247
14	Mo	$Li_2O_2 + Mo + O_2 \leftrightharpoons Li_2MoO_4$	-939
15		$Li_2O_2 + 1/2Mo + 1/4O_2 \leftrightharpoons 1/2Li_4MoO_5$	-952
16		$Li_2O_2 + 2/3Mo + 1/6O_2 \leftrightharpoons 1/3Li_6Mo_2O_7$	-603.75
17		$Li_2O_2 + Mo + 1/2O_2 \leftrightharpoons Li_2MoO_3$	-645
18		$Li_2O_2 + 2Mo + O_2 \leftrightharpoons 2LiMoO_2$	-473.5
19		$Li_2O_2 + 3/2Mo + O_2 \leftrightharpoons 1/2Li_4Mo_3O_8$	-609
20		$Li_2O_2 + 5/2Mo + 13/4O_2 \leftrightharpoons Li_4Mo_5O_{17}$	-837.3
21	MoO_3	$Li_2O_2 + MoO_3 \leftrightharpoons Li_2MoO_4 + 1/2O_2$	-158
22	Ru	$Li_2O_2 + Ru + 1/2O_2 \leftrightharpoons Li_2RuO_3$	-446
23		$Li_2O_2 + 2/7Ru \leftrightharpoons 1/7O_2 + 2/7Li_7RuO_6$	-463.5
24		$Li_2O_2 + 2Ru + O_2 \leftrightharpoons 2LiRuO_2$	-290.5
25	RuO_2	$Li_2O_2 + RuO_2 \rightleftharpoons 1/2O_2 + Li_2RuO_3$	-19.5
26		$Li_2O_2 + 2/7RuO_2 \rightleftharpoons 3/7O_2 + 2/7Li_7RuO_6$	-37

3.3.5. Unified mechanism of solid-state activation of Li_2O_2 oxidation

Further insights into the enhanced Li_2O_2 kinetics is gained from examining the enthalpies for conversion reactions: $Li_2O_2 + M_aO_b \pm O_2 \rightarrow Li_xM_yO_z$, where M_aO_b is the surface composition of the promoter. Values of computed enthalpies for a number of representative reactions are tabulated in Table 3-2.[122] Based on the L edge XAS results of pristine Cr, Mo, and Co particles, their surfaces were identified as Cr_2O_3, Mo/MoO_x, and Co_3O_4, respectively. It is assumed that the surface of Mn particles was covered by Mn_3O_4 as reported by American Elements and that of Ru by Ru/RuO_2 based on previous studies.[123] In the case of the metal oxides, the surfaces of MoO_3, Cr_2O_3, Co_3O_4, α-MnO_2 and RuO_2 are comparable to the bulk. Additionally, the reaction intermediates of Cr and Mo are Li_2CrO_4 and Li_2MoO_4, respectively, as revealed from XAS measurements. Increasing enthalpy for chemical reaction between Li_2O_2 and the promoter was correlated with increasing specific Li_2O_2 oxidation currents in both carbon free and carbon-containing electrodes, as shown in Figure 3-16. This trend shows that the generally reduced activities from metals to metal oxides (Figure 3-6) is related to the relative thermochemical stability of metal oxides in presence of Li_2O_2 which results in reduced conversion. A notable exception in the correlation of enthalpy with activity in Figure 3-16 arises with Mn nanoparticles (with Mn_3O_4 surfaces) which a priori would be expected to have activity on the order of Cr and Ru promoter. Using Au nanoparticles enhanced Raman spectroscopy, spontaneous conversion of the promoter to Li_2MnO_3 is observed in pristine $Mn:Li_2O_2$ electrodes (Figure 3-17) in agreement with a relatively large expected conversion enthalpy of reaction 4 in Table 3-2.

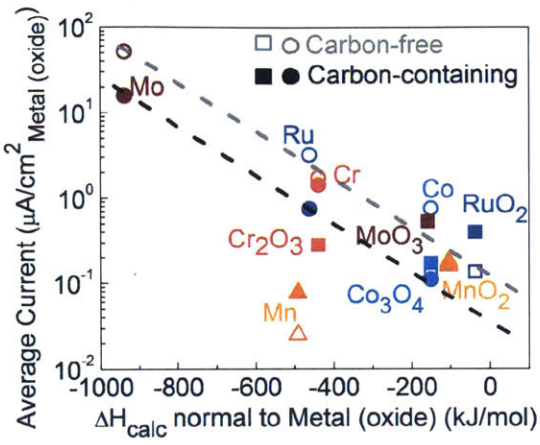

Figure 3-16. Average BET surface area specific activity at 3.9 V_{Li} for carbon-free (open symbol) and carbon-containing (filled symbols) versus calculated enthalpies of chemical conversion $Li_2O_2 + M_aO_b \pm O_2 \rightarrow Li_xM_yO_z$ highlighted in Table S1 (Ceder *et al.*[122]). (Circles): Metal nanoparticles, (Squares): Metal oxides. Triangle markers are used for the case of Mn-based catalysts as discussed in the text. Dotted lines are provided as a guide and should not be interpreted as linear fits.

Under these observations, the pathway of electrode activation during Li_2O_2 oxidation is identified as cyclical chemical conversion of the promoter to a corresponding lithiated metal oxide $Li_xM_yO_z$ followed by electrochemical delithiation with generally better kinetics compared to the direct oxidation of $Li_2O_2 \rightarrow 2Li^+ + 2e^- + O_2$ (Figure 3-18a). In the particular case of Mn, activity is limited by the delithation step, which would not be possible at the 3.9 V_{Li} applied potential in our study. Contrary to the other promoters investigated for which the $Li_xM_yO_z$ intermediates have reversible delithiation potentials below the 3.9 V_{Li} applied potential (Table 3-3), the delithiation potential of Li_2MnO_3 is reported above 4.5 V_{Li},[124, 125] well above the applied chronoamperometry potential.

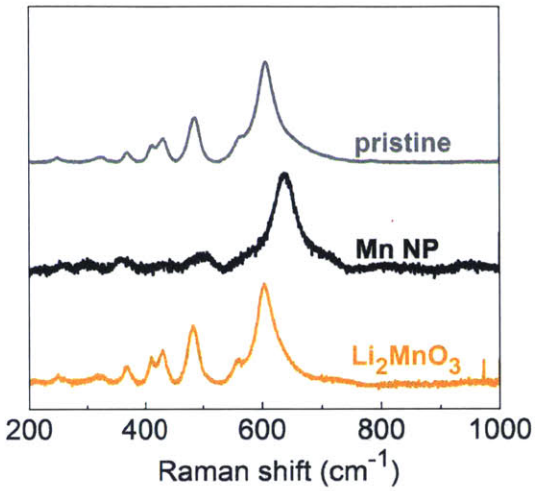

Figure 3-17. Raman spectroscopy of pristine carbon-free Mn:Li_2O_2 electrode, Mn nanopowder, and Li_2MnO_3 reference powder. Gold nanoparticles enhanced raman was used in Mn:Li_2O_2 probing.

Our proposed pathway can be used to explain the surface behavior during Li_2O_2 oxidation of the reported TiC[21] and Ti_4O_7[126] promoters. X-ray photoelectron spectra (XPS) after first discharge on TiC and Ti_4O_7 in Li-O_2 batteries[21] reveal the growth of peaks at ~458.5 and ~464 eV, indicative of Ti^{4+} $2p_{3/2}$ and Ti^{4+} $2p_{1/2}$ in Li_2TiO_3.[127] The thermodynamically spontaneous reactions between Li_2O_2 and TiC and Ti_4O_7 in presence of oxygen such as $Li_2O_2 + TiC + 3/2O_2 \rightarrow Li_2TiO_3 + CO_2$ (ΔH_{calc} = -1459 kJ/mol[122]), $Li_2O_2 + TiC + O_2 \rightarrow Li_2TiO_3 + CO$ (ΔH_{calc} = -1071 kJ/mol[122]) and $4Li_2O_2 + Ti_4O_7 \rightarrow 4Li_2TiO_3 + 3/2O_2$ (ΔH_{calc} = -753 kJ/mol[122]) have large thermodynamically favorable enthalpies. Regarding delithiation of the intermediate, Li_2TiO_3 is stable against delithiation above 4.7 V_{Li}[127] which would explain the relatively low surface-area-normalized activity of Ti_4O_7[126] (~4V at ~$8.4 \cdot 10^{-3}$ $\mu A \cdot cm^{-2}_{BET}$) electrodes loaded with crystalline Li_2O_2 and the persistence of the Ti^{4+} XPS peak during cycling beyond the first discharge.[21, 126]

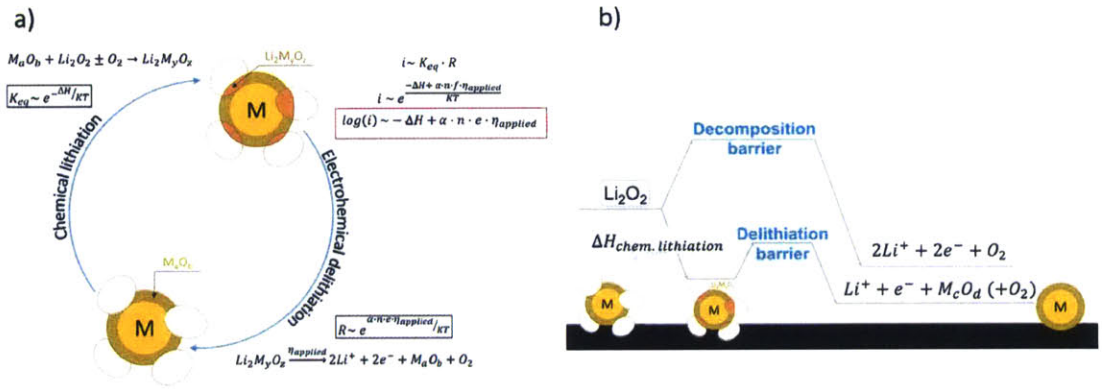

Figure 3-18. Diagram of reaction steps in proposed mechanism of chemical conversion of chemical conversion of Li_2O_2 and catalyst to $Li_xM_yO_z$ followed by delithiation. Below the diagram a derivation of current dependence on enthalpy and effective applied overpotential is provided.

3.3.6. Microkinetics analysis of proposed mechanism of Li_2O_2 oxidation

Chemical lithiation step

$$Li_2O_2 + \alpha\ M_aO_b + \beta\ _2 \leftrightarrow Li_2M_yO_z\ \ (z = 3,4) \tag{3.1}$$

Electrochemical step

$$Li_2M_yO_z\ \leftrightarrow xLi^+ + xe^- + Li_{2-x}M_yO_z \tag{3.2}$$

The state of delithiation of $Li_2M_yO_z$, x, is a function of the relative rates of reactions (3.1) and (3.2).

Kinetics analysis of electrochemical reaction (3.2)

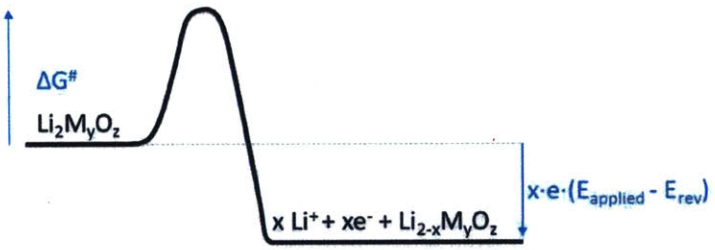

Figure 3-19. Energy landscape diagram during electrochemical delithiation reaction (3.2) of the lithiated metal oxide ($Li_2M_yO_z$)

$$R_{ne} = R_{forward} - R_{backward}$$

$$R_{net} = k_f \cdot [Li_2M_yO_z] - k_b \cdot a_{Li^+}^{x} \cdot [Li_{2-x}M_yO_z]$$

Where a_{Li+} is the activity of lithium cations on the surface of the promoter nanoparticle (within the lithiated metal oxide layer).

The rate constants k_f and k_b are potential dependent and can be shown from diagram (Figure 3-19):

$$k_f = k^0 \cdot \exp\left(\frac{(1-\alpha)\cdot x\cdot F}{RT}(E - E^0)\right)$$

$$k_b = k^0 \cdot \exp\left(\frac{-\alpha\cdot x\cdot F}{RT}(E - E^0)\right)$$

Where E^0 is the standard potential of the lithiated metal oxide $Li_2M_yO_z$ and k^0 is the standard rate constant of reaction (3.2), E is the applied potential (3.9 V_{Li} in most of our studies).

It follows then, that

$$R_{net} = k^0 \cdot \exp\left(\frac{(1-\alpha)\cdot x\cdot F}{RT}(E - E^0)\right) \cdot [Li_2M_yO_z] - k^0 \cdot \exp\left(\frac{-\alpha\cdot x\cdot F}{RT}(E - E^0)\right) \cdot a_{Li^+}^{x} \cdot [Li_{2-x}M_yO_z]$$

The concentration of partially delithiated $Li_{2-x}M_yO_z$ can be safely assumed to be proportional to the concentration of $Li_2M_yO_z$ through a function of the state of delithiation x. Therefore, we write without loss of generality:

$$[Li_{2-x}M_yO_z] = \rho(x) \cdot [Li_2M_yO_z] \; with \; \rho(x) \; a \; function \; of \; x \; likely \; less \; than \; 1$$

Now:

$$R_{net} = k^0 \cdot [Li_2M_yO_z]\left\{\exp\left(\frac{(1-\alpha)\cdot x\cdot F}{RT}(E-E^0)\right) - \exp\left(\frac{-\alpha\cdot x\cdot F}{RT}(E-E^0)\right)\cdot a_{Li^+}^x \cdot \rho(x)\right\}$$

Then, current per unit area can be expressed as:

$$i = x \cdot F \cdot k^0 \cdot [Li_2M_yO_z]\left\{\exp\left(\frac{(1-\alpha)\cdot x\cdot F}{RT}(E-E^0)\right) - \exp\left(\frac{-\alpha\cdot x\cdot F}{RT}(E-E^0)\right)\cdot a_{Li^+}^x \cdot \rho(x)\right\} \quad (3.3)$$

Coupling reactions (3.1) and (3.2)

We incorporate an analysis of the coupled chemical step reaction (3.1).

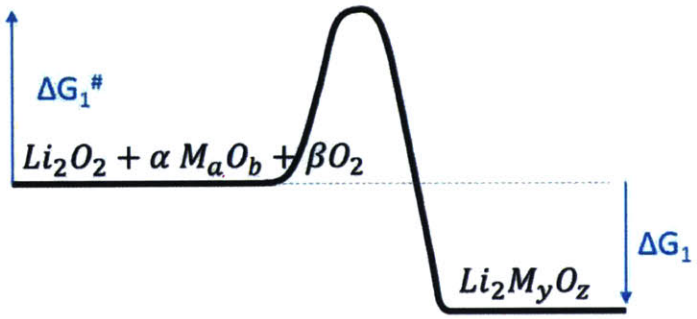

Figure 3-20. Energy landscape diagram during chemical lithiation reaction (3.1)

- Given their solid-state nature and large concentration we make the following simplifications:

$$a_{Li_2O_2} = a_{M_aO_b} = 1$$

- The activity of oxygen depends on the partial pressure of oxygen and can be written as:

$$a_{O_2} = p_{O_2}$$

Two assumptions can be made with regards to the concentrations of reactants and products in reaction (3.1):

Assumption 1: The generated lithiated metal oxide ($Li_2M_yO_z$) remains in equilibrium with the reactants Li_2O_2 and M_aO_b during the entirety of the oxidation process.

This assumption would result in the following equilibrium equality:

$$K_{eq} = \frac{[Li_2M_yO_z]}{a_{Li_2O_2} \cdot a_{M_aO_b}^{\alpha} \cdot a_{O_2}^{\beta}} = e^{-\frac{\Delta G_1}{RT}}$$

$$[Li_2M_yO_z] = K_{eq} p_{O_2}^{\beta} = e^{-\frac{\Delta G_1}{RT}} p_{O_2}^{\beta}$$

And

$$i = x \cdot F \cdot k^0 \cdot e^{-\frac{\Delta G_1}{RT}} \cdot p_{O_2}^{\beta} \cdot \left\{ \exp\left(\frac{(1-\alpha)\cdot x \cdot F}{RT}(E - E^0)\right) - \exp\left(\frac{-\alpha \cdot x \cdot F}{RT}(E - E^0)\right) \cdot a_{Li^+}^{x} \cdot \rho(x) \right\} \tag{3.4}$$

Assumption 2: Reaction (3.1) is driven away from equilibrium by the electrochemical step. A steady-state condition is reached such that the concentration of $Li_2M_yO_z$ on the surface of the surface of the nanoparticle remains constant throughout oxidation.

Under this assumption 2:

$$\frac{d}{dt}[Li_2M_yO_z] = 0 = k_1^f \cdot p_{O_2}^{\beta} - k_1^b \cdot [Li_2M_yO_z] - \left[k_f \cdot [Li_2M_yO_z] - k_b \cdot a_{Li^+}^{x} \cdot [Li_{2-x}M_yO_z]\right]$$

$$0 = k_1^f \cdot p_{O_2}^{\beta} - k_1^b \cdot [Li_2M_yO_z] - R_{net}$$

$$k_1^f \cdot p_{O_2}^{\beta} - k_1^b \cdot [Li_2M_yO_z] = R_{net}$$

Furthermore we can express using the energy diagram (Figure 3-20):

$$k_1^f = k_1 e^{-\frac{\Delta G_1^{\#}}{RT}}$$

$$k_1^b = k_1 e^{-\frac{\Delta G_1^{\#} - \Delta G_1}{RT}} = k_1 e^{-\frac{\Delta G_1^{\#}}{RT}} e^{\frac{\Delta G_1}{RT}}$$

$$k_1 e^{-\frac{\Delta G_1^{\#}}{RT}} \cdot p_{O_2}^{\beta} - k_1 e^{-\frac{\Delta G_1^{\#}}{RT}} e^{\frac{\Delta G_1}{RT}} \cdot [Li_2M_yO_z] = R_{net}$$

$$k_1 e^{-\frac{\Delta G_1^{\#}}{RT}} \cdot p_{O_2}^{\beta} - k_1 e^{-\frac{\Delta G_1^{\#}}{RT}} e^{\frac{\Delta G_1}{RT}} \cdot [Li_2M_yO_z] = k^0 \cdot [Li_2M_yO_z] \left\{ \exp\left(\frac{(1-\alpha)\cdot x \cdot F}{RT}(E - E^0)\right) - \right.$$

$$\left. \exp\left(\frac{-\alpha \cdot x \cdot F}{RT}(E - E^0)\right) \cdot a_{Li^+}^{x} \cdot \rho(x) \right\}$$

$$[Li_2M_yO_z] \cdot \left\{ k^0 \cdot \left\{ \exp\left(\frac{(1-\alpha)\cdot x \cdot F}{RT}(E - E^0)\right) - \exp\left(\frac{-\alpha \cdot x \cdot F}{RT}(E - E^0)\right) \cdot a_{Li^+}^{x} \cdot \rho(x) \right\} + \right.$$

$$\left. k_1 e^{-\frac{\Delta G_1^{\#}}{RT}} e^{\frac{\Delta G_1}{RT}} \right\} = k_1 e^{-\frac{\Delta G_1^{\#}}{RT}} \cdot p_{O_2}^{\beta}$$

$$[Li_2M_yO_z] = \frac{e^{-\frac{\Delta G_1^{\#}}{RT}} \cdot p_{O_2}^{\beta}}{\frac{k^0}{k_1} \left\{ \exp\left(\frac{(1-\alpha)\cdot x \cdot F}{RT}(E-E^0)\right) - \exp\left(\frac{-\alpha \cdot x \cdot F}{RT}(E-E^0)\right) \cdot a_{Li^+}^{x} \cdot \rho(x) \right\} + e^{-\frac{\Delta G_1^{\#}}{RT}} e^{\frac{\Delta G_1}{RT}}}$$

We can rewrite:

$$[Li_2M_yO_z]$$

$$= e^{-\frac{\Delta G_1}{RT}} \frac{e^{-\frac{\Delta G_1^{\#}}{RT}} \cdot p_{O_2}^{\beta}}{\frac{k^0}{k_1} \cdot \left\{ \exp\left(\frac{(1-\alpha)\cdot x \cdot F}{RT}(E - E^0)\right) - \exp\left(\frac{-\alpha \cdot x \cdot F}{RT}(E - E^0)\right) \cdot a_{Li^+}^{x} \cdot \rho(x) \right\} e^{-\frac{\Delta G_1}{RT}} + e^{-\frac{\Delta G_1^{\#}}{RT}}}$$

Now current is written as:

$$i = x \cdot F \cdot k^0 \cdot [Li_2M_yO_z] \left\{ \exp\left(\frac{(1-\alpha)\cdot x \cdot F}{RT}(E - E^0)\right) - \exp\left(\frac{-\alpha \cdot x \cdot F}{RT}(E - E^0)\right) \cdot a_{Li^+}^{x} \cdot \rho(x) \right\}$$

$$i = x \cdot F \cdot k^0 \cdot e^{-\frac{\Delta G_1}{RT}} \cdot p_{O_2}^{\beta} \frac{e^{-\frac{\Delta G_1^{\#}}{RT}} \cdot \left\{ \exp\left(\frac{(1-\alpha)\cdot x \cdot F}{RT}(E-E^0)\right) - \exp\left(\frac{-\alpha \cdot x \cdot F}{RT}(E-E^0)\right) \cdot a_{Li^+}^{x} \cdot \rho(x) \right\}}{\frac{k^0}{k_1} \left\{ \exp\left(\frac{(1-\alpha)\cdot x \cdot F}{RT}(E-E^0)\right) - \exp\left(\frac{-\alpha \cdot x \cdot F}{RT}(E-E^0)\right) \cdot a_{Li^+}^{x} \cdot \rho(x) \right\} e^{-\frac{\Delta G_1}{RT}} + e^{-\frac{\Delta G_1^{\#}}{RT}}} \quad (3.5)$$

Important note: for sufficiently large free energy of conversion in reaction (3.1), the preceding equation (3.5) collapses back to equation (3.4) which is equivalent to assuming that the reaction (3.1) is at equilibrium (assumption 1).

Under both assumptions 1 and 2, current is proportional to the exponential of the free energy of conversion ΔG_1 of reaction (3.1).

Under a sufficiently large effective overpotential: $\eta_{applied} = E_{applied} - E_{rev}^{Li_2M_yO_z} = E - E^0$

$$\exp\left(\frac{-\alpha \cdot x \cdot F}{RT}(E-E^0)\right) \cdot a_{Li^+}^{x} \cdot \rho(x) \ll \exp\left(\frac{(1-\alpha)\cdot x \cdot F}{RT}(E-E^0)\right)$$

$$i \approx x \cdot F \cdot k^0 \cdot e^{-\frac{\Delta G_1}{RT}} \cdot p_{O_2}^{\beta} \cdot \left\{ \exp\left(\frac{(1-\alpha)\cdot x \cdot F}{RT}(E-E^0)\right) \right\} \qquad (Tafel) \quad (3.6)$$

Or

$$log(i) \approx -\frac{\Delta G_1}{RT} + \frac{(1-\alpha)\cdot x \cdot F}{RT}(E-E^0) + ln(x \cdot F \cdot k^0 \cdot p_{O_2}^{\beta}) \quad (3.7)$$

We note that the above result in (3.6) is equivalent to a chemical step paired with a tafel step. Approximating the free energy of reaction (3.1) with enthalpies of the conversion reaction (3.1) as most reactants except oxygen are in the solid state (entropy contribution to the free energy will not be large):

$$log(i) \approx -\frac{\Delta H_1}{RT} + \frac{(1-\alpha)F}{RT}\left(E_{applied} - E_{rev}^{Li_2M_yO_z}\right) + ln(x \cdot F \cdot k^0 \cdot p_{O_2}^{\beta}) \quad (3.8)$$

Utilizing the above simplified equation, a correlation between the enthalpies of chemical conversion, reaction (3.1), and the logarithm of current is expected to first approximation as seen in (Figure 3-16) which validates the proposed mechanism.

Table 3-3. Estimated values of $\log(i) \sim -\Delta H + \alpha \cdot n \cdot e \cdot \eta_{applied}$ assuming $\alpha \approx 0.5$ and n is the number of Li^+ cations in the lithiated compound.

Catalysts	Intermediate Lithiated compound	$-\Delta H(kJ/mol)$	E_{rev} (V)	η at 3.9 V_{Li}	$\alpha \cdot n \cdot e \cdot \eta$ (eV)	$(-\Delta H + \alpha \cdot n \cdot e \cdot \eta)$
MnO_2	Li_2MnO_3	-104.5	4.6[124]	-0.7	-0.7	N/A ($\eta < 0$)
Mn, Mn_3O_4	Li_2MnO_3	-492	4.6	-0.7	-0.7	N/A ($\eta < 0$)
Cr,Cr_2O_3	Li_2CrO_4	-440	3.7[128]	0.2	0.2	4.78
Mo	Li_2MoO_4	-939	2.0[129]	1.9	1.9	11.66
Ru	Li_2RuO_3	-446	3.5[130, 131]	0.4	0.4	5.04
RuO_2	Li_2RuO_3	-37	3.5[130, 131]	0.4	0.4	0.78
Co, Co_3O_4	$LiCoO_2$	-151	3.8[132]	0.1	0.1	1.62

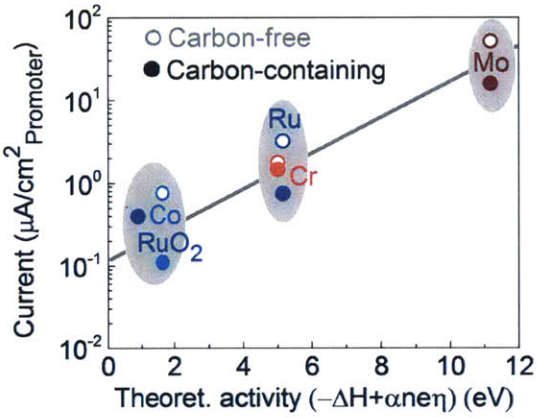

Figure 3-21. Agreement between theoretically estimated activity factor and measured electrode activity expressed as surface area normalized current.

Furthermore, estimates of $-\Delta H + \alpha \cdot n \cdot e \cdot \eta_{applied}$ are presented in Table 3-3. A good linear relation is found between this quantity and the experimentally measured activity trend (Figure 3-21) as expected from equation (3.8). It is worth noting that complete delithiation of Li_2CrO_4, Li_2MoO_4, Li_2RuO_3, and Li_2MnO_3 (above ~4.5 V_{Li}) would result in oxygen evolution $Li_xM_yO_z \rightarrow Li^+ + M_cO_d + O_2$ as desired in Li-O_2 batteries.[124, 125, 131]

On the other hand, the delithiation reaction will likely result in a metal oxide deposit but not necessarily the regeneration of the original promoter.

3.4. Conclusions

In this chapter, we report mechanistic insights into the kinetics of Li_2O_2 oxidation by coupling electrochemical Li_2O_2 oxidation trends of metal and oxide promoters with spectroscopic measurements and the reactivity energetics between Li_2O_2 and the promoter. The measured activities of Cr, Mo and Ru particles are an order of magnitude greater than those of Co and Mn as well as those of corresponding oxides. Upon Li_2O_2 oxidation, XAS measurements show that Cr and Mo particles become highly oxidized to M^{6+} in CrO_4^{2-} and MoO_4^{2-} environments such as Li_2CrO_4 and Li_2MoO_4, respectively, which is accompanied with soluble Cr and Mo-based species in the electrolyte. However, those soluble species as well as other potential impurities such as water generated in operando are not the main source for the order of magnitude enhancement in electrode activity in presence of Mo, Cr, and Ru for example. We present a strong correlation between increasing specific Li_2O_2 oxidation currents in both carbon free and carbon-containing electrodes and increasing enthalpy for chemical reaction between Li_2O_2 and the promoter. Our work proposes a universal mechanism for promoting Li_2O_2 oxidation kinetics via solid-state activation, which involves thermochemical conversion of the promoter surface and Li_2O_2 towards a lithium metal oxide, which can subsequently undergo electrochemical delithiation. A kinetic diagram depicting the chemical steps under which this mechanism leads to enhanced oxidation currents of Li_2O_2 is provided in Figure 3-18b The influence of such solid-state activation of Li_2O_2 oxidation for the voltage and faradaic efficiency of rechargeable Li-air batteries require further studies.

Chapter 4. Reversibility of O_2 reduction and evolution in presence of solid-state promoters for Li_2O_2 oxidation in Li-O_2 batteries

Adapted from manuscript draft in preparation. This work was done in collaboration with Jonathon R. Harding, Shuting Feng, Sayed Youssef Sayed, Fanny Bardé, and Yang Shao-Horn.

4.1. Introduction

In order to address the coupled issues of high overpotentials and poor round trip efficiencies, metal (oxides) nanoparticles referred to as catalysts in the Li-O_2 literature are commonly employed.[41, 78, 94, 99, 133] In Chapter 3, systematic probing of electrochemical and thermochemical trends aided by ex-situ X-ray absorption spectroscopy (XAS) revealed the chemical conversion of the promoter with the discharge product Li_2O_2 to form lithiated metal oxides ($Li_2O_2 + M_aO_b \pm O_2 \rightarrow Li_xM_yO_z$).[78, 133, 134] Later delithiation of the lithiated metal oxide intermediates is revealed to be the source of the observed enhanced kinetics of Li_2O_2 oxidation.[133] A mechanism which differs significantly from traditional oxygen evolution (OER) catalysis in which the catalyst lowers the barrier of the rate limiting step through tuned binding of oxygenated intermediates on the surfaces.[67, 69] Under this understanding, we refer to the metal nanoparticles additives as "promoters". Additionally, it is well known that severe degradation of the solvents is observed for most aprotic electrolytes including alkyl carbonates used in Li-Ion cells,[26] ethereal solvents[32, 135] and organosulfurs[136] in Li-O_2 cells. The electrolyte degradation couples with the formation of parasitic discharge products[23, 137] and the poor electronic conductivity[25, 40] of the main discharge product Li_2O_2 to cause high recharge overpotentials, low round trip efficiencies and limited cycle life. The chemical transformation of the promoter surface indicated in Chapter 3 likely has implications for the overall electrochemical to chemical dynamics within a Li-O_2 cell containing the various metal nanoparticle. Therefore, it becomes imperative to investigate the round trip utilization (during discharge) and release (during charge) of O_2 which need be symmetric for a truly rechargeable Li-O_2 cell. Reporting on the round trip chemical

efficacy of O_2 consumption and evolution in presence of promoters is therefore the focus of the present chapter.

McCloskey et al.[91] have used differential electrochemical mass spectrometry (DEMS) to investigate the OER during the charge reaction of Li-O_2 batteries using either polycarbonate:dimethoxyethane (PC:DME) or 1, 2 dimethoxyethane (DME) as electrolyte solvent. Their work concluded that metal nanoparticles in Li-O_2 cells only affected the removal of soluble parasitic products in PC-based electrolytes evolving CO_2 on charge, while no effect was observed in DME-based electrolytes where Li_2O_2 discharge product was oxidized to evolve O_2.[91] Later work by the same author[96] comparing the Li-O_2 and Na-O_2 systems further suggested that in the absence of carbonate side products, recharge of the alkali-O_2 cells should be efficient without needing promoter nanoparticles. These conclusions have not been consistent with the clear charging trends observed for Li_2O_2 decomposition using carbon-free electrodes preloaded with externally synthesized Li_2O_2 where little to no carbonates are expected.[133] In the work of Kundu et al.[134] exploring the effect of Mo_2C on charge, a charging plateau below 3.6 V_{Li} (strong enhancement effect) and online electrochemical mass spectrometry (OEMS) measurement of mostly O_2 with only trace CO_2 have been reported. The authors observed by X-ray photoelectron spectroscopy the conversion of the promoter surface to Li_xMoO_3[134] per our previously proposed mechanism.[133] Furthermore, comparison of the oxidation kinetics of Li_2O_2 in Li-O_2 cell and NaO_2 in Na-O_2[96] cell disregards the anticipated slower kinetics of a two-electron transfer vs. a one-electron transfer reaction as well as the possible differences in charge transport from one to the other.

In the present work, we investigate using DEMS the reversibility of O_2 consumption and evolution of Li-O_2 cells in presence of the Mo, Cr, and Ru which are the most active Li_2O_2 oxidation promoters previously reported[78, 133]. Explicitly, this investigation is centered on the O_2 evolution reaction (OER) from Li_2O_2 oxidation desired on charging of Li-O_2 batteries. On discharge, the desired discharge reaction in Li-O_2 batteries is the reaction of lithium with oxygen to form a lithium oxide (LiO_2, Li_2O_2, and/or Li_2O). Since the first publication by Kumar et al.,[138] the Li-O_2 electrochemical system, in absence of parasitic decomposition of the electrolyte or carbon cathode, has been reported to discharge through formation of Li_2O_2 as the final discharge product ($2Li^+ + 2e^- + O_2 \leftrightarrow Li_2O_2$).[32, 45] The stoichiometry of this reaction dictates the consumption of one O_2 molecule per two electrons passed (2 e^-/O_2). It is found that the above promoter nanoparticles do not alter the discharge pathway and abide by the 2 e^-/O_2 reaction. The most significant enhancement effect of the promoter nanoparticles has been observed on the Li_2O_2 oxidation reaction during cell charging.[78, 133] As described above, at 3.9 V_{Li} in presence of metal nanoparticles $Li_2O_2 + M_aO_b \pm O_2 \rightarrow Li_2M_yO_z$ occurs.[133] Therefore, we investigate the potential effect of this pathway on the regeneration of O_2 from $Li_2O_2 \leftrightarrow 2Li^+ + 2e^- + O_2$ and compare the actual reversibility of oxygen evolution across the high activity promoters Mo, Cr, and Ru identified previously.[133] Potentiostatic charging at 3.9 V_{Li} is selected to minimize electrolyte decomposition which has been shown to occur most strongly at potentials above 4.0 V_{Li}[23] and therefore allow simplified interpretation of O_2 evolution versus current. Charging is found to yield values of e^-/O_2 greater than 2 for all promoters and characteristic similarities between Cr and noble metal Ru and their difference from Mo are highlighted. Those similarities and differences are found

explicable by values of conversion enthalpies of the promoter with Li_2O_2 towards lithiated metal oxides upon charging.[133]

4.2. Experimental

4.2.1. Electrode preparation

The most active metal nanoparticles promoters discovered in our previous work,[133] namely Mo (US Research Nanomaterial Inc., purity = 99.9%, SSA_{BET} = 4 $m^2 \cdot g^{-1}$), Cr (US Research Nanomaterial Inc., 99.9%, 26 $m^2 \cdot g^{-1}$), and Ru (Sigma Aldrich, ≥ 98%, 23 $m^2 \cdot g^{-1}$) were selected for further study using DEMS. Vulcan XC72 (VC, Premetek, ~100 $m^2 \cdot g^{-1}$) carbon-supported electrodes containing these three promoter nanoparticles were fabricated in an argon-filled glovebox (MBraun, water content <0.1 ppm, O_2 content <1%). Fabrication tools consisting of a #50 mayer rod, battery grade aluminum foil (Targray Inc.), and Celgard C480 cell separator sheet (Celgard Inc.) were dried at 70 °C prior to use. Nanoparticles powders of VC, Mo, Cr, and Ru were dried at 100 °C under a 30 mbar vacuum in a Buchi® B585 oven. Transfer of the dried nanoparticles occurred with isolation from ambient air within the Buchi® vacuum tube.

Oxygen electrodes (O_2-electrodes) of VC:(Mo,Cr,Ru):LiNafion = 1:0.667:1 (mass ratios) were obtained by ink-casting on a sheet of Celgard C480. A mixture of 75 mg of Vulcan XC72, 50 mg of promoter, and 75 mg equivalent of IPA-dispersed lithium-substituted Nafion (LiNafion, Dupont) was homogenized in IPA by horn-sonication at 50% pulses of 30 W for 30 minutes. Similarly, Li_2O_2-preloaded electrodes of VC:(Mo,Cr,Ru):Li_2O_2:LiNafion = 1:0.667:1:1 (mass ratios) were obtained by ink-casting on a sheet of aluminum. A mixture of 75 mg of Vulcan XC72, 50 mg of promoter, 75 mg of Li_2O_2 (Alfa Aesar, ≥90%, ~345 nm after ball-milling), and 75 mg equivalent of IPA-

dispersed LiNafion was homogenized in IPA by horn-sonication at 50% pulses of 30 W for 30 minutes.

Within the anaerobic environment of the glovebox, half-inch diameter discs were punched and secured in the vacuum tube of the Buchi® oven tube and dried at 70 °C for a minimum of twelve hours before cell assembly.

4.2.2. DEMS experiments

Electrochemical cells using either O_2 electrodes or Li_2O_2-preloaded electrodes were fabricated in an argon glovebox (MBraun, water content <0.1 ppm, O_2 content <0.1 ppm), which were used for DEMS measurements. All cells included 150 μm lithium foil (RockWood Lithium Inc.), 0.1 M lithium bis(trifluoromethane)sulfonimide (LiTFSI) in diglyme (20 ppm nominal after drying on molecular sieves) and an O_2 or Li_2O_2-preloaded electrode. Cells consisting of lithium foil||2 Celgard C480 separators with 150 μL of 0.1 M LiTFSI in Diglyme||0.5 inch electrode were assembled in a custom cell with an internal volume of ca. 2.9 mL. An in-house DEMS based on a design reported by McCloskey et al.[30] and Harding et al.[139, 140] was utilized to monitor oxygen consumption during discharge and gas evolution on charge. Oxygen consumption during galvanostatic discharge at 200 $mA \cdot g^{-1}_{Carbon}$ of O_2 electrodes was quantified via pressure drop monitoring of the O_2 atmosphere in the cell at two second intervals. The ideal gas law is used to convert pressure change to the amount O_2 consumed. O_2, CO_2, and H_2O evolution during potentiostatic charge of both O_2 and Li_2O_2-preloaded electrodes was quantified at 15-minute intervals using a 200 amu precision residual gas analyzer (mass spectrometer, Stanford Research Systems Inc.) coupled with pressure monitoring. Linear interpolation

is used to match electrochemical and DEMS measurements in the all figures presented herein. Details of DEMS and cell technical construction are available online.[140]

4.3. Results and discussion

4.3.1. O_2 and parasitic gases from Li_2O_2 oxidation

The principal interest of the present work is in elucidating the gases evolved in the OER during Li_2O_2 oxidation. Evolution of O_2 and parasitic gases such as CO_2, CO, and H_2O as measured by a residual gas analyzer during potentiostatic charging at 3.9 V_{Li} are plotted as a function time in Figure 4-1. In both Li_2O_2-preloaded and O_2-electrodes, little to no evolution of CO and H_2O are observed. O_2 and CO_2, the major charging species,[23, 32] are the main gases detected during charge as a result of expected oxidation of Li_2O_2 as well as parasitic carbonate products. Thereby, the following discussions are concerned with the evolutions of O_2 and CO_2.

In Li_2O_2-preloaded electrodes, the amount of parasitic CO_2 (Figure 4-1a-d) formed on charging is one to two orders of magnitude lower than O_2 at 3.9 V_{Li}. In a VC-only Li_2O_2-preloaded electrode (Figure 4-1a) charged at 4.4 V_{Li} (chosen to enable reasonable rate of charging since VC shows negligible oxidation activity of preloaded commercial Li_2O_2 at 3.9 V_{Li}[133, 141, 142]), a greater amount of CO_2 is measured on charge compared to the promoted electrodes charged at 3.9 V_{Li}, likely from electrolyte decomposition at the higher applied potential. In O_2-electrodes (Figure 4-1f-h), Li_2O_2 electrooxidation at 3.9 V_{Li} following discharge evolved measurably more CO_2 as compared to corresponding Li_2O_2-preloaded electrodes (particularly for Mo and Cr). This finding is consistent with the reported formation of Li_2CO_3, HCO_2Li, CH_3CO_2Li electrolyte decomposition products on discharge in ethers such as diglyme.[23, 32] The oxidative decomposition of

these carbonates (which has previously been shown to oxidize between 3.5 and 4.0 V_{Li} at 70 $mA \cdot g^{-1}_{Carbon}$[143]) on subsequent charging at 3.9 V_{Li} may explain the moderately greater presence of CO_2 compared to preloaded electrodes where discharge is bypassed for the purpose understanding the Li_2O_2 oxidation reaction with minimal interference from parasitic discharge products.

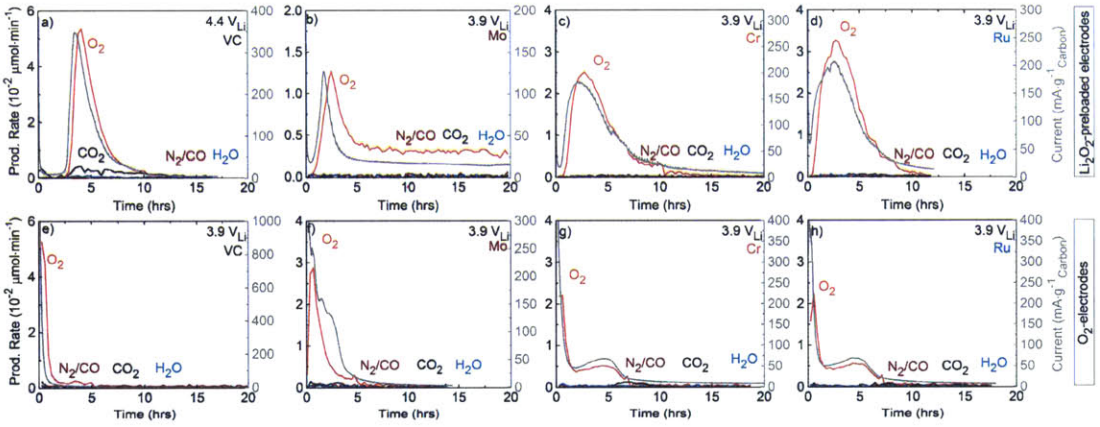

Figure 4-1. Non-normalized O_2, CO_2, CO, H_2O production rates obtained on first cycle charging (a, b, c, d) Li_2O_2-preloaded electrodes and (e, f, g, h) O_2-electrodes charged following first cycle galvanostatic discharge at 200 $mA \cdot g^{-1}_{Carbon}$ = 300 $mA \cdot g^{-1}_{[Mo, Cr, Ru]}$ (see Figure 4-3a for discharge voltage profiles of e, f, g, h). Top right corner annotations correspond to applied potential and added transition metal promoter (from left to right: VC only, Mo, Cr, Ru). Grey lines corresponds to current shown on the right y-axes.

O_2 is unambiguously the main gas evolved from Li_2O_2 oxidation both from commercial chemically synthesized Li_2O_2 as well as upon charging of electrochemically discharged Li-O_2 cells (Figure 4-1). The O_2-evolution during the OER in both Li_2O_2-preloaded and O_2-electrodes follows the faradaic current profiles in all cases presented in Figure 4-1. It

is interesting to note a time delay in the evolution of O_2 in Li_2O_2-preloaded electrodes after imposing the potentiostatic voltage. This delay is on the order of 2.5 hours in VC:Li_2O_2 electrodes while being less than 0.25 hours in electrodes promoted by transition metal Mo, Cr, and Ru. Shorter time delay in promoted electrodes trends with greater faradaic activity of the electrode[133] with the initial low O_2 evolution corresponding to an initial drop in electrode current (Figure 4-1). This phenomenon referred to as 'activation'[78, 133, 141] was previously noted in the current by Harding et al.[141] and seen in the O_2 profile of Li_2O_2-preloaded electrodes using OEMS.[142]

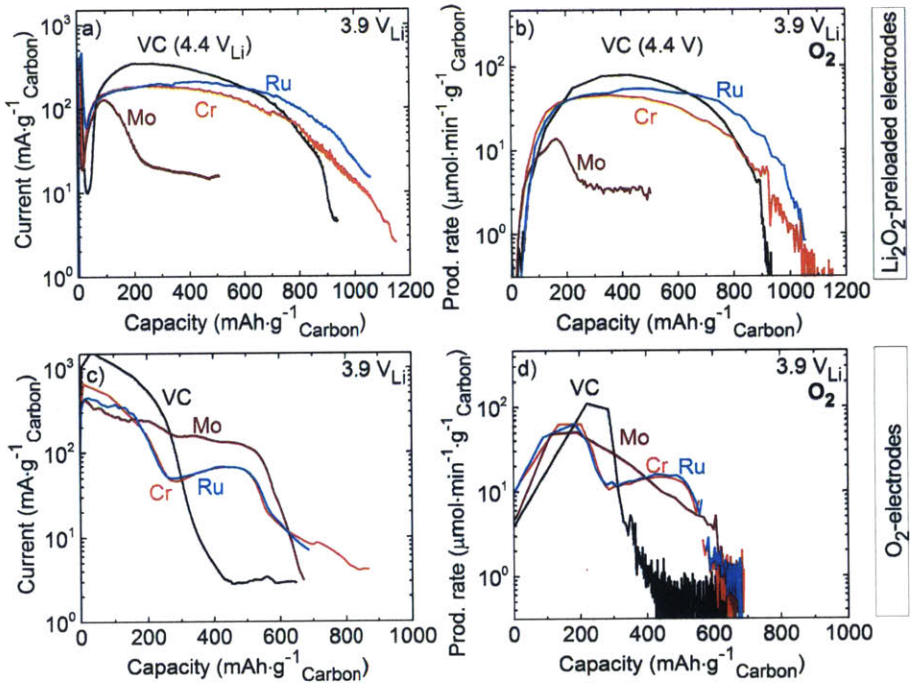

Figure 4-2. O_2 evolved on first cycle charge of (a, b) Li_2O_2-preloaded electrodes [Mo, Cr, Ru]:VC:Li_2O_2:LiNafion = 0.667:1:1:1 and (c, d) O_2-electrodes [Mo, Cr, Ru]:VC:LiNafion = 0.667:1:1. (a, c) are current profiles at the potentiostatic applied potential of 3.9 V_{Li} and (b, d) are O_2 production rates. Y-axis scale in (b, d) are aligned (a, c) according to 2 e^-/O_2 expected. Note that VC:Li_2O_2:LiNafion = 1:1:1 in (a) is

charged at 4.4 V_{Li} chosen to enable reasonable rate of charging since VC shows negligible oxidation activity of preloaded Li_2O_2 at 3.9 V_{Li}[133, 141, 142].

Compared to previously reported findings in DME-based electrolytes,[133] we observe decreased performance in diglyme electrolyte for all metal promoters in Li_2O_2-preloaded electrodes (Figure 4-2a). Current output are significantly reduced (average currents: 423, 258, and 187 $mA \cdot g^{-1}_{Carbon}$ in DME[133] versus 43, 103, and 142 $mA \cdot g^{-1}_{Carbon}$ in diglyme for Mo, Cr, and Ru promoters respectively). It is conceivable that the higher viscosity of diglyme (viscosity = 0.981 mPa.s[144], O_2 diffusion coefficient = $4.4 \cdot 10^{-5}$ $cm^2 \cdot s^{-1}$ [145]) versus DME (viscosity = 0.4341[146], O_2 diffusion coefficient = $6.0 \cdot 10^{-5}$ $cm^2 \cdot s^{-1}$ [145]) results in significantly greater local O_2 concentration at the Li_2O_2 oxidation site which would negatively impact the kinetics of the $Li_2O_2 \rightarrow 2Li^+ + 2e^- + O_2$ reaction.

In O_2-electrodes during the first cycle (Figure 4-2c), average current in units of $mA \cdot g^{-1}_{Carbon}$ was observed as Mo (171) > Cr (147) ≈ Ru (135) in agreement with previous trend in faradaic activities.[133] The reference VC-only O_2-electrode charged at 3.9 V_{Li} started at high current values but precipitously dropped to a current lower than that of Mo, Cr, and Ru in Figure 4-2c after ~300 $mAh \cdot g^{-1}_{Carbon}$ and remained at ~ 3 $mA \cdot g^{-1}_{Carbon}$ for the remainder 18 hours of charging (Figure 4-1e). It is worth highlighting that the "dropping current" step at 3.9 V_{Li} in VC-only O_2-electrodes seemed to correspond with the first O_2 wave in Cr and Ru promoted electrodes. Only one O_2-wave spanning its full capacity was observed for Mo electrodes. This step likely corresponds to the sloping first stage during galvanostatic charging for which McCloskey et al.[30] have measured high rates of O_2-evolution similarly to those in Figure 4-2d. This first stage has been assigned to facile rate-insensitive delithiation and disproportionation of Li_2O_2 by Lu et al.[147]

In addition to good agreement between change in current and O_2-evolution noted in Figure 4-1, ordering of activities seen from faradaic current is nominally preserved in the flux of O_2 evolved. Notably, Cr and Ru promoted electrodes show comparable currents at 3.9 V_{Li} in both Li_2O_2-preloaded and O_2-electrodes; their comparable first cycle current output is accompanied by practically overlapping O_2-evolution profiles in Figure 4-2b and Figure 4-2d. On the other hand, the charging behavior of Mo-promoted electrodes from Li_2O_2-preloaded to O_2-electrodes warrants further discussion. The high current wave of Li_2O_2-preloaded Mo electrodes spanned only ~227 $mAh \cdot g^{-1}_{Carbon}$ followed by a low ~20 $mA \cdot g^{-1}_{Carbon}$ lasting approximately 15 hours with incomplete charging before termination of the cell after 20 hours as seen in Figure 4-1b. In contrast, in O_2-electrodes with Li_2O_2 formed in operando, a relatively high faradaic activity of Mo with complete charging is observed in Figure 4-2c. It is likely that incomplete recharge of preloaded Mo electrodes stems from stronger conversion of Mo with Li_2O_2 to form Li_2MoO_4 in the pristine electrode state.[133] Contact time between Li_2O_2 formed in operando and the Mo promoter is on the order of 10 hour (imposed rest period between discharge and charge) in O_2-electrode compared to a few days of drying and glovebox storage in the case of Li_2O_2-preloaded electrodes. With limited contact time between Li_2O_2 and Mo, only limited surface conversion occurs that maintains the greater mass-activity of Mo compared to Cr and Ru in agreement with previous observations.[133]

4.3.2. Rate of O_2 consumption during discharge

O_2 consumption during discharge in presence of promoters O_2-electrodes was investigated during galvanostatic discharge at 200 $mA \cdot g^{-1}_{Carbon}$ by monitoring of pressure drop in the O_2 atmosphere within the cell. First cycle discharge voltage profiles in

presence of Mo, Cr, and Ru promoters are shown in Figure 4-3a and compared to a reference VC-only electrode. All voltage profiles show an initial short dip and a plateau at ~2.6 V_{Li} which agrees with the discharge of VC-only. In effect, discharge in presence of all promoters is characteristic of the VC carbon support used in the electrode. The initial higher capacity of VC-only compared to metal-promoter-containing electrodes is likely due to variability in capacity seen in Li-O_2 batteries.[45] As mentioned above, 2 e^-/O_2 is expected on discharge for formation of Li_2O_2 from O_2 in Li-O_2 cells; Figure 4-3d summarizes the adhesion to this discharge pathway of Li-O_2 cells in presence of Mo, Cr, and Ru on the first cycle. Comparing the gas consumption with faradaic charge measured in Figure 4-3d, it is clear that a nominally 2 e^-/O_2 reduction reaction is occurring throughout the first cycle discharge for all promoters studied and VC-only electrodes. The actual fitted slope of first discharge yielded ~2.1 e^-/O_2 for all four measurements. We confirm therefore that formation of Li_2O_2 is the main electrochemical process occurring during discharge of Li-O_2 in presence of Mo, Cr, and Ru.

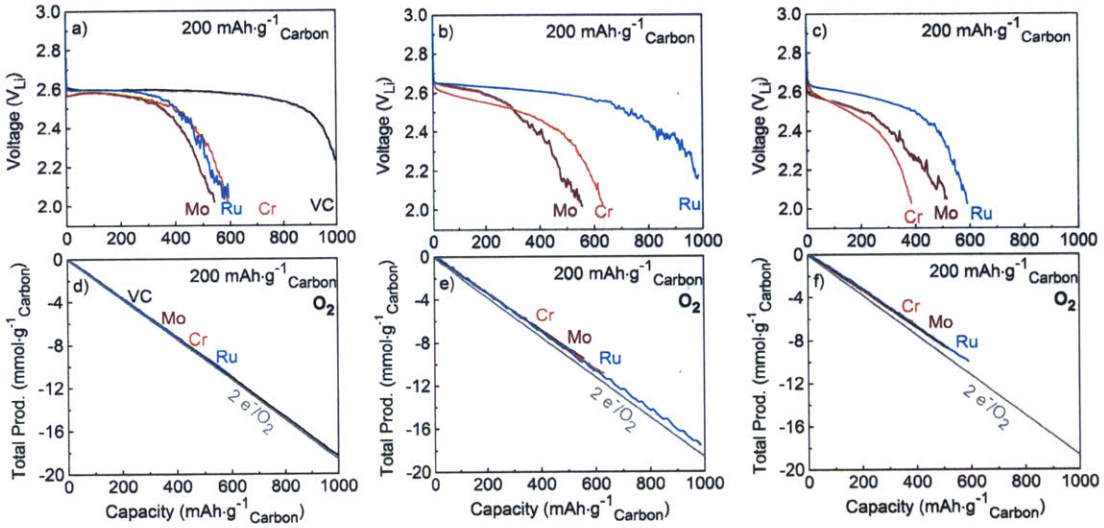

Figure 4-3. First (a, d), second (b, e), third (c, f) discharge cycles of O_2-electrodes of VC-only (VC:LiNafion = 1:0.5) and transition metal promoted [Mo, Cr, Ru]:VC:LiNafion = 0.667:1:1. Top panels (a, b, c) are voltage profiles and bottom panels (d, e, f) are illustrations of e^-/O_2 values on first, second, and third galvanostatic discharge cycles at 200 $mA \cdot g^{-1}_{Carbon}$. Grey line in (d, e, f) corresponds to the ideal 0.01865 mmol of O_2 per mAh of charge for the 2 e^-/O_2 ($2Li^+ + 2e^- + O_2 \rightarrow Li_2O_2$) reaction.

While on the first cycle, capacities and voltages in Mo, Cr, and Ru promoted O_2-electrodes are comparable at ~600 $mAh \cdot g^{-1}_{Carbon}$ and ~2.5 V_{Li} average voltage, on the subsequent second and third discharge cycles, capacities at the voltage cut-off of 2.0 V_{Li} remained between 400 and 600 $mAh \cdot g^{-1}_{Carbon}$ for Mo and Cr electrodes. Ru electrodes displayed 1000 $mAh \cdot g^{-1}_{Carbon}$ on the second cycle which is within capacity variation for VC-based electrodes and somewhat slower decay in discharge voltage over cycles (Figure 4-4a, b). In terms of correspondence between O_2 reduction to Li_2O_2 and current, Figure 4-3e and f suggest a decrease in O_2 consumption rate per unit current passed on

successive cycles. Moderate increase in e^-/O_2 in all promoted electrodes is observed as visualized in Figure 4-5. The increase in e^-/O_2 shown might be linked to accumulation of parasitic degradation species in the electrode and electrolyte over cycles which may undergo side reduction reactions in parallel with the main O_2 reduction.[22, 32]

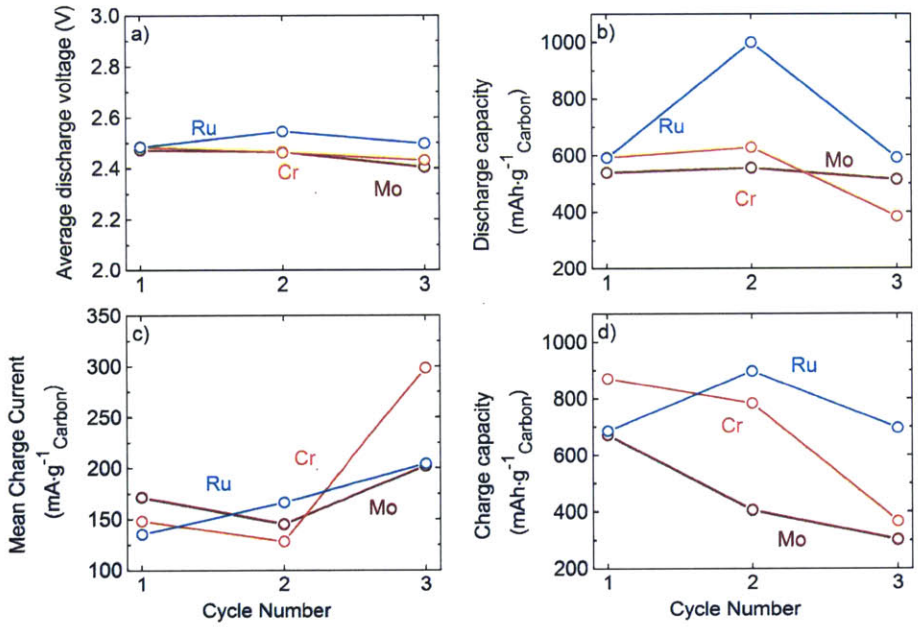

Figure 4-4. Measures of cell performance on discharge in (a, b) and charge (c, d) of transition metal promoted [Mo, Cr, Ru]:VC:LiNafion = 0.667:1:1 O_2-electrodes. Mathematical average over capacity of discharge voltage at 200 $mA \cdot g^{-1}_{Carbon}$ (a) and charge current at 3.9 V_{Li} (c) versus cycle numbers. Capacities at the end of discharge (b) and charge (d).

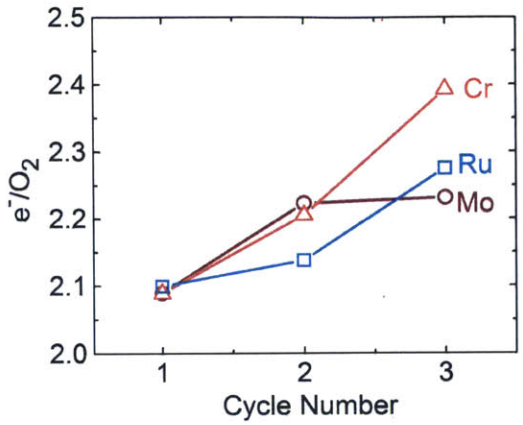

Figure 4-5. e^-/O_2 versus cycle number during discharge of O_2-electrodes of [Mo, Cr, Ru]:VC:LiNafion = 0.667:1:1 electrodes in Li-O_2 cells. A general decrease in O_2 consumption rate per faradaic current passed is revealed as increasing e^-/O_2. Note the 0.5 e^-/O_2 range of y-scale.

4.3.3. Rate of O_2 evolution during Li_2O_2 oxidation on charge

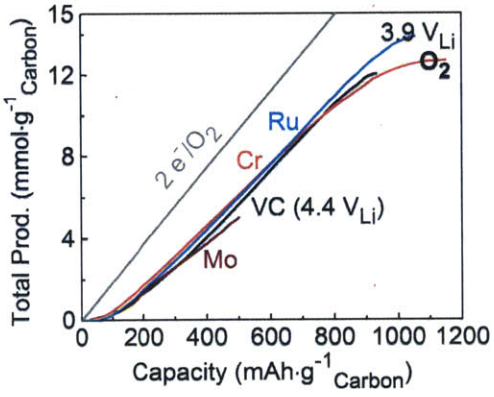

Figure 4-6. Illustration of e^-/O_2 during potentiostatic charging at 3.9 V_{Li} of Li_2O_2-preloaded [Mo, Cr, Ru]:VC:Li_2O_2:LiNafion = 0.667:1:1:1 electrodes. Note that the VC-only (VC:Li_2O_2:LiNafion = 1:1:1) electrode is charged at 4.4 V_{Li}. Grey line corresponds to the ideal 0.01865 mmol of O_2 per mAh of charge for a 2 e^-/O_2 reaction.

On charge, although O_2 production rates generally trace the current profiles, rates of oxygen evolution upon charging are less than would be expected from measured currents considering the 2 e^-/O_2 oxidation both in Li_2O_2-preloaded and O_2-electrodes (where Li_2O_2 is formed electrochemically as shown by ~2.1 e^-/O_2 discharge in Figure 4-3d).

In Li_2O_2-preloaded electrodes shown in Figure 4-6, an initial regime with large 6-9 e^-/O_2 is observed which aligns with electrode activation and little O_2 evolution.[133, 141, 142] Activation of the oxidation of commercial Li_2O_2 seems to require an initial electrochemical reaction with low oxygen generation. For Cr and Ru Li_2O_2-preloaded electrodes in Figure 4-6 which approached full capacity of 1168 $mAh \cdot g^{-1}_{Carbon}$, another regime of 4-7 e^-/O_2 at the end of charge is observed that coincides with precipitous drop in current. Between these two regimes, a more linear regime with 2.5, 3.1, 2.6, 2.3 e^-/O_2 in VC, Mo, Cr, and Ru promoted electrodes respectively is evident.

On the first cycle of O_2-electrodes charged following discharge (Figure 4-7d), values of 2.7, 4.2, 2.7, and 2.7 e^-/O_2 in VC, Mo, Cr, and Ru promoted electrodes respectively. A slope change with 5-9 e^-/O_2 can be seen at the end of charging as current drops precipitously past the ~600 $mAh \cdot g^{-1}_{Carbon}$ in promoted electrodes (only ~643 $mAh \cdot g^{-1}_{Carbon}$ out of ~1000 $mAh \cdot g^{-1}_{Carbon}$ was recovered on charge for VC-only electrode resulting in incomplete charging after 20 hours).

The lower rate of O_2 evolution versus measured current close to the end of charge is likely due to greater amount of side reactions occurring at the potentiostatic voltage as Li_2O_2 is depleted towards the end of charge. Indeed a measurable increase in CO_2 is seen towards the end of O_2-electrode charging in the specific case of Cr and Ru (Figure 4-1g, h). In the case of Mo-promoted O_2-electrodes, CO_2 evolved concomitantly with O_2

(Figure 4-1f) and the shape of the e^-/O_2 curve as seen in Figure 4-7d is correspondingly highly nonlinear. We note that prior studies utilizing DEMS or OEMS for gas quantification during Li_2O_2 oxidation generally report O_2 regeneration lower than expected from measured current in Li-O_2 cells.[30, 96, 121, 142, 148] McCloskey et al.[30, 91, 148] report values of 2.6 up to 3.2 e^-/O_2 in recharging O_2-electrodes with the LiTFSI/monoglyme (DME) electrolyte. Meini et al. used OEMS to report values of 2.6 e^-/O_2[142] and 2-2.4 e^-/O_2[121] in preloaded electrodes with LiTFSI/diglyme electrolyte and carbon-only electrode.

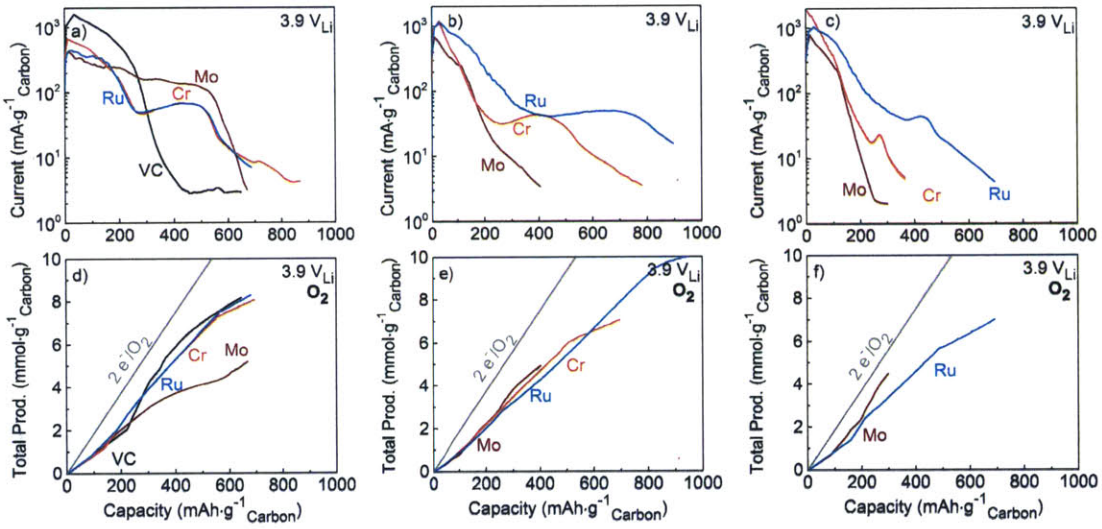

Figure 4-7. First (a, d), second (b, e), third (c, f) charge cycles (following discharge cycles shown in Figure 3) of O_2-electrodes of VC-only (VC:LiNafion = 1:0.5) and transition metal promoted [Mo, Cr, Ru]:VC:LiNafion = 0.667:1:1. Top panels (a, b, c) are current profiles and bottom panels (d, e, f) are illustrations of e^-/O_2 values on first, second, and third potentiostatic charge cycles at 3.9 V_{Li}. Missing Cr curve in (f) is a result of instrumental failure on the third DEMS cycle of Cr. Grey line in (d, e, f) corresponds to the ideal 0.01865 mmol of O_2 per mAh of charge for a 2 e^-/O_2 reaction.

4.3.4. Mechanistic discussion of O_2 regeneration rate on Li_2O_2 oxidation

Results presented above for the O_2 release on charge can be interpreted in the framework of our proposed mechanism of enhancement of Li_2O_2 oxidation proceeding through an intermediate chemical conversion to a lithium-rich transition metal oxide followed by electrochemical delithiation. Mo-promoted electrodes show particularly large values of e^-/O_2 slopes with 3.1 in Li_2O_2-preloaded electrodes and 4.2 on the first cycle in O_2-electrodes. We postulate that the greater deviation of Mo electrodes from the stoichiometric value of 2 e^-/O_2 is a reflection of the greater driving force for reaction with Li_2O_2 to Li_2MoO_4 (partially oxidized, -939 $kJ \cdot mol^{-1}_{Mo}$) compared to Li_2CrO_4 for Cr (Cr_2O_3-coated, -440 $kJ \cdot mol^{-1}_{Cr2O3}$) and Li_2RuO_3 for Ru (partially oxidized, -446 $kJ \cdot mol^{-1}_{Ru}$).[122, 133] The delithiation at 3.9 V_{Li} ($Li_2MO_{(y = 3, 4)} \leftrightarrow 2Li^+ + MO_x + \frac{1}{2}(y-x)O_2$) of the chemically lithiated metal oxide which contributes to the externally measured activity of electrodes is not expected to result in 2 e^-/O_2. This observation is further reflected in Figure 4-8 where the ratio of O_2 evolved on charge (potentiostatic 3.9 V_{Li}) over O_2 consumed on discharge (galvanostatic 200 $mA \cdot g^{-1}_{Carbon}$) is observed to be lower for Mo at ~52% on the three cycles while starting at ~75% for both Cr and Ru and decreasing in unison to 60-70% on the subsequent 2 cycles. We note comparing discharge capacities in Figure 4-4b to charge capacities in Figure 4-4d that Cr and Ru showed comparable round-trip coulombic efficiencies in O_2-electrodes over three cycles with some overcharge during galvanostatic charging. Coulombic recovery for Cr and Ru over cycling appeared more optimal compared to Mo in agreement with the O_2 regeneration trends. Coulombic recovery for Cr and Ru over cycling appeared more optimal compared to Mo in agreement with the O_2 regeneration trends in Figure 4-8. We note that

the round-trip O_2 utilization for VC-only O_2 electrodes on the first cycle was 45% as a result of incomplete charging at 3.9 V_{Li} linked to the low activity of VC as a promoter of the Li_2O_2 oxidation.

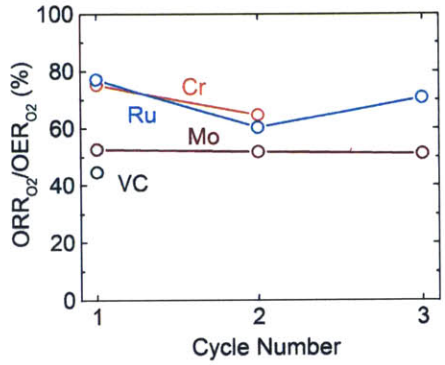

Figure 4-8. Round trip ratio of O_2 evolved on charge (potentiostatic 3.9 V_{Li}) over O_2 consumed on discharge (galvanostatic 200 $mA \cdot g^{-1}_{Carbon}$) as a function of cycles in O_2-electrodes [Mo, Cr, Ru]:VC:LiNafion = 0.667:1:1 and VC:LiNafion = 1:0.5.

Values of 3.0 and 2.6 e^-/O_2 are recorded on the second and third cycles of Mo approaching the ideal 2 e^-/O_2 as compared to the first cycle 4.2 e^-/O_2 (Figure 4-9). We speculate that a permanent oxide layer forms (MoO_2 or MoO_3) on the surface of Mo particles after the first cycle delithiation of Li_2MoO_4 that mitigates conversion on subsequent cycles ($Li_2O_2 + MoO_3 \leftrightarrow Li_2MoO_4 + ½\ O_2$, enthalpy = -158 $kJ \cdot mol^{-1}_{MoO3}$).[122, 133] This permanent surface oxidation following first charge has been reported for TiC[21] and Mo_2C.[134] In the case of Mo metal nanoparticle promoters it translates into reduced faradaic activity and round-trip coulombic efficiency on the second and third cycles as compared to its first cycle (Figure 4-7b, c and Figure 4-4c, d). This observation is in agreement with MoO_2 and/or MoO_3 having lower electrochemical activity accompanying greater stability against chemical conversion.[133]

It is noteworthy that Cr and Ru maintain comparable e^-/O_2 on charge over the first two cycles reported (Figure 4-9, see also Figure 4-7d, e). Cr electrodes showed 2.7 and 3.1 e^-/O_2 on the first and second cycles respectively while Ru electrodes showed 2.7 and 3.2 e^-/O_2. Similarity of faradaic current (Figure 4-2a, c), O_2 evolution efficacy (Figure 4-2b, d), round-trip O_2 utilization (Figure 4-8) and values of e^-/O_2 (Figure 4-6 and Figure 4-9) on at least two cycles between Cr and Ru agrees with their comparable enthalpies of conversion with Li_2O_2 and equivalent BET surface areas listed previously (values of enthalpies are listed in Table 3-2).[133]

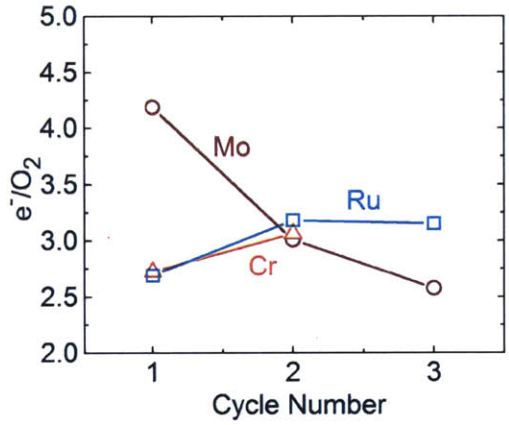

Figure 4-9. e^-/O_2 versus cycle number during charge of O_2-electrodes of [Mo, Cr, Ru]:VC:LiNafion = 0.667:1:1 electrodes in Li-O_2 cells. A general decrease in O_2 evolution per faradaic current passed is revealed as increasing e^-/O_2. In the specific case of Mo electrodes, a decrease in e^-/O_2 closer to the ideal value of 2 e^-/O_2 suggests stabilization of the electrode surface by oxidation.

4.4. Conclusion

In conclusion, metal nanoparticle promoters offer an avenue for reduction of the large overpotential pervasive during the recharge of Li-O_2 cells and thereby increase recharge

efficiency and lower parasitic oxidation of the organic electrolyte. In this work, we investigate the process efficiency of promising promoter nanoparticles Mo, Cr, and Ru. The following four major findings are highlighted: (i) Li_2O_2 with 2 e^-/O_2 is the major discharge product independent of the presence of Mo, Cr, or noble metal Ru. The discharge pathway ($2Li^+ + O_2 \leftrightarrow Li_2O_2$) is generally unaffected by the promoter nanoparticle as revealed through discharge plateau voltage of ~2.6 V_{Li} at 200 $mA \cdot g^{-1}_{Carbon}$ common for all three metal promoters studied as well as plain VC-only O_2-electrodes. (ii) Oxidation of the Li_2O_2 discharge product results in rates of regeneration of O_2 lower than expected from measured charge currents in agreement with literature reports. In particular, Mo electrodes depart strongly from 2 e^-/O_2 likely as a result of the greater thermodynamic driving force (-939 $kJ \cdot mol^{-1}$ for $Li_2O_2 + Mo + O_2 \leftrightarrow Li_2MoO_4$) for conversion of Mo with Li_2O_2 towards Li_2MoO_4. In contrast Cr and Ru with lower and similar conversion enthalpies (approximately -440 $kJ \cdot mol^{-1}$ for $Li_2O_2 + 1/2Cr_2O_3 + 1/2O_2 \leftrightarrow Li_2CrO_4$ and $Li_2O_2 + Ru + 1/2O_2 \leftrightarrow Li_2RuO_3$), display values of 2.7-3.2 e^-/O_2. Remarkably, the correlation between conversion enthalpy and promoter electrochemical activity is further reflected in the similarity between Cr and Ru in terms of both current and oxygen evolution rates and round-trip efficiencies at 3.9 V_{Li} in Li_2O_2 preloaded as well as O_2-electrodes. Low cost Cr-based nanoparticles could be an excellent substitute for higher cost noble metal Ru charging promoters extensively used in Li-O_2 batteries. (iii) Only minor amount of CO_2, CO and H_2O are measured during cycling charging at 3.9 V_{Li}, which emphasize the utility of promoter nanoparticles to enable charging voltage below 4.0 V_{Li} for improved electrolyte stability.

Chapter 5. On the utilization of cobalt bis(terpyridine) metal complex as soluble redox mediator in Li-O_2 batteries

Adapted from manuscript draft submitted to the Journal of Physical Chemistry C. This work was done in collaboration with James T. Frith, Sayed Youssef Sayed, Fanny Bardé, John R. Owen, Yang Shao-Horn, Nuria Garcia-Araez. Cyclic voltammetry in Figure 5-1 and viscosity measurements in this chapter are explicitly credited to James T. Frith at the University of Southampton.

5.1. Introduction

From Chapter 2 through to Chapter 4, we have investigated the use of solid-state metal nanoparticles to address one of the key bottleneck in the development of Li-O_2 batteries, i.e the inefficiency of the charging process. The discharge product Li_2O_2 is nominally an electronic insulator (~10^{-12} $S \cdot cm^{-1}$)[40, 52] and the oxygen evolution reaction from its oxidation has sluggish kinetics; therefore, high overpotentials are required to charge Li-O_2 cells. High charging voltages, in turn, induce several undesired reactions such as electrolyte degradation[26, 30, 149, 150] and corrosion of carbon containing electrodes.[23, 24, 151-153] The combination of high charging voltage and parasitic degradation results in poor round trip efficiencies and limited cycling.

It has been shown that certain soluble redox agents (referred to as redox mediators), enhance the charging kinetics of Li-O_2 cells by mediating the electron transfer from Li_2O_2 to the electrode surface. The soluble redox agent (denoted M in reactions (5.1) and (5.2) below) is first oxidized on exposed carbon surfaces. Then, the oxidized form of the mediator chemically oxidizes Li_2O_2 evolving oxygen and releasing Li^+ cations into the electrolyte.[60, 61]

$$M \rightarrow M^+ + e^- \quad (5.1)$$

$$2M^+ + Li_2O_2 \rightarrow 2M + O_2 + 2Li^+ \quad (5.2)$$

Since chemical oxidation of Li_2O_2 is initiated by the electro-oxidation of the redox agent, it is expected that the charging potential of the cell will be close to the reversible potential of the redox agent, $E^0(M^+/M)$. For the chemical reaction (5.2) to proceed, it is

necessary that $E^0(M^+/M)$ is greater than the reversible potential of ($2Li^+ + O_2 + 2e^- \leftrightarrow Li_2O_2$), i.e 2.96 V_{Li}.

Several redox mediators have been demonstrated such as TTF,[61] TEMPO,[110] transition metal phthalocyanines[154] and iodine,[111, 155-160] with varying degrees of efficiency on enhancing the kinetics of the charge reaction. The requirements for efficient redox mediators are: i) fast and reversible electron transfer kinetics, ii) fast reaction with Li_2O_2 to evolve oxygen, iii) absence of degradation reactions, and iv) formal potential $E^{0'}(M^+/M)$ higher than 2.96 $V_{Li,}$ but not too high so as to afford low charging potentials (see the discussion below). The conditions in which Li-O_2 batteries operate (high voltages and presence of oxygen and reactive reaction intermediates such as superoxide) make it difficult to find redox reagents that satisfy the above listed conditions simultaneously. Specifically, it is difficult to enhance the rate of reaction of Li_2O_2 with the redox agent because the reaction mechanism is poorly understood. Although, to first order, the reaction rate is expected to increase with increasing $E^{0'}$ of the redox agent, since the driving force for the electron transfer reaction between the redox agent and Li_2O_2 (reaction 5.2) will increase. On the other hand, if the redox potential of the redox agent is too high, charging of the Li-O_2 cell will require high voltages, where significant electrolyte degradation takes place.

In this work, we compare the cobalt bis(terpyridine) ($Co(Terp)_2$) complex and the well-known tetrathiafulvalene (TTF)[61] as redox mediators in Li-O_2 cells using electrochemical characterization, X-ray diffraction (XRD) and differential electrochemical mass spectrometry (DEMS) measurements. $Co(Terp)_2$ was selected because, as with other metal complexes, it undergoes fast and reversible electron transfer

reactions. Having cobalt as the metal center is suitable as the Co^{II} to Co^{III} process is located in a potential window where the mediated oxidation of Li_2O_2 is thermodynamically favorable, ie. $E^{0'}(Co^{II}/Co^{III})$ in $Co(Terp)_2$ is higher than 2.96 V_{Li}. Cobalt complexes are known to undergo changes in their coordination sphere, between octahedral and tetrahedral geometries, during electron transfer reactions.[161] Therefore, a tridentate ligand such as bis(terpyridine) was chosen in order to strengthen the metal-ligand interaction and to minimize possible side-reactions such as de-complexation and formation of cobalt oxide. Herein, we show that the redox potential of metal complexes can be easily tuned by changing the solvent. This effect is related to the shift in potential of the lithium counter electrode, and therefore, applicable to most mediators, including TTF. By carefully changing the solvent composition, the onset of the charging reaction of Li-O_2 cells can be decreased to ca. 3.2 V_{Li}. However, some shortcomings of both $Co(Terp)_2$ and TTF were elucidated using DEMS and are discussed in detail.

5.2. Experimental

5.2.1. Reagents

Cobalt (II) bis(terpyridine) bis(trifluoromethane)sulfonylimide was synthesized according to the literature.[162] An aqueous solution of cobalt (II) chloride ($CoCl_2$, Puriss $\geq$ 98.5 %, Fluka) was added drop wise to solution of 2,2':6',2"-terpyridine (Terp, 98 %, Sigma-Aldrich) in the molar ratio 1:2. This produced a yellow solution. Excess lithium bis(trifluoromethane)sulfonylimide (LiTFSI, 99.95 %, Sigma-Aldrich) in water was then added, causing a red/brown product to precipitate out of solution. The product was then washed with water and dried overnight under vacuum at 80 °C before being stored in a

dry glove box. Commercially available tetrathiafulvalene (97%) was purchased from Sigma-Aldrich and used after drying at 70 °C under vacuum in a Buchi B585 glass oven.

5.2.2. Electrolytes solutions

LiTFSI used in the preparation of electrolyte solutions was dried under vacuum at 120 °C for 48 h. The ionic liquid pyrrolidinium bis(trifluoromethane)sulfonylimide (Pyr_{14}TFSI, 99.5%, IoLiTec) was dried under vacuum at 120 °C for 48 h. Diethylene glycol dimethyl ether (diglyme, anhydrous 99.5 %, Sigma-Aldrich) was dried using molecular sieves (3 Å, beads, 4-8 mesh, Sigma-Aldrich). Electrolyte solutions of 1 M LiTFSI in diglyme, 1 M LiTFSI in Pyr_{14}TFSI:diglyme = 1:1 (volume ratio), and 0.1 M LiTFSI in Pyr_{14}TFSI were prepared in an argon-filled glove box (H_2O < 0.1 ppm and O_2 <0.1 ppm).

5.2.3. Cyclic voltammetry

Cyclic voltammetry experiments were carried out in a two electrode split cell. Lithium metal (30 mm diameter, 150 μm thick, RockWood Lithium Inc.) was used as a counter and reference electrode and was housed in the negative electrode compartment of the cell. In all cases the electrolyte in the negative electrode compartment did not contain either of the mediators $Co^{II}(Terp)_2$ or TTF. A 3 mm ø glassy carbon electrode was used as the working electrode and was housed in the positive electrode compartment of the cell with an electrolyte consisting of LiTFSI in varying concentrations depending on the solvent and 2 mM $Co^{II}(Terp)_2$ or TTF. CVs were recorded under an Ar atmosphere at 20 mV s^{-1} from 2 to 4 V_{Li}.

5.2.4. Electrochemical testing

Electrolytes with 50 mM of a redox mediator ($Co^{II}(Terp)_2$ or TTF) dissolved in 1 M LiTFSI/diglyme or 1 M LiTFSI/Pyr_{14}TFSI:diglyme were prepared for the purpose of Li-O_2 cell testing. Electrochemical cells consisted a "2-compartment cell"[114] of the following stack: lithium foil (15 mm diameter, 150 μm thick, RockWood Lithium Inc.), battery membrane separator (18 mm diameter, C480, Celgard) wetted with 50 μL 1 M LiTFSI/diglyme, a Lithium-Ion Conducting Glass-Ceramic electrolyte (19 mm diameter, 150 μm thick, LICGC™, Ohara Corp.), Whatman GF/A separator wetted with 200 μL of electrolyte (1 M LiTFSI/diglyme or 1 M LiTFSI/Pyr_{14}TFSI:diglyme with or without 50 mM of redox mediator), free standing vertically aligned carbon nanotubes (CNT, 1 cm^2 square geometry, 0.4 to 1.2 mg),[163] and stainless steel current collector. The Ohara glass electrolyte in the "2-compartment cell" configuration suppresses the crossover of redox mediator from cathode to anode which may result in an undesired internal electrochemical shuttling.[164] All cell assembly and pressurization with O_2 was carried within an argon-filled glovebox. All galvanostatic discharge and charge of thus assembled cells was performed at a rate of 200 $mA \cdot g^{-1}_{CNT}$ using a research-grade multi-channel potentiostat (VMP3, BioLogic Inc.)

5.2.5. Differential electrochemical mass spectroscopy (DEMS)

A custom-made DEMS based on a configuration reported by McCloskey et al.[30] and Harding et al.[139, 140] was used for measurement of oxygen consumption during discharge and gas evolution on charge at 200 $mA \cdot g^{-1}_{CNT}$. Oxygen consumption during galvanostatic discharge was quantified via pressure drop monitoring at two second intervals. O_2, CO, CO_2, and H_2O evolution during charge was quantified at 15-minute intervals using a mass

spectrometer coupled with pressure monitoring. Details of DEMS and cell technical construction are available online.[140] Li-O_2 cells for DEMS underwent the following electrochemical sequence: 12-hour rest period, 5-hour discharge to 1000 $mAh \cdot g^{-1}_{CNT}$, 10-hours rest, and charging to 4.5 V_{Li} cut-off.

5.3. Results and discussion

Results of cyclic voltammetry (CV) investigation of $Co(Terp)_2$ and TTF on a glassy carbon electrode in 3 different solvents: diglyme, 1-butyl-1-methylpyrrolidinium bis(trifluoromethanesulfonyl)imide ($Pyr_{14}TFSI$), and $Pyr_{14}TFSI$:diglyme = 1:1 (volume ratio) are shown in Figure 5-1. The peak cathodic and anodic currents decrease in the order diglyme (η = 2.96 mPa·s) > $Pyr_{14}TFSI$:diglyme (η = 20.7 mPa·s) > $Pyr_{14}TFSI$ (η = 79 mPa·s) both for $Co(Terp)_2$ (Figure 5-1a) and TTF (Figure 5-1b). During cyclic voltammetry of a reversible analyte,[165] peak current is a function of the number of electrons exchanged (n), the electrode surface area (A), the diffusion coefficient of the analyte (D), the scan rate (v), and the analyte bulk concentration (C^*). Their relation is approximated by the following equation 5.3

$$i_p = (2.69 \cdot 10^{-5}) \cdot n^{\frac{3}{2}} \cdot A \cdot D^{\frac{1}{2}} \cdot \vartheta^{\frac{1}{2}} \cdot C^* \tag{5.3}$$

The Stokes-Einstein hard sphere diffusion is stated as follows in equation 5.4:

$$D = \frac{k_B \cdot T}{6 \cdot \pi \cdot \eta \cdot a} \tag{5.4}$$

Where k_B, T, η, and, a are the Boltzmann constant, temperature, solution viscosity, and the hydrodynamic radius of the diffusing species respectively.

Therefore, decreasing peak current with increasing solvent viscosity, η, is the immediate consequence of peak current during CV being approximately proportional to $\eta^{-1/2}$ under the reasonable reversibility of the analytes herein (Figure 5-2).

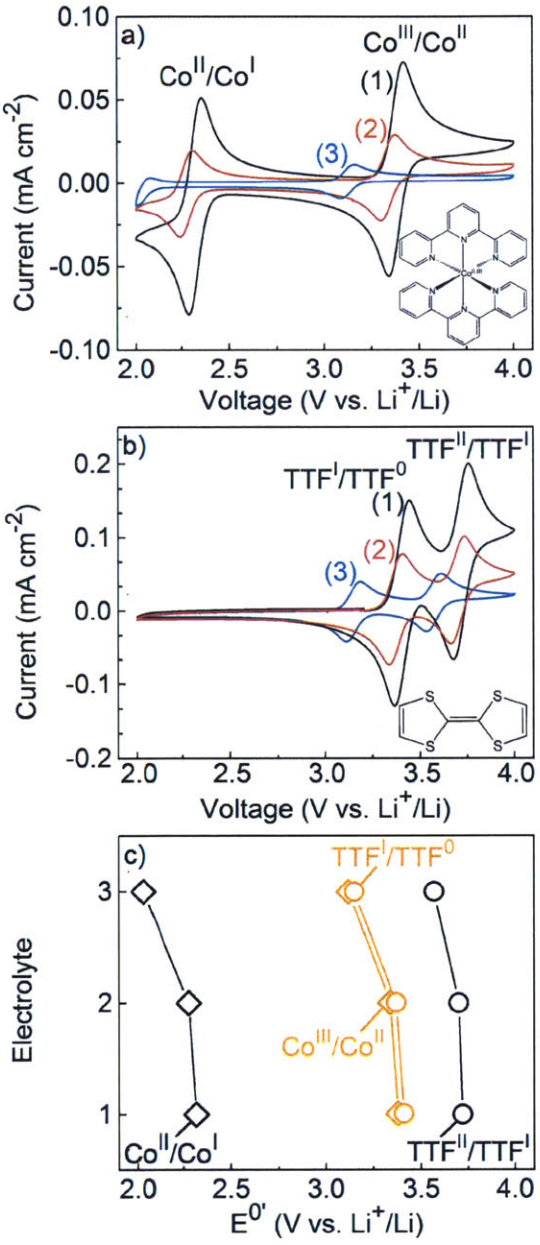

Figure 5-1. Voltammograms at 20 mV·s^{-1} using a glassy carbon electrode of 2 mM $Co^{II}(Terp)_2$ (a) and TTF (b): (1) 1 M LiTFSI in diglyme, (2) 1 M LiTFSI in $Pyr_{14}TFSI$:diglyme = 1:1 (volume ratio), and (3) 0.1 M LiTFSI in $Pyr_{14}TFSI$. (c) Reversible redox potential of mediators in respective electrolytes annotated with redox couples. Numbers on y-axis correspond to electrolyte formulation listed for (a) and (b).

More interestingly, the solvent produces a marked effect on the measured potentials of the Co^{III}/Co^{II}, Co^{II}/Co^{I}, TTF^{I}/TTF^{0}, and TTF^{II}/TTF^{I} as summarized in Figure 5-1c. Anodic to cathodic peaks separation for $Co(Terp)_2$ and TTF were found to vary between 66 and 80 mV (Table 5-1). These values are reasonably close to the 58 mV expected for a reversible one electron processes.[165] Variations in formal potentials could be due to (i) a shift in the absolute potential of the redox agent or/and (ii) a shift in the absolute potential of the Li^+/Li reference electrode. Changing the solvent produces similar shifts in the redox process of $Co(terp)_2$ and TTF (Figure 5-1), thus suggesting that the main cause of the shift is a variation of the potential of the lithium reference electrode.

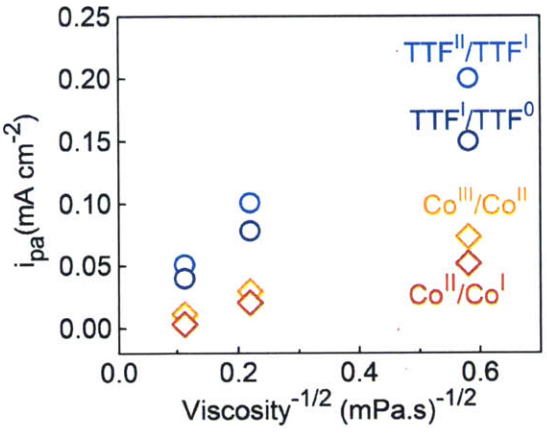

Figure 5-2. Values of anodic peak current per redox couple during CV at 20 $mV \cdot s^{-1}$. For both $Co(Terp)_2$ and TTF, anodic peaks for the two redox couples in each varies quasi-linearly with $\eta^{-1/2}$, increasing in value with decreasing η.

Indeed, very similar shifts in potential with solvents were observed in the voltammograms of the ferrocene/ferrocenium couple, which is often used as reference to compare between different solvents since ferrocene-based couples are known to interact

only weakly with solvents.[166] On the contrary, there is a strong interaction between the solvent and lithium cations, which affects the activity of lithium cations, and with this, the potential of the Li^+/Li reference electrode. Solvent-induced shifts in the potential of the lithium electrode versus the standard hydrogen electrode have been reported and are correlated to the strength of lithium solvation.[167] Solvation of lithium cations in diglyme containing electrolytes are stronger than in the ionic liquid $Pyr_{14}TFSI$; consequently, $E^{0'}(Li^+/Li)$ is lower in diglyme containing electrolytes, and as a result, the measured redox potential of $Co(Terp)_2$ and TTF measured vs. Li^+/Li decreases with the addition of more $Pyr_{14}TFSI$.

Table 5-1. Peak separation in mV for $Co(Terp)_2$ and TTF redox processes

Units (mV)	Co^{III}/Co^{II}	Co^{II}/Co^{I}	TTF^{II}/TTF^{I}	TTF^{I}/TTF^{0}
1 M LiTFSI in diglyme	78.5	65.8	79.6	76.9
1 M LiTFSI in $Pyr_{14}TFSI$:Diglyme	71.5	66.7	70.6	67.6
100 mM LiTFSI in $Pyr_{14}TFSI$	66.6	--	72.7	70.7

In order to mediate the oxidation of Li_2O_2, the standard potential of the metal complex *vs.* Li^+/Li should be higher than $E^0(O_2/Li_2O_2)$ = 2.96 V vs. Li^+/Li.[60] The range of potential of interest for $Co(Terp)_2$ and TTF are highlighted in orange in Figure 5-1c. The formal potential of Co^{III}/Co^{II} in $Co(Terp)_2$ were found to be 3.38, 3.34, and 3.12 V_{Li} in diglyme, $Pyr_{14}TFSI$:diglyme, and $Pyr_{14}TFSI$, respectively. Similarly, the formal potential

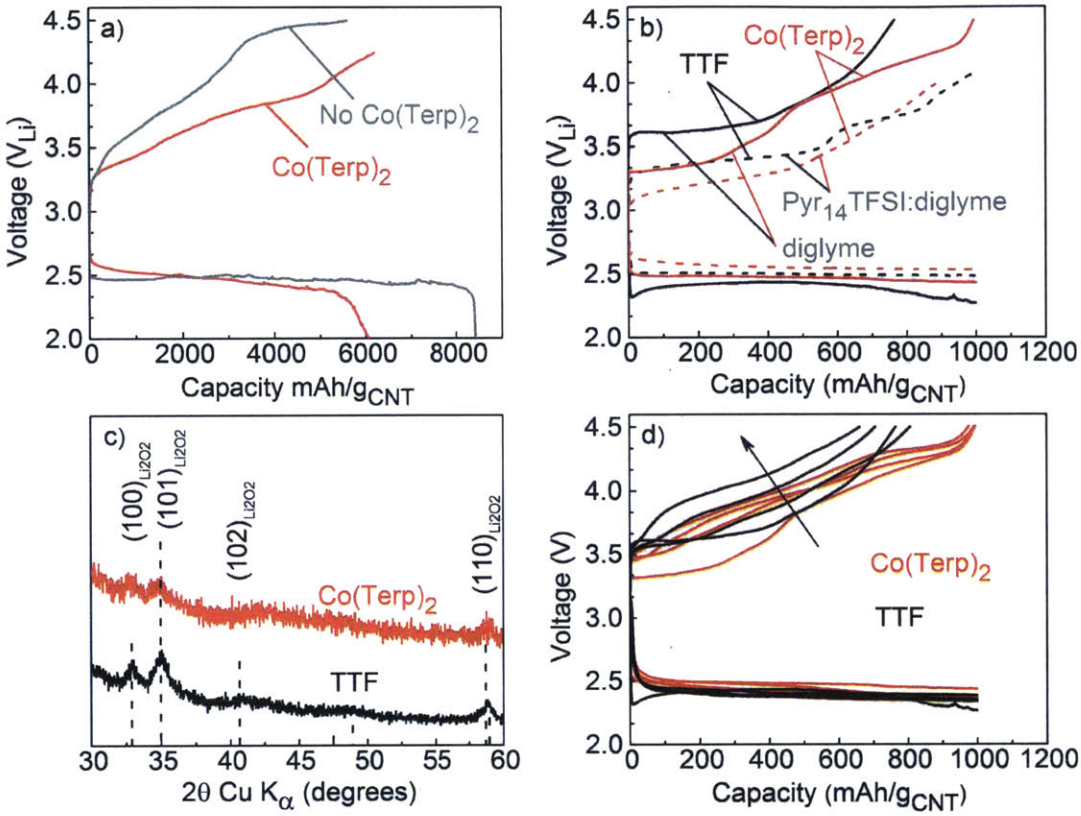

Figure 5-3. (a) Galvanostatic discharge (to 2.0 V_{Li}) and charge at 200 $mA \cdot g^{-1}_{CNT}$ of Li-O_2 cells in 1 M LiTFSI in Pyr_{14}TFSI:diglyme (1:1 volume ratio), with and without 50 mM $Co(Terp)_2$. (b) First cycle galvanostatic discharge and charge at 200 $mA \cdot g^{-1}_{CNT}$ of Li-O_2 cells using 1 M LiTFSI in diglyme (solid line) and Pyr_{14}TFSI:diglyme (dashed line) in presence of 50 mM $Co(Terp)_2$ or TTF. Capacities were limited to 1000 $mAh \cdot g^{-1}_{CNT}$. (c) XRD patterns of CNT electrodes after discharge in 1 M LiTFSI in diglyme with 50 mM $Co(Terp)_2$ and TTF. (d) Electrochemical discharge and charge during cycling under DEMS at 200 $mA \cdot g^{-1}_{CNT}$ of Li-O_2 cells in 1 M LiTFSI in diglyme in presence of 50 mM TTF or $Co(Terp)_2$. Cells discharge capacities were limited to 1000 $mAh \cdot g^{-1}_{CNT}$ and charging was limited to a 4.5 V_{Li} voltage cut-off. Arrow indicates the general direction of charge curves with increasing cycles.

of TTF^{I}/TTF^{0} were found to be 3.41, 3.37, and 3.15 V_{Li} in the same order of electrolyte solvents. Preliminary studies in unary $Pyr_{14}TFSI$ electrolyte showed only a minor effect of $Co(Terp)_2$ on the charge reaction likely because the potential (3.15 V_{Li}) was too close to the thermodynamic potential of Li_2O_2 oxidation (2.96 V_{Li}), and therefore, the driving force for the mediated Li_2O_2 oxidation (reaction 5.2 above) was small. Therefore, the following studies utilized diglyme and $Pyr_{14}TFSI$:diglyme.

Unlike TTF,[61, 168, 169] no prior report treats $Co(Terp)_2$ as a redox mediator in Li-O_2 batteries; therefore, we first probed the efficiency gain in $Pyr_{14}TFSI$:diglyme (with an intermediate formal potential of $Co(Terp)_2$ of 3.34 V_{Li}). Carpets of carbon nanotubes (CNT) served as the positive electrode and the first galvanostatic cycle at 200 $mA \cdot g^{-1}_{CNT}$ is reported in Figure 5-3a. No major effect of $Co(Terp)_2$ was resolved on the discharge to 2.0 V_{Li}. Although, the capacity of the CNT electrode in presence of $Co(Terp)_2$ appeared smaller than in its absence, capacity variations are common in different Li-O_2 cells. On charge, the average cell voltage with $Co(Terp)_2$ was ~3.8 V_{Li} versus ~4.1 V_{Li} without the mediator. This result indicates $Co(Terp)_2$ may have been enhancing cell charging per its intended use as a redox mediator.

We proceed to compare the electrochemical behavior at 200 $mA \cdot g^{-1}_{CNT}$ of $Co(Terp)_2$ and TTF in diglyme and $Pyr_{14}TFSI$:diglyme (Figure 5-3b). Once again, little influence of the mediators was observed on discharge. Also, no robust trend can be claimed regarding the discharge voltage profile from diglyme to $Pyr_{14}TFSI$:diglyme; the apparent higher discharge voltage with $Pyr_{14}TFSI$:diglyme compared to diglyme is likely within experimental error. Bergner et al.[110] similarly observed little influence of TEMPO on the discharge of Ketjen black carbon electrodes in diglyme. On charge, overpotentials seen

when using $Co(Terp)_2$ appeared to be consistently less than those of TTF in each solvent. This is in line with $E^{0'}(Co^{III}/Co^{II})$ being lower than $E^{0'}(TTF^{I}/TTF^{0})$ as seen in (Figure 5-1c). We also note that charging in the presence of the mediators also displayed lower potentials in $Pyr_{14}TFSI$:diglyme than in diglyme in agreement with the 20 to 40 mV reduction of $E^{0'}(Co^{III}/Co^{II})$ and $E^{0'}(TTF^{I}/TTF^{0})$ mentioned above. It is paramount to understand the actual chemistry associated with these electrochemical processes in Li-O_2 cells. Therefore, XRD and DEMS were performed to elucidate product formation and gas consumption and evolution.

Although better overall performance seems to occur in cells using $Pyr_{14}TFSI$:diglyme, we elected to investigate the chemical processes occurring in the presence of a redox mediator using the unary ether electrolyte commonly employed in Li-O_2 reports. Figure 5-3c shows the XRD of CNT electrodes discharged to a low cut-off of 2.0 V_{Li}. Formation of Li_2O_2 during discharge in the presence of TTF has been reported by Raman spectroscopy[61, 169] and electrochemical quartz crystal microbalance[168]. Similar to TTF, formation of Li_2O_2 as the discharge product is confirmed in the presence of $Co(Terp)_2$. This initial result suggests the presence of $Co(Terp)_2$ allows the main discharge reaction ($2Li^+ + 2e^- + O_2 \rightarrow Li_2O_2$) to proceed. DEMS results discussed below provide more details of the O_2 consumption in presence of these mediators.

In order to probe the chemical efficacy of $Co(Terp)_2$ and benchmark it against TTF, 2-compartment cells were cycled at 200 $mA \cdot g^{-1}_{CNT}$ for four cycles under DEMS using a 1 M LiTFSI diglyme electrolyte. Results of the cycling are summarized in Figure 5-3d. Similar to the observations on the first cycles mentioned above, the discharge profiles of $Co(Terp)_2$ during cycling in Figure 5-3d are close to that of TTF and match the ~2.5 V_{Li}

plateau characteristic of unmediated CNTs at 200 $mA \cdot g^{-1}_{CNT}$ (see Figure 5-3a). Electrochemical differences between $Co(Terp)_2$ and TTF, without regard to DEMS, were apparent mostly on charge. $Co(Terp)_2$ maintained lower charging voltages compared to TTF throughout cycling.

However, chemical probing of the efficacy of the reaction revealed considerable differences between the two mediators investigated. Figure 5-4 summarizes the measurements of O_2 consumption during discharge in presence of $Co(Terp)_2$ (panel a) and TTF (panel b) by monitoring the pressure decay of the O_2 atmosphere within the cell. Since formation of desired Li_2O_2 is a 2 e^-/O_2 reaction ($2Li^+ + 2e^- + O_2 \rightarrow Li_2O_2$), a close match between O_2 consumption and half of the faradaic current is expected. In the first cycle, less O_2 was consumed in the $Co(Terp)_2$ cell than expected from the half-current line (Figure 5-4a-1), especially at the beginning of discharge. Similar under-stoichiometric consumption of O_2 in cells with $Co(Terp)_2$ was noted for the subsequent three cycles (Figure 5-4a-2,3,4), where the number of electron per O_2 was found to be between 2.3 and 2.8 e^-/O_2 (Figure 5-5a). On the other hand, TTF displays a good match between the half-current and O_2 consumption on the first cycle (Figure 5-4b-1). The excess current as compared to O_2 consumed occurring during discharge with the addition of $Co^{II}(Terp)_2$ can be attributed to the reduction of Co^{II} to Co^{I} in the 50 mM $Co(Terp)_2$ used. A relatively small over-consumption of O_2 was observed at the beginning of discharge on the second through fourth cycles of TTF (Figure 5-4b-2,3,4) which might warrant further investigation (e^-/O_2 values between 1.9 and 2 recorded in Figure 5-5a).

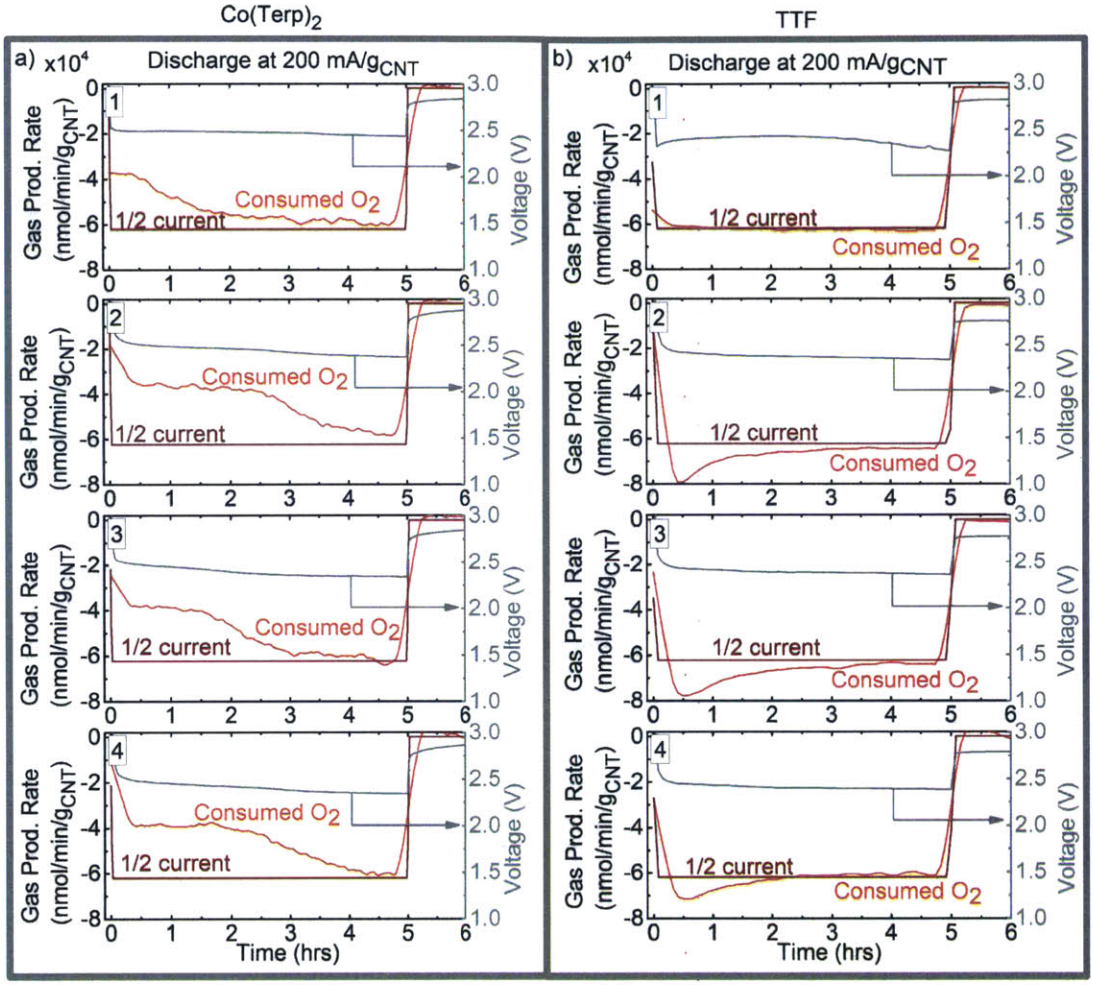

Figure 5-4. Galvanostatic discharge at 200 $mA \cdot g^{-1}_{CNT}$ of Li-O_2 cells in 1 M LiTFSI in diglyme in presence of 50 mM $Co(Terp)_2$ (a) and TTF (b). Cell discharges were limited to 1000 $mAh \cdot g^{-1}_{CNT}$. Panel numbering corresponds to cycle number for $Co(Terp)_2$ and TTF separately. Discharge voltage profiles are the same shown in Figure 5-3d.

We report the DEMS monitoring of gases evolved during galvanostatic charging, at 200 $mA \cdot g^{-1}_{CNT,}$ of Li-O_2 cells in the presence of $Co(Terp)_2$ and contrast with TTF in Figure 5-6. First, we note that no CO or H_2O was evident in DEMS spectra for all four

cycles of the two mediators investigated. O_2 evolution was observed in the early stages of charging at potentials as low as ~3.4 V_{Li} for $Co(Terp)_2$ and ~3.6 V_{Li} for TTF. These low onset voltages of O_2 evolution from Li_2O_2 oxidation show that these redox mediators can effectively reduce the overpotential required for Li_2O_2 oxidation in Li-O_2 batteries. Noticeably, when increasing voltages to ~4.0 V_{Li} and greater, CO_2 was found as the predominant gas evolved in presence of $Co(Terp)_2$ as well as TTF. A similar CO_2 evolution above 4.0 V_{Li} is reported using TEMPO[110] as mediator and can be assigned to decomposition of ether solvents at those potentials.[32, 170] This observation suggests that "galvanostatic charging followed by potentiostatic holding at voltages lower than 4.0 V_{Li}" of Li-O_2 cells with these redox mediators would be effective to oxidize Li_2O_2 with reduced potentials without triggering parasitic decomposition of electrolyte to CO_2. For both mediators, the amount of O_2 measured on charge was far below that consumed on discharge. The amount of O_2 evolved on charge in the presence of $Co(Terp)_2$ was between 10% and 23% of the O_2 consumed in the preceding discharge, OER/ORR, while in presence of TTF values between 10% to 32% were measured (Figure 5-5b). This OER/ORR was found to decay with cycle number, with TTF outperforming $Co(Terp)_2$ showing better round-trip O_2 recovery. Values of OER/ORR much lower than 100% indicate that a significant amount of the mediator oxidized on charge may be diffusing away from the CNT electrodes and thereby does not participate in the necessary reaction (2). A process which will cause incomplete removal of the Li_2O_2 deposit. Furthermore,

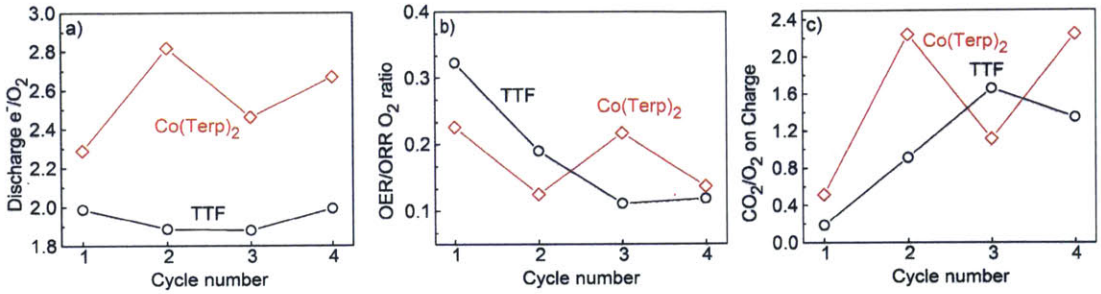

Figure 5-5. Summary of DEMS cycling at 200 $mA \cdot g^{-1}_{CNT}$ of Li-O_2 cells in 1 M LiTFSI in diglyme in presence of 50 mM $Co(Terp)_2$ and TTF. Cells discharge are limited to 1000 $mAh \cdot g^{-1}_{CNT}$. Charging voltages are limited to 4.5 V_{Li}. (a) Number of electrons per O_2 on discharge. (b) Ratio of O_2 evolved on charge to O_2 consumed on discharge. (c) Ratios of CO_2 to O_2 evolved on charge as a function of cycle number. For these calculations, cumulative values of species were obtained by integration of the rate curves shown in Figure 5-4 and Figure 5-6.

more CO_2 (at greater than ~4.0 V_{Li}) was measured relative to O_2 evolved in presence of $Co(Terp)_2$ compared to TTF in Figure 5-6. Figure 5-5c confirms this assessment with a generally larger CO_2/O_2 ratio in cells with $Co(Terp)_2$ versus TTF. In the case of TTF in Figure 5-6b, O_2 accompanies CO_2 evolution above 4.0 V_{Li}, while O_2 and CO_2 evolutions do not overlap in presence of $Co(Terp)_2$ (Figure 5-6a).

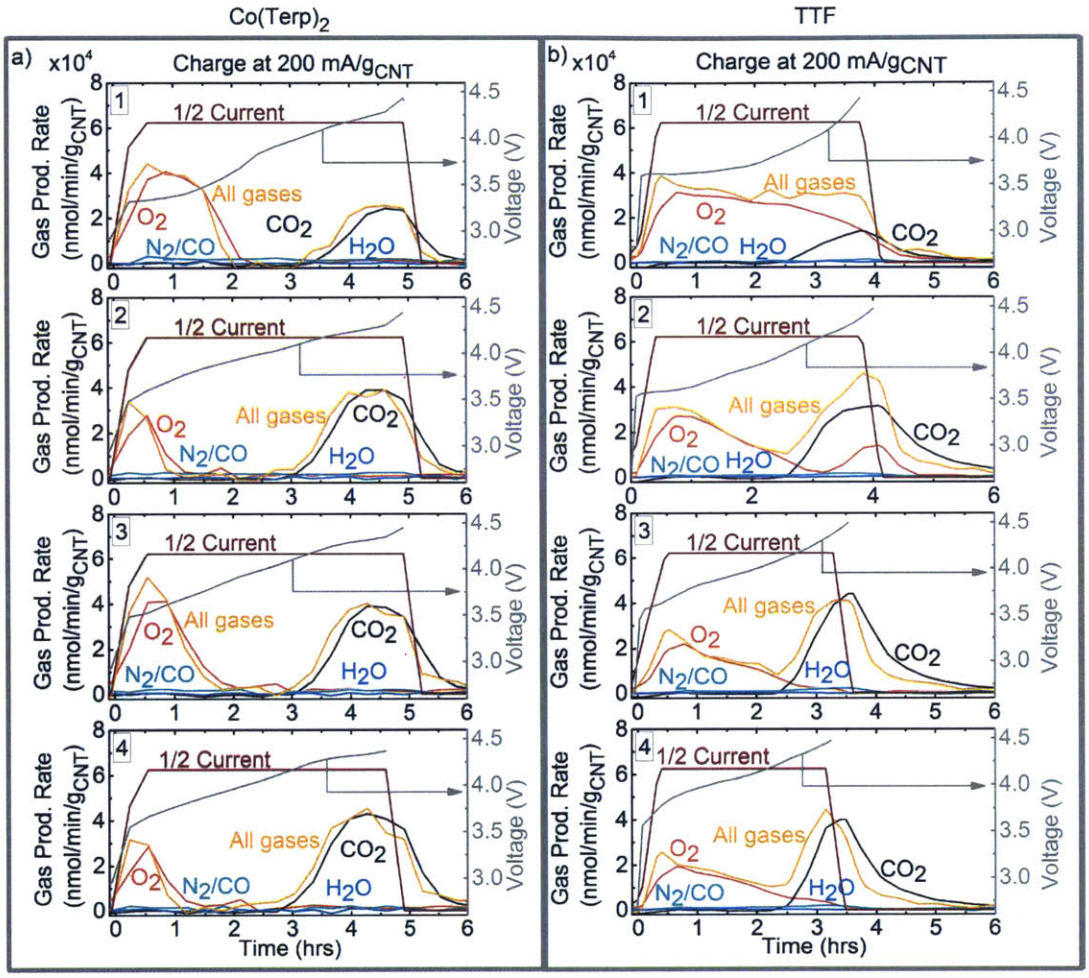

Figure 5-6. Galvanostatic charging at 200 $mA \cdot g^{-1}_{CNT}$ of Li-O_2 cells in 1 M LiTFSI in diglyme in presence of 50 mM $Co(Terp)_2$ (a) and TTF (b). Charging voltages were limited to 4.5 V_{Li}. Panel numbering correspond to cycle number for $Co(Terp)_2$ and TTF separately. Voltage profiles are the same shown in Figure 5-3d.

5.4. Conclusions

In this chapter, The effect of the tridendate cobalt bis(terpyridine) complex on the electrochemical performance of Li-O_2 cells was characterized by cyclic voltammetry and galvanostatic cycling, XRD and DEMS and benchmarked against TTF. It has been found

that the redox potential of redox mediators such as Co^{III}/Co^{II} and TTF^{I}/TTF^{0} redox couples measured vs. Li^{+}/Li decreases from unary diglyme to $Pyr_{14}TFSI$:diglyme to unary $Pyr_{14}TFSI$ due to weakening of Li^{+} solvation causing an upward shift of the Li^{+}/Li electrode potential. The change in redox potential is reflected in the value of the charging potential of Li-O_2 batteries, with lower charging voltages measured in $Pyr_{14}TFSI$:diglyme compared to diglyme in presence of either of the two mediators. The effect of $Co(Terp)_2$ has been compared to that of TTF, a well-known mediator of the Li_2O_2 oxidation in Li-O_2 cells.[14] Discharging in presence of $Co(Terp)_2$ resulted in undesired reduction of Co^{II} to Co^{I} at the 2.5 V_{Li} plateau of CNT electrodes, which resulted in non-ideal 2.3 to 2.8 e^{-}/O_2. On the other hand cells with TTF discharged close to ideal 2.0 e^{-}/O_2. Upon charging, although galvanic data showed faster charging kinetics with $Co(Terp)_2$, differential electrochemical mass spectrometry measurements reveal only partial O_2 recovery and significant CO_2 evolution above 4.0 V_{Li}. Similarly, partial O_2 recovery and CO_2 evolution occurred with TTF; however, the efficacy of TTF was found superior to the cobalt complex. In summary, the present detailed investigation of $Co(Terp)_2$ indicates it is not a suitable candidate for utilization as metal complex redox mediator for Li-O_2 batteries charging. Nonetheless, the systematic methodology here applied and the tuning of a mediator redox potential by choice of electrolyte solvent are important tools and approaches for future research in the field.

Chapter 6. Conclusions and Perspective

6.1. Summary

The Li-O_2 electrochemical system could offer energy storage at high energy density and low cost by replacing the heavy, relatively costly transition metals in the cathode of Li-Ion cells with lightweight, inexpensive oxygen. Its realization, however, is faced with interlinked degradation and high charging overpotentials. This thesis investigated avenues to enhance the rate of oxidation of Li_2O_2 for oxygen evolution (OER) during charging of Li-O_2 batteries. The overarching goal is been to identify solid-state as well as solute-state kinetic promoters for the Li_2O_2 oxidation reaction and understand their operating mechanism.

In Chapter 2, we elucidated upward to 50-fold higher Li_2O_2 oxidation current in presence chromium (oxide) nanoparticles. It is a fact that the excellent OER activity of chromium compounds in the Li-O_2 setting was counterintuitive in reference to their poor OER activity in aqueous media. We tentatively assigned this 'catalytic effect' to the facile Cr^{3+} to Cr^{6+} interexchange on the surface of all Cr oxides which chemically interacts with the Li_2O_2 during oxidation as measured by XPS and XAS. A preliminary mechanism was proposed that involves the formation of lithium-deficient LiO_2—Cr intermediates with faster oxidation kinetics.

In Chapter 3, we elaborate further on the operating pathway of solid-state promoters on the OER. Similarly to Cr, we measured an 80-fold increase in faradaic current for the Li_2O_2 oxidation reaction in presence of Mo compared to a baseline promoter-free carbon electrode. The facile oxidation of Mo which is the same group of the periodic table as Cr is again linked to the observed activity. Using XAS we elucidate unambiguously the formation of Li_2CrO_4 and Li_2MoO_4 on the surfaces of Cr and Mo in as charging

progresses. In the case of Cr, complete reversion/removal of the intermediate Li_2CrO_4 was measured at the end of charge. Examination of a large number of transition metals and metal oxides revealed a strong correlation between the enthalpy of chemical conversion of the promoter nanoparticle with Li_2O_2 towards formation of a lithium-rich metal oxide ($Li_2O_2 + M_aO_b \pm O_2 \rightarrow Li_xM_yO_z$) and the measured charging current. We propose thereby that the operating mechanism of solid-state promoters for the Li_2O_2 oxidation consists of a mix "chemical conversion to a lithium-rich metal oxide followed by electrochemical lithium deintercalation". Faster observed kinetics stems from the generally faster kinetics of deintercalation compared to the direct oxidation of insulating Li_2O_2.

We close our efforts to understand the mechanics of enhancement of the Li_2O_2 oxidation reaction by using DEMS to probe the gas consumption and evolution in Li-O_2 cells in presence of high activity promoters in Chapter 4. We found no influence of the promoter nanoparticle on discharge and measured close to the anticipated 2.0 e^-/O_2 in the $2Li^+ + 2e^- + O_2 \rightarrow Li_2O_2$ desired reaction. However, charging is sub-stoichiometric in terms of O_2 evolved per unit current whether in presence of Mo, Cr, and Ru or in a promoter-free Vulcan carbon electrode, in agreement with literature report thus far. More revealing was the trend of more severe sub-stoichiometry for Mo electrodes with ~4.2 e^-/O_2 on charge while Cr and Ru displayed ~2.7 e^-/O_2; this result is matched to the much larger conversion enthalpy to Li_2MoO_4 of Mo (-939 $kJ \cdot mol^{-1}$) while Cr and Ru have a comparable but lower conversion enthalpies (-440 $kJ \cdot mol^{-1}$) to Li_2CrO_4 and Li_2RuO_3, respectively. These DEMS results lend further support to the mechanism proposed for solid-state enhancement of the Li_2O_2 oxidation kinetic in Chapter 3.

Finally in Chapter 5, we explored the use of solute-state cobalt bis(terpyridine) metal complex ($Co(Terp)_2$) as a redox mediator for charging of Li-O_2 cells and benchmarked against tetrathiafulvalene (TTF). Progressively lowering the electrolyte solvent's Li^+ solvation energy from 100% diglyme to 50% diglyme with $Pyr_{14}TFSI$, to 100% $Pyr_{14}TFSI$, the formal potential of Co^{III}/Co^{II} and TTF^I/TTF^0 redox couples measured vs. Li^+/Li decreases as result of increasing Li^+/Li electrode potential. In diglyme electrolyte, both ($Co(Terp)_2$) and TTF showed little influence on discharge, while on charge a $Co(Terp)_2$ offered a lower charging voltage than TTF. However, using DEMS, $Co(Terp)_2$ showed a non-ideal 2.3 to 2.8 e^-/O_2 due to the undesired reduction of Co^{II} to Co^I at the 2.5 V_{Li} O_2 reduction plateau of CNT electrodes. This is in contrast to TTF which delivered approximately the ideal 2.0 e^-/O_2 on discharge. Upon charging, although electrochemical data showed faster charging kinetics with $Co(Terp)_2$ than TTF, DEMS measurements reveal only partial O_2 recovery and significant CO_2 evolution above 4.0 V_{Li} for both. Nonetheless, the efficacy of O_2 evolution by TTF was found superior to the cobalt complex. $Co(Terp)_2$ does not appear to be a suitable candidate for utilization as metal complex redox mediator for Li-O_2 batteries charging. Nonetheless, the systematic methodology here applied and the tuning of a mediator redox potential by choice of electrolyte solvent are important tools and approaches for future research in the field.

6.2. Perspective

Li_2O_2, the final discharge product of Li-O_2 batteries is proven to be a highly chemically reactive chemical species;[23, 24, 26, 30, 32, 53, 96, 136, 137] the intermediates of discharge and potentially charge such as singlet oxygen and LiO_2 are likely to be even more reactive.[151, 171] The investigations performed in the present thesis corroborate the fact with observed conversion of candidate promoters. An appropriate way forward in

optimizing the long term stability of Li-O_2 batteries in addition to efficiency resides in devising stable electrolytes and electrode components. Some progress in the electrode structures have been garnered in creating carbon-free electrodes such as such as nanoporous gold,[58] TiC,[21] and Ru on $TiSi_2$.[98]. Noting also that the stability of carbon is dependent on the carbon structure and surface functional groups,[24] surface functionalization of carbon could offer stable carbon-based electrodes.

Regarding electrolytes, the issue is been rather challenging as promising ethers and ionic liquid have failed to be stable for prolonged cycling. A recent advancement using a eutectic $LiNO_3$-KNO_3 molten salt electrolyte demonstrates the possibility of eliminating the unstable aprotic solvent.[172]

Furthermore, operation of the Li-O_2 cell in molten salt at the elevated temperature of 120 °C virtually eliminated the discharge to charge hysteresis with only a ~50 mV charging overpotential using a carbon electrode.[172] Albeit formation of Li_2CO_3 was observed by XRD during cycling, the first cycle offered the ideal 2.0 e^-/O_2 on discharge as well as charge which is usually not the case in the current state-of-the-art Li-O_2 cell discussed in Chapter 4. This molten salt electrolyte approach could be combined with progresses made in designing carbon-free and possibly promoter-free electrodes to achieve full cells with minimal electrolyte and electrode degradation. This approach offers one of the most promising path forward to stable, long cycle life, Li-O_2 cells.

In applying solid-state promoters in Li-O_2 batteries, the chemical participation of the metal nanoparticles surface called into question their long term stability. A research direction would be in identifying solid-state nanoparticles to reversibly undergo the process of chemical lithiation and electrochemical delithiation with high kinetics (such as Mo displayed on the first cycle) without irreversible surface transformation for the next cycles. Such a promoter, although changed in operando, will essentially maintain its starting chemical nature and undergo the same process on following cycle with similar efficacy. There are indications that Cr and Ru are such reversible promoters as shown in Chapter 3 and Chapter 4 and should be a good starting point for such as design and exploration work. Additionally, our microkinetics exploration of the proposed pathway of enhancement of Li_2O_2 oxidation revealed the need to extract other relevant kinetic

parameters of candidate promoters such as rate constant of the conversion to lithium metal oxide as well rate constant of the electrochemical delithiation.

Finally, in the area of redox mediators for Li-O_2 batteries, although our attempt at using cobalt bis(terpyridine) was unsuccessful, the intrinsic flexibility of the ligand in metal complexes offers avenues to tune properties such as formal redox potential and stability. We envision the possibility of ligand engineering on promising metal centers such as cobalt to potentially devise stable and electrochemically effective metal complex redox mediators for Li-O_2 batteries.

Several issues remain to be solved before the high gravimetric energy density and low-cost Li-O_2 cells can be used in grid storage, portable electronics, and long-range electric vehicles. The present thesis endeavored to advance understanding of the operating principles of solid-state and solute-state promoters. It is the hope of the author that the contributions herein will aid in the pursuit of practical Li-O_2 batteries.

References

1 B. Dunn, H. Kamath and J.-M. Tarascon, Electrical Energy Storage for the Grid: A Battery of Choices, *Science*, 2011, **334**, 928.

2 T. F. Stocker, D. Qin, G.-K. Plattner, M. M. B. Tignor, S. K. Allen, J. Boschung, A. Nauels, Y. Xia, V. Bex and P. M. Midgley, IPCC, Cambridge University Press, Cambridge, United Kingdom and New York, NY, USA, 2013, p. 1535.

3 E. Dlugokencky and P. Tans, www.esrl.noaa.gov/gmd/ccgg/trends/, Accessed March 18, 2016, 2016.

4 W. Peters, A. R. Jacobson, C. Sweeney, A. E. Andrews, T. J. Conway, K. Masarie, J. B. Miller, L. M. P. Bruhwiler, G. Pétron, A. I. Hirsch, D. E. J. Worthy, G. R. van der Werf, J. T. Randerson, P. O. Wennberg, M. C. Krol and P. P. Tans, An atmospheric perspective on North American carbon dioxide exchange: CarbonTracker, *P. Natl. Acad. Sci.*, 2007, **104**, 18925.

5 World Bank Group, http://databank.worldbank.org/data/home.aspx, Accessed March 17, 2016, 2016.

6 EPA, Inventory of U.S. Greenhouse Gas Emissions and Sinks: 1990–2013, 2015.

7 NREL, 2013 Renewable Energy Data Book, 2013.

8 EIA, What is U.S. electricity generation by energy source?, http://www.eia.gov/, Accessed March 17, 2016, 2016.

9 NERC, http://www.nerc.com/Pages/default.aspx, Accessed March 20, 2016, 2016.

10 C. R. Ferguson and A. T. Kirkpatrick, *Internal Combustion Engines: Applied Thermosciences*, John Wiley and Sons Ltd, United Kingdom, 2016.

11 H. Chen, T. N. Cong, W. Yang, C. Tan, Y. Li and Y. Ding, Progress in electrical energy storage system: A critical review, *Prog. Nat. Sci.*, 2009, **19**, 291.

12 P. Vanysek, in *CRC Handbook of Chemistry and Physics*, ed. D. R. Lide, CRC Press: Boca Raton, 2002, pp. 8-21–8-31.

13 H. Tian, F. Xin, X. Wang, W. He and W. Han, High capacity group-IV elements (Si, Ge, Sn) based anodes for lithium-ion batteries, *J. Materiomics*, 2015, **1**, 153.

14 P. G. Bruce, S. A. Freunberger, L. J. Hardwick and J. M. Tarascon, Li-O_2 and Li-S batteries with high energy storage, *Nat. Mater.*, 2012, **11**, 19.

15 L. F. Nazar, M. Cuisinier and Q. Pang, Lithium-sulfur batteries, *MRS Bull.*, 2014, **39**, 436.

16 K. G. Gallagher, S. Goebel, T. Greszler, M. Mathias, W. Oelerich, D. Eroglu and V. Srinivasan, Quantifying the promise of lithium-air batteries for electric vehicles, *Energy Environ. Sci.*, 2014, **7**, 1555.

17 Y.-C. Lu, H. A. Gasteiger, M. C. Parent, V. Chiloyan and Y. Shao-Horn, The Influence of Catalysts on Discharge and Charge Voltages of Rechargeable Li–Oxygen Batteries, *Electrochem. Solid-State Lett.*, 2010, **13**, A69.

18 Y.-C. Lu, B. M. Gallant, D. G. Kwabi, J. R. Harding, R. R. Mitchell, M. S. Whittingham and Y. Shao-Horn, Lithium-oxygen batteries: bridging mechanistic understanding and battery performance, *Energy Environ. Sci.*, 2013, **6**, 750.

19 USCAR, Energy Storage System Goals, http://www.uscar.org, Accessed Jan. 01, 2016, 2016.

20 S. W. Lee, B. M. Gallant, H. R. Byon, P. T. Hammond and Y. Shao-Horn, Nanostructured carbon-based electrodes: bridging the gap between thin-film lithium-ion batteries and electrochemical capacitors, *Energy Environ. Sci.*, 2011, **4**, 1972.

21 M. M. Ottakam Thotiyl, S. A. Freunberger, Z. Peng, Y. Chen, Z. Liu and P. G. Bruce, A stable cathode for the aprotic Li–O_2 battery, *Nat. Mater.*, 2013, **12**, 1050.

22 B. M. Gallant, R. R. Mitchell, D. G. Kwabi, J. Zhou, L. Zuin, C. V. Thompson and Y. Shao-Horn, Chemical and Morphological Changes of Li–O_2 Battery Electrodes upon Cycling, *J. Phys. Chem. C*, 2012, **116**, 20800.

23 B. D. McCloskey, A. Speidel, R. Scheffler, D. C. Miller, V. Viswanathan, J. S. Hummelshøj, J. K. Nørskov and A. C. Luntz, Twin Problems of Interfacial Carbonate Formation in Nonaqueous Li–O_2 Batteries, *J. Phys. Chem. Lett.*, 2012, **3**, 997.

24 M. M. Ottakam Thotiyl, S. A. Freunberger, Z. Peng and P. G. Bruce, The carbon electrode in nonaqueous Li-O_2 cells, *J. Am. Chem. Soc.*, 2013, **135**, 494.

25 Y. Shao, S. Park, J. Xiao, J.-G. Zhang, Y. Wang and J. Liu, Electrocatalysts for Nonaqueous Lithium–Air Batteries: Status, Challenges, and Perspective, *ACS Catal.*, 2012, **2**, 844.

26 S. A. Freunberger, Y. Chen, Z. Peng, J. M. Griffin, L. J. Hardwick, F. Barde, P. Novak and P. G. Bruce, Reactions in the rechargeable lithium-O_2 battery with alkyl carbonate electrolytes, *J. Am. Chem. Soc.*, 2011, **133**, 8040.

27 M. E. Ortiz, L. J. Núñez-Vergara and J. A. Squella, Voltammetric determination of the heterogeneous charge transfer rate constant for superoxide formation at a glassy carbon electrode in aprotic medium, *J. Electroanal. Chem.*, 2003, **549**, 157.

28 E. I. Rogers, X.-J. Huang, E. J. F. Dickinson, C. Hardacre and R. G. Compton, Investigating the Mechanism and Electrode Kinetics of the Oxygen|Superoxide ($O_2|O_2^{\bullet-}$) Couple in Various Room-Temperature Ionic Liquids at Gold and Platinum Electrodes in the Temperature Range 298–318 K, *J. Phys. Chem. C*, 2009, **113**, 17811.

29 V. S. Bryantsev and F. Faglioni, Predicting autoxidation stability of ether- and amide-based electrolyte solvents for Li-air batteries, *J. Phys. Chem. A*, 2012, **116**, 7128.

30 B. D. McCloskey, D. S. Bethune, R. M. Shelby, G. Girishkumar and A. C. Luntz, Solvents' Critical Role in Nonaqueous Lithium–Oxygen Battery Electrochemistry, *J. Phys. Chem. Lett.*, 2011, **2**, 1161.

31 D. Aurbach, M. Daroux, P. Faguy and E. Yeager, The electrochemistry of noble metal electrodes in aprotic organic solvents containing lithium salts, *J. Electroanal. Chem. Interfacial Electrochem.*, 1991, **297**, 225.

32 S. A. Freunberger, Y. Chen, N. E. Drewett, L. J. Hardwick, F. Barde and P. G. Bruce, The lithium-oxygen battery with ether-based electrolytes, *Angew. Chem. Int. Ed.*, 2011, **50**, 8609.

33 C. Laoire, S. Mukerjee, E. J. Plichta, M. A. Hendrickson and K. M. Abraham, Rechargeable Lithium/TEGDME- LiPF6/O_2 Battery, *J. Electrochem. Soc.*, 2011, **158**, A302.

34 R. Black, S. H. Oh, J. H. Lee, T. Yim, B. Adams and L. F. Nazar, Screening for superoxide reactivity in Li-O_2 batteries: effect on Li_2O_2/LiOH crystallization, *J. Am. Chem. Soc.*, 2012, **134**, 2902.

35 K. P. C. Yao, D. G. Kwabi, R. A. Quinlan, A. N. Mansour, A. Grimaud, Y.-L. Lee, Y.-C. Lu and Y. Shao-Horn, Thermal Stability of Li_2O_2 and Li_2O for Li-Air Batteries: In Situ XRD and XPS Studies, *J. Electrochem. Soc.*, 2013, **160**, A824.

36 L. G. Cota and P. de la Mora, On the structure of lithium peroxide, Li_2O_2, *Acta Crystallogr. B*, 2005, **61**, 133.

37 J. S. Hummelshøj, J. Blomqvist, S. Datta, T. Vegge, J. Rossmeisl, K. S. Thygesen, A. C. Luntz, K. W. Jacobsen and J. K. Nørskov, Communications: Elementary oxygen electrode reactions in the aprotic Li-air battery, *J. Chem. Phys.*, 2010, **132**, 071101.

38 P. Albertus, G. Girishkumar, B. McCloskey, R. S. Sánchez-Carrera, B. Kozinsky, J. Christensen and A. C. Luntz, Identifying Capacity Limitations in the Li/Oxygen Battery Using Experiments and Modeling, *J. Electrochem. Soc.*, 2011, **158**, A343.

39 M. D. Radin, J. F. Rodriguez, F. Tian and D. J. Siegel, Lithium peroxide surfaces are metallic, while lithium oxide surfaces are not, *J. Am. Chem. Soc.*, 2012, **134**, 1093.

40 O. Gerbig, R. Merkle and J. Maier, Electron and Ion Transport In Li_2O_2, 2013, **25**, 3129.

41 R. Black, J. H. Lee, B. Adams, C. A. Mims and L. F. Nazar, The role of catalysts and peroxide oxidation in lithium-oxygen batteries, *Angew. Chem. Int. Ed.*, 2013, **52**, 392.

42 B. M. Gallant, D. G. Kwabi, R. R. Mitchell, J. Zhou, C. V. Thompson and Y. Shao-Horn, Influence of Li_2O_2 morphology on oxygen reduction and evolution kinetics in Li-O_2 batteries, *Energy Environ. Sci.*, 2013, **6**, 2518.

43 S. Kang, Y. Mo, S. P. Ong and G. Ceder, A Facile Mechanism for Recharging Li_2O_2 in Li–O_2 Batteries, *Chem. Mater.*, 2013, **25**, 3328.

44 Y. Mo, S. P. Ong and G. Ceder, First-principles study of the oxygen evolution reaction of lithium peroxide in the lithium-air battery, *Phys. Rev. B*, 2011, **84**, 205446.

45 Y.-C. Lu, D. G. Kwabi, K. P. C. Yao, J. R. Harding, J. Zhou, L. Zuin and Y. Shao-Horn, The discharge rate capability of rechargeable Li-O_2 batteries, *Energy Environ. Sci.*, 2011, **4**, 2999.

46 K. U. Schwenke, S. Meini, X. Wu, H. A. Gasteiger and M. Piana, Stability of superoxide radicals in glyme solvents for non-aqueous Li-O_2 battery electrolytes, *Phys. Chem. Chem. Phys.*, 2013, **15**, 11830.

47 V. S. Bryantsev, V. Giordani, W. Walker, M. Blanco, S. Zecevic, K. Sasaki, J. Uddin, D. Addison and G. V. Chase, Predicting solvent stability in aprotic electrolyte Li-air batteries: nucleophilic substitution by the superoxide anion radical ($O_2^{\bullet-}$), *J. Phys. Chem. A*, 2011, **115**, 12399.

48 D. Sharon, V. Etacheri, A. Garsuch, M. Afri, A. A. Frimer and D. Aurbach, On the Challenge of Electrolyte Solutions for Li–Air Batteries: Monitoring Oxygen Reduction and Related Reactions in Polyether Solutions by Spectroscopy and EQCM, *J. Phys. Chem. Lett.*, 2012, **4**, 127.

49 Y. C. Lu and Y. Shao-Horn, Probing the Reaction Kinetics of the Charge Reactions of Nonaqueous Li-O2 Batteries, *J. Phys. Chem. Lett.*, 2013, **4**, 93.

50 J. S. Hummelshøj, A. C. Luntz and J. K. Nørskov, Theoretical evidence for low kinetic overpotentials in Li-O_2 electrochemistry, *J. Chem. Phys.*, 2013, **138**, 034703.

51 Y.-C. Lu and Y. Shao-Horn, Probing the Reaction Kinetics of the Charge Reactions of Nonaqueous Li–O_2 Batteries, *J. Phys. Chem. Lett.*, 2013, **4**, 93.

52 V. Viswanathan, K. S. Thygesen, J. S. Hummelshoj, J. K. Norskov, G. Girishkumar, B. D. McCloskey and A. C. Luntz, Electrical conductivity in Li_2O_2 and its role in determining capacity limitations in non-aqueous Li-O_2 batteries, *J. Chem. Phys.*, 2011, **135**, 214704.

53 B. D. McCloskey, R. Scheffler, A. Speidel, D. S. Bethune, R. M. Shelby and A. C. Luntz, On the efficacy of electrocatalysis in nonaqueous Li-O_2 batteries, *J. Am. Chem. Soc.*, 2011, **133**, 18038.

54 S. H. Oh and L. F. Nazar, Oxide Catalysts for Rechargeable High-Capacity Li–O_2 Batteries, *Adv. Energy Mater.*, 2012, **2**, 903.

55 J.-H. Lee, R. Black, G. Popov, E. Pomerantseva, F. Nan, G. A. Botton and L. F. Nazar, The role of vacancies and defects in $Na_{0.44}MnO_2$ nanowire catalysts for lithium-oxygen batteries, *Energy Environ. Sci.*, 2012, **5**, 9558.

56 R. R. Mitchell, B. M. Gallant, C. V. Thompson and Y. Shao-Horn, All-carbon-nanofiber electrodes for high-energy rechargeable Li-O_2 batteries, *Energy Environ. Sci.*, 2011, **4**, 2952.

57 Y. Chen, S. A. Freunberger, Z. Peng, F. Bardé and P. G. Bruce, Li–O_2 Battery with a Dimethylformamide Electrolyte, *J. Am. Chem. Soc.*, 2012, **134**, 7952.

58 Z. Peng, S. A. Freunberger, Y. Chen and P. G. Bruce, A reversible and higher-rate Li-O_2 battery, *Science*, 2012, **337**, 563.

59 L. Brandsma, J. Meijer and H. D. Verkruijsse, Cleavage of dimethyl sulfoxide by alkali metals, *Recueil des Travaux Chimiques des Pays-Bas*, 1976, **95**, 79.

60 G. V. Chase, S. Zecevic, T. W. Wesley, J. Uddin, K. A. Sasaki, P. G. Vincent, V. Bryantsev, M. Blanco and D. D. Addison, Soluble oxygen evolving catalysts for rechargeable metal-air batteries, *USPTO*, US20120028137 A1, 2012

61 Y. H. Chen, S. A. Freunberger, Z. Q. Peng, O. Fontaine and P. G. Bruce, Charging a Li–O_2 battery using a redox mediator, *Nat. Chem.*, 2013, **5**, 489.

62 J. R. Harding, Y. C. Lu, Y. Tsukada and Y. Shao-Horn, Evidence of catalyzed oxidation of Li_2O_2 for rechargeable Li-air battery applications, *Phys. Chem. Chem. Phys.*, 2012, **14**, 10540.

63 Y. Yang, M. Shi, Y.-S. Li and Z.-W. Fu, MnO_2-Graphene Composite Air Electrode for Rechargeable Li-Air Batteries, *J. Electrochem. Soc.*, 2012, **159**, A1917.

64 V. Giordani, S. A. Freunberger, P. G. Bruce, J. M. Tarascon and D. Larcher, H_2O_2 Decomposition Reaction as Selecting Tool for Catalysts in Li-O_2 Cells, *Electrochem. Solid-State Lett.*, 2010, **13**, A180.

65 K.-N. Jung, J.-I. Lee, W. B. Im, S. Yoon, K.-H. Shin and J.-W. Lee, Promoting Li_2O_2 oxidation by an $La_{1.7}Ca_{0.3}Ni_{0.75}Cu_{0.25}O_4$ layered perovskite in lithium-oxygen batteries, *Chem. Commun.*, 2012, **48**, 9406.

66 S. H. Oh, R. Black, E. Pomerantseva, J.-H. Lee and L. F. Nazar, Synthesis of a metallic mesoporous pyrochlore as a catalyst for lithium-O_2 batteries, *Nat. Chem.*, 2012, **4**, 1004.

67 I. C. Man, H.-Y. Su, F. Calle-Vallejo, H. A. Hansen, J. I. Martínez, N. G. Inoglu, J. Kitchin, T. F. Jaramillo, J. K. Nørskov and J. Rossmeisl, Universality in Oxygen Evolution Electrocatalysis on Oxide Surfaces, *ChemCatChem*, 2011, **3**, 1159.

68 J. Suntivich, H. A. Gasteiger, N. Yabuuchi, H. Nakanishi, J. B. Goodenough and Y. Shao-Horn, Design principles for oxygen-reduction activity on perovskite oxide catalysts for fuel cells and metal-air batteries, *Nat. Chem.*, 2011, **3**, 546.

69 J. Suntivich, K. J. May, H. A. Gasteiger, J. B. Goodenough and Y. Shao-Horn, A perovskite oxide optimized for oxygen evolution catalysis from molecular orbital principles, *Science*, 2011, **334**, 1383.

70 S. Dahl, A. Logadottir, C. J. H. Jacobsen and J. K. Nørskov, Electronic factors in catalysis: the volcano curve and the effect of promotion in catalytic ammonia synthesis, *Appl. Catal. A-Gen.*, 2001, **222**, 19.

71 M. Jaksic, Volcano plots along the Periodic table, their causes and consequences on electrocatalysis for hydrogen electrode reactions, *J. New Mat. Elect. Syst.*, 2000, **3**, 153.

72 F. H. B. Lima, J. Zhang, M. H. Shao, K. Sasaki, M. B. Vukmirovic, E. A. Ticianelli and R. R. Adzic, Catalytic Activity-d-Band Center Correlation for the O_2 Reduction Reaction on Platinum in Alkaline Solutions, *J.Phys. Chem. C*, 2007, **111**, 404.

73 J. K. Nørskov, F. Abild-Pedersen, F. Studt and T. Bligaard, Density functional theory in surface chemistry and catalysis, *P. Natl. Acad. Sci. USA*, 2011, **108**, 937.

74 J. Suntivich, H. A. Gasteiger, N. Yabuuchi and Y. Shao-Horn, Electrocatalytic Measurement Methodology of Oxide Catalysts Using a Thin-Film Rotating Disk Electrode, *J. Electrochem. Soc.*, 2010, **157**, B1263.

75 C. A. Schneider, W. S. Rasband and K. W. Eliceiri, NIH Image to ImageJ: 25 years of image analysis, *Nat. Meth.*, 2012, **9**, 671.

76 Y.-C. Lu, H. A. Gasteiger and Y. Shao-Horn, Catalytic Activity Trends of Oxygen Reduction Reaction for Nonaqueous Li-Air Batteries, *J. Am. Chem. Soc.*, 2011, **133**, 19048

77 T. Regier, J. Krochak, T. K. Sham, Y. F. Hu, J. Thompson and R. I. R. Blyth, Performance and capabilities of the Canadian Dragon: The SGM beamline at the Canadian Light Source, *Nucl. Instrum. Meth. A*, 2007, **582**, 93.

78 K. P. C. Yao, Y.-C. Lu, C. V. Amanchukwu, D. G. Kwabi, M. Risch, J. Zhou, A. Grimaud, P. T. Hammond, F. Barde and Y. Shao-Horn, The influence of transition metal oxides on the kinetics of Li_2O_2 oxidation in Li-O_2 batteries: high activity of chromium oxides, *Phys. Chem. Chem. Phys.*, 2014, **16**, 2297.

79 T. Shinagawa, A. T. Garcia-Esparza and K. Takanabe, Insight on Tafel slopes from a microkinetic analysis of aqueous electrocatalysis for energy conversion, *Sci. Rep.*, 2015, **5**, 13801.

80 V. Viswanathan, J. K. Nørskov, A. Speidel, R. Scheffler, S. Gowda and A. C. Luntz, Li–O_2 Kinetic Overpotentials: Tafel Plots from Experiment and First-Principles Theory, *J. Phys. Chem. Lett.*, 2013, **4**, 556.

81 M. D. Radin, F. Tian and D. J. Siegel, Electronic structure of Li_2O_2 {0001} surfaces, *J. Mater. Sci.*, 2012, **47**, 7564.

82 T. Schedel-Niedrig, X-Ray absorption spectroscopy: sensitive characterization of (model-) catalysts with the electron yield technique, *Fresenius J. Anal. Chem.*, 1998, **361**, 680.

83 M. O. Figueiredo, A. C. dos Santos, M. J. Carmezim, M. Abbate, F. M. F. de Groot, H. Petersen and W. Braun, Chemical study of passivating chromium oxide films by soft X-ray absorption spectroscopy, *Analyst*, 1994, **119**, 609.

84 F. M. F. de Groot, M. Grioni, J. C. Fuggle, J. Ghijsen, G. A. Sawatzky and H. Petersen, Oxygen 1s X-ray-absorption edges of transition-metal oxides, *Phys. Rev. B*, 1989, **40**, 5715.

85 R. Qiao, Y.-D. Chuang, S. Yan and W. Yang, Soft X-Ray Irradiation Effects of Li_2O_2, Li_2CO_3 and Li_2O Revealed by Absorption Spectroscopy, *PLoS ONE*, 2012, **7**, e49182.

86 M. W. Ruckman, J. Chen, S. L. Qiu, P. Kuiper, M. Strongin and B. I. Dunlap, Interpreting the near edges of O_2 and O_2^- in alkali-metal superoxides, *Phys. Rev. Lett.*, 1991, **67**, 2533.

87 D. W. Fischer, Soft x-ray band spectra and molecular orbital structure of Cr_2O_3, CrO_3, CrO_4^{-2} and $Cr_2O_7^{-2}$, *J. Phys. Chem. Solids*, 1971, **32**, 2455.

88 J. Stöhr, *NEXAFS Spectroscopy*, Springer, Berlin, 2003.

89 T. L. Daulton and B. J. Little, Determination of chromium valence over the range Cr(0)–Cr(VI) by electron energy loss spectroscopy, *Ultramicroscopy*, 2006, **106**, 561.

90 L. Zhong, R. R. Mitchell, Y. Liu, B. M. Gallant, C. V. Thompson, J. Y. Huang, S. X. Mao and Y. Shao-Horn, In Situ Transmission Electron Microscopy Observations of Electrochemical Oxidation of Li_2O_2, *Nano Lett.*, 2013, **13**, 2209.

91 B. D. McCloskey, R. Scheffler, A. Speidel, D. S. Bethune, R. M. Shelby and A. C. Luntz, On the Efficacy of Electrocatalysis in Nonaqueous Li-O_2 Batteries, *J. Am. Chem. Soc.*, 2011, **133**, 18038.

92 B. D. McCloskey, R. Scheffler, A. Speidel, G. Girishkumar and A. C. Luntz, On the Mechanism of Nonaqueous Li-O_2 Electrochemistry on C and Its Kinetic Overpotentials: Some Implications for Li-Air Batteries, *J. Phys. Chem. C*, 2012, **116**, 23897.

93 S. Ganapathy, B. D. Adams, G. Stenou, M. S. Anastasaki, K. Goubitz, X.-F. Miao, L. F. Nazar and M. Wagemaker, The nature of Li_2O_2 oxidation in a Li-O_2 battery revealed by operando X-ray diffraction, *J. Am. Chem. Soc.*, 2014, **136**, 16335.

94 F. Li, R. Ohnishi, Y. Yamada, J. Kubota, K. Domen, A. Yamada and H. Zhou, Carbon supported TiN nanoparticles: an efficient bifunctional catalyst for non-aqueous Li-O_2 batteries, *Chem. Commun.*, 2013, **49**, 1175.

95 Y. Cao, S.-R. Cai, S.-C. Fan, W.-Q. Hu, M.-S. Zheng and Q.-F. Dong, Reduced graphene oxide anchoring $CoFe_2O_4$ nanoparticles as an effective catalyst for non-aqueous lithium-oxygen batteries, *Faraday Discuss.*, 2014, **172**, 215.

96 B. D. McCloskey, J. M. Garcia and A. C. Luntz, Chemical and Electrochemical Differences in Nonaqueous Li-O_2 and Na-O_2 Batteries, *J. Phys. Chem. Lett.*, 2014, **5**, 1230.

97 T. Cetinkaya, S. Ozcan, M. Uysal, M. O. Guler and H. Akbulut, Free-standing flexible graphene oxide paper electrode for rechargeable Li-O_2 batteries, *J. Power Sources*, 2014, **267**, 140.

98 J. Xie, X. Yao, I. P. Madden, D.-E. Jiang, L.-Y. Chou, C.-K. Tsung and D. Wang, Selective Deposition of Ru Nanoparticles on $TiSi_2$ Nanonet and Its Utilization for Li_2O_2 Formation and Decomposition, *J. Am. Chem. Soc.*, 2014, **136**, 8903.

99 Z. Jian, P. Liu, F. Li, P. He, X. Guo, M. Chen and H. Zhou, Core–Shell-Structured CNT@RuO_2 Composite as a High-Performance Cathode Catalyst for Rechargeable Li-O_2 Batteries, *Angew. Chem. Int. Ed.*, 2014, **53**, 442.

100 F. Li, Y. Chen, D.-M. Tang, Z. Jian, C. Liu, D. Golberg, A. Yamada and H. Zhou, Performance-improved Li-O_2 battery with Ru nanoparticles supported on binder-free multi-walled carbon nanotube paper as cathode, *Energy Environ. Sci.*, 2014, **7**, 1648.

101 C. Kavakli, S. Meini, G. Harzer, N. Tsiouvaras, M. Piana, A. Siebel, A. Garsuch, H. A. Gasteiger and J. Herranz, Nanosized Carbon-Supported Manganese Oxide Phases as Lithium-Oxygen Battery Cathode Catalysts, *ChemCatChem*, 2013, **5**, 3358.

102 K. Song, J. Jung, Y.-U. Heo, Y. C. Lee, K. Cho and Y.-M. Kang, α-MnO_2 nanowire catalysts with ultra-high capacity and extremely low overpotential in lithium-air batteries through tailored surface arrangement, *Phys. Chem. Chem. Phys.*, 2013, **15**, 20075.

103 J. Ming, W. J. Kwak, J. B. Park, C. D. Shin, J. Lu, L. Curtiss, K. Amine and Y. K. Sun, A physical pulverization strategy for preparing a highly active composite of CoO_x and crushed graphite for lithium-oxygen batteries, *Chemphyschem*, 2014, **15**, 2070.

104 B. G. Kim, H.-J. Kim, S. Back, K. W. Nam, Y. Jung, Y.-K. Han and J. W. Choi, Improved reversibility in lithium-oxygen battery: Understanding elementary reactions and surface charge engineering of metal alloy catalyst, *Sci. Rep.*, 2014, **4**, 4225.

105 R. Cao, E. D. Walter, W. Xu, E. N. Nasybulin, P. Bhattacharya, M. E. Bowden, M. H. Engelhard and J.-G. Zhang, The Mechanisms of Oxygen Reduction and Evolution Reactions in Nonaqueous Lithium–Oxygen Batteries, *ChemSusChem*, 2014, **7**, 2436.

106 Z. Peng, S. A. Freunberger, L. J. Hardwick, Y. Chen, V. Giordani, F. Bardé, P. Novák, D. Graham, J.-M. Tarascon and P. G. Bruce, Oxygen Reactions in a Non-Aqueous Li^+ Electrolyte, *Angew. Chem. Int. Ed.*, 2011, **50**, 6351.

107 M. J. Trahan, I. Gunasekara, S. Mukerjee, E. J. Plichta, M. A. Hendrickson and K. M. Abraham, Solvent-Coupled Catalysis of the Oxygen Electrode Reactions in Lithium-Air Batteries, *J. Electrochem. Soc.*, 2014, **161**, A1706.

108 M. J. Trahan, S. Mukerjee, E. J. Plichta, M. A. Hendrickson and K. M. Abraham, Studies of Li-Air Cells Utilizing Dimethyl Sulfoxide-Based Electrolyte, *J. Electrochem. Soc.*, 2013, **160**, A259.

109 C. N. Satterfield, *Heterogeneous catalysis in practice*, McGraw-Hill New York, 1980.

110 B. J. Bergner, A. Schürmann, K. Peppler, A. Garsuch and J. Janek, TEMPO: A Mobile Catalyst for Rechargeable Li-O_2 Batteries, *J. Am. Chem. Soc.*, 2014, **136**, 15054.

111 H.-D. Lim, H. Song, J. Kim, H. Gwon, Y. Bae, K.-Y. Park, J. Hong, H. Kim, T. Kim, Y. H. Kim, X. Lepró, R. Ovalle-Robles, R. H. Baughman and K. Kang, Superior Rechargeability and Efficiency of Lithium-Oxygen Batteries: Hierarchical Air Electrode Architecture Combined with a Soluble Catalyst, *Angew. Chem. Int. Ed.*, 2014, **53**, 3926.

112 S. Devaraj and N. Munichandraiah, Effect of Crystallographic Structure of MnO_2 on Its Electrochemical Capacitance Properties, *J. Phys. Chem. C*, 2008, **112**, 4406.

113 M. Risch, A. Grimaud, K. J. May, K. A. Stoerzinger, T. J. Chen, A. N. Mansour and Y. Shao-Horn, Structural Changes of Cobalt-Based Perovskites upon Water Oxidation Investigated by EXAFS, *J. Phys. Chem. C*, 2013, **117**, 8628.

114 R. Bernhard, S. Meini and H. A. Gasteiger, On-Line Electrochemical Mass Spectrometry Investigations on the Gassing Behavior of $Li_4Ti_5O_{12}$ Electrodes and Its Origins, *J. Electrochem. Soc.*, 2014, **161**, A497.

115 D. M. Itkis, D. A. Semenenko, E. Y. Kataev, A. I. Belova, V. S. Neudachina, A. P. Sirotina, M. Hävecker, D. Teschner, A. Knop-Gericke, P. Dudin, A. Barinov, E. A. Goodilin, Y. Shao-Horn and L. V. Yashina, Reactivity of Carbon in Lithium-Oxygen Battery Positive Electrodes, *Nano Lett.*, 2013, **13**, 4697.

116 R. Wang, X. Yu, J. Bai, H. Li, X. Huang, L. Chen and X. Yang, Electrochemical decomposition of Li_2CO_3 in NiO–Li_2CO_3 nanocomposite thin film and powder electrodes, *J. Power Sources*, 2012, **218**, 113.

117 R. Powell, R. Tye and M. J. Woodman, Thermal conductivities and electrical resistivities of the platinum metals, *Platinum Met. Rev.*, 1962, **6**, 138.

118 L. Krusin - Elbaum and M. Wittmer, Conducting Transition Metal Oxides: Possibilities for RuO_2 in VLSI Metallization, *J. Electrochem. Soc.*, 1988, **135**, 2610.

119 S. Tanuma, C. J. Powell and D. R. Penn, Calculations of electron inelastic mean free paths. IX. Data for 41 elemental solids over the 50 eV to 30 keV range, *Surf. Interface Anal.*, 2011, **43**, 689.

120 S. L. M. Schroeder, G. D. Moggridge, R. M. Ormerod, T. Rayment and R. M. Lambert, What determines the probing depth of electron yield XAS?, *Surf. Sci.*, 1995, **324**, L371.

121 S. Meini, S. Solchenbach, M. Piana and H. A. Gasteiger, The Role of Electrolyte Solvent Stability and Electrolyte Impurities in the Electrooxidation of Li_2O_2 in Li-O_2 Batteries, *J. Electrochem. Soc.*, 2014, **161**, A1306.

122 A. Jain, G. Hautier, S. P. Ong, C. J. Moore, C. C. Fischer, K. A. Persson and G. Ceder, Formation enthalpies by mixing GGA and GGA + U calculations, *Phys. Rev. B*, 2011, **84**, 045115.

123 K. S. Kim and N. Winograd, X-Ray photoelectron spectroscopic studies of ruthenium-oxygen surfaces, *J. Catal.*, 1974, **35**, 66.

124 F. Zhou, M. Cococcioni, C. Marianetti, D. Morgan and G. Ceder, First-principles prediction of redox potentials in transition-metal compounds with LDA+U, *Phys. Rev. B*, 2004, **70**, 235121.

125 P. Lanz, C. Villevieille and P. Novák, Electrochemical activation of Li_2MnO_3 at elevated temperature investigated by in situ Raman microscopy, *Electrochim. Acta*, 2013, **109**, 426.

126 D. Kundu, R. Black, E. J. Berg and L. F. Nazar, A highly active nanostructured metallic oxide cathode for aprotic Li–O_2 batteries, *Energy Environ. Sci.*, 2015, **8**, 1292.

127 H. Deng, P. Nie, H. Luo, Y. Zhang, J. Wang and X. Zhang, Highly enhanced lithium storage capability of $LiNi_{0.5}Mn_{1.5}O_4$ by coating with Li_2TiO_3 for Li-ion batteries, *J. Mater. Chem. A*, 2014, **2**, 18256.

128 L. Zhang and H. Noguchi, Novel Layered Li-Cr-Ti-O Cathode Materials Related to the $LiCrO_2$-Li_2TiO_3 Solid Solution, *J. Electrochem. Soc.*, 2003, **150**, A601.

129 X. Liu, Y. Lyu, Z. Zhang, H. Li, Y.-s. Hu, Z. Wang, Y. Zhao, Q. Kuang, Y. Dong, Z. Liang, Q. Fan and L. Chen, Nanotube Li_2MoO_4: a novel and high-capacity material as a lithium-ion battery anode, 2014, **6**, 13660.

130 H. Kobayashi, R. Kanno, Y. Kawamoto, M. Tabuchi, O. Nakamura and M. Takano, Structure and lithium deintercalation of $Li_{2-x}RuO_3$, *Solid State Ionics*, 1995, **82**, 25.

131 S. Sarkar, P. Mahale and S. Mitra, Lithium Rich Composition of Li_2RuO_3 and $Li_2Ru_{1-x}Ir_xO_3$ Layered Materials as Li-Ion Battery Cathode, *J. Electrochem. Soc.*, 2014, **161**, A934.

132 K. Mizushima, P. C. Jones, P. J. Wiseman and J. B. Goodenough, Li_xCoO_2 ($0<x<1$): A new cathode material for batteries of high energy density, *Solid State Ionics*, 1981, **3–4**, 171.

133 K. P. C. Yao, M. Risch, S. Y. Sayed, Y.-L. Lee, J. R. Harding, A. Grimaud, N. Pour, Z. Xu, J. Zhou, A. Mansour, F. Barde and Y. Shao-Horn, Solid-state

activation of Li_2O_2 oxidation kinetics and implications for Li-O_2 batteries, *Energy Environ. Sci.*, 2015, **8**, 2417.

134 D. Kundu, R. Black, B. Adams, K. Harrison, K. Zavadil and L. F. Nazar, Nanostructured Metal Carbides for Aprotic Li-O_2 Batteries: New Insights into Interfacial Reactions and Cathode Stability, *J. Phys. Chem. Lett.*, 2015, **6**, 2252.

135 B. D. Adams, R. Black, Z. Williams, R. Fernandes, M. Cuisinier, E. J. Berg, P. Novak, G. K. Murphy and L. F. Nazar, Towards a Stable Organic Electrolyte for the Lithium Oxygen Battery, *Adv. Energy Mater.*, 2015, **5**, 1400867.

136 D. G. Kwabi, T. P. Batcho, C. V. Amanchukwu, N. Ortiz-Vitoriano, P. Hammond, C. V. Thompson and Y. Shao-Horn, Chemical Instability of Dimethyl Sulfoxide in Lithium-Air Batteries, *J. Phys. Chem. Lett.*, 2014, **5**, 2850.

137 B. D. McCloskey, A. Valery, A. C. Luntz, S. R. Gowda, G. M. Wallraff, J. M. Garcia, T. Mori and L. E. Krupp, Combining Accurate O_2 and Li_2O_2 Assays to Separate Discharge and Charge Stability Limitations in Nonaqueous Li-O_2 Batteries, *J. Phys. Chem. Lett.*, 2013, **4**, 2989.

138 B. Kumar, J. Kumar, R. Leese, J. P. Fellner, S. J. Rodrigues and K. M. Abraham, A Solid-State, Rechargeable, Long Cycle Life Lithium-Air Battery, *J. Electrochem. Soc.*, 2010, **157**, A50.

139 J. R. Harding, C. V. Amanchukwu, P. T. Hammond and Y. Shao-Horn, Instability of Poly(ethylene oxide) upon Oxidation in Lithium-Air Batteries, *J. Phys. Chem. C*, 2015, **119**, 6947.

140 J. R. Harding, in *Chemical Engineering*, Massachusetts Institute of Technology, http://hdl.handle.net/1721.1/98707, Accessed March 20, 2016, 2015.

141 J. R. Harding, Y.-C. Lu, Y. Tsukada and Y. Shao-Horn, Evidence of catalyzed oxidation of Li_2O_2 for rechargeable Li-air battery applications, *Phys. Chem. Chem. Phys.*, 2012, **14**, 10540.

142 S. Meini, N. Tsiouvaras, K. U. Schwenke, M. Piana, H. Beyer, L. Lange and H. A. Gasteiger, Rechargeability of Li-air cathodes pre-filled with discharge products using an ether-based electrolyte solution: implications for cycle-life of Li-air cells, *Phys. Chem. Chem. Phys.*, 2013, **15**, 11478.

143 S. A. Freunberger, Y. Chen, Z. Peng, J. M. Griffin, L. J. Hardwick, F. Barde, P. Novak and P. G. Bruce, Reactions in the rechargeable lithium-O_2 battery with alkyl carbonate electrolytes, *J. Am. Chem. Soc.*, 2011, **133**, 8040.

144 M. E. de Ruiz Holgado, C. R. de Schaefer, E. L. Arancibia and M. Katz, Excess molar volumes and viscosities of binary mixtures of bis(2-methoxyl)ether (diglyme) with chloroalkanes at 298.15 K, *Fluid Phase Equilibr.*, 1994, **95**, 299.

145 P. Hartmann, D. Grübl, H. Sommer, J. Janek, W. G. Bessler and P. Adelhelm, Pressure Dynamics in Metal-Oxygen (Metal-Air) Batteries: A Case Study on Sodium Superoxide Cells, *J. Phys. Chem. C*, 2014, **118**, 1461.

146 P. Zheng, X. Meng, J. Wu and Z. Liu, Density and Viscosity Measurements of Dimethoxymethane and 1,2-Dimethoxyethane from 243 K to 373 K up to 20 MPa, *Int. J. Thermophys.*, 2008, **29**, 1244.

147 Y.-C. Lu and Y. Shao-Horn, Probing the Reaction Kinetics of the Charge Reactions of Nonaqueous Li-O_2 Batteries, *J. Phys. Chem. Lett.*, 2013, **4**, 93.

148 B. D. McCloskey, D. S. Bethune, R. M. Shelby, T. Mori, R. Scheffler, A. Speidel, M. Sherwood and A. C. Luntz, Limitations in Rechargeability of Li-O_2 Batteries and Possible Origins, *J. Phys. Chem. Lett.*, 2012, **3**, 3043.

149 F. Mizuno, S. Nakanishi, Y. Kotani, S. Yokoishi and H. Iba, Rechargeable Li-Air Batteries with Carbonate Based Liquid Electrolytes, *Electrochemistry*, 2010, **78**, 403.

150 G. M. Veith, N. J. Dudney, J. Howe and J. Nanda, Spectroscopic Characterization of Solid Discharge Products in Li–Air Cells with Aprotic Carbonate Electrolytes, *J. Phys. Chem. C*, 2011, **115**, 14325.

151 D. M. Itkis, D. A. Semenenko, E. Y. Kataev, A. I. Belova, V. S. Neudachina, A. P. Sirotina, M. Havecker, D. Teschner, A. Knop-Gericke, P. Dudin, A. Barinov, E. A. Goodilin, Y. Shao-Horn and L. V. Yashina, Reactivity of carbon in lithium-oxygen battery positive electrodes, *Nano Lett.*, 2013, **13**, 4697.

152 M. Leskes, A. J. Moore, G. R. Goward and C. P. Grey, Monitoring the Electrochemical Processes in the Lithium-Air Battery by Solid State NMR Spectroscopy, *J. Phys. Chem. C*, 2013, **117**, 26929.

153 G. A. Elia, J.-B. Park, B. Scrosati, Y.-K. Sun and J. Hassoun, Investigation of the carbon electrode changes during lithium oxygen cell operation in a tetraglyme-based electrolyte, *Electrochem. Commun.*, 2013, **34**, 250.

154 D. Sun, Y. Shen, W. Zhang, L. Yu, Z. Yi, W. Yin, D. Wang, Y. Huang, J. Wang, D. Wang and J. B. Goodenough, A Solution-Phase Bifunctional Catalyst for Lithium–Oxygen Batteries, *J. Am. Chem. Soc.*, 2014, **136**, 8941.

155 Y. G. Zhu, C. Jia, J. Yang, F. Pan, Q. Huang and Q. Wang, Dual redox catalysts for oxygen reduction and evolution reactions: towards a redox flow Li-O_2 battery, *Chem. Commun.*, 2015, **51**, 9451.

156 M. Yu, X. Ren, L. Ma and Y. Wu, Integrating a redox-coupled dye-sensitized photoelectrode into a lithium–oxygen battery for photoassisted charging, *Nat. Commun.*, 2014, **5**.

157 D. S. Kim and Y. J. Park, Effect of multi-catalysts on rechargeable Li–air batteries, *J. Alloy. Compd.*, 2014, **591**, 164.

158 T. H. Yoon and Y. J. Park, New strategy toward enhanced air electrode for Li-air batteries: apply a polydopamine coating and dissolved catalyst, 2014, **4**, 17434.

159 W.-J. Kwak, D. Hirshberg, D. Sharon, H.-J. Shin, M. Afri, J.-B. Park, A. Garsuch, F. F. Chesneau, A. A. Frimer, D. Aurbach and Y.-K. Sun, Understanding the behavior of Li-oxygen cells containing LiI, *J. Mater. Chem. A*, 2015, **3**, 8855.

160 T. Liu, M. Leskes, W. Yu, A. J. Moore, L. Zhou, P. M. Bayley, G. Kim and C. P. Grey, Cycling Li-O_2 batteries via LiOH formation and decomposition, *Science*, 2015, **350**, 530.

161 A. J. Bard and J. A. A. Ketelaar, Encyclopedia of Electrochemistry of the Elements, *J. Electrochem. Soc.*, 1976, **123**, 348C.

162 K. B. Aribia, T. Moehl, S. M. Zakeeruddin and M. Gratzel, Tridentate cobalt complexes as alternative redox couples for high-efficiency dye-sensitized solar cells, *Chem. Sci.*, 2013, **4**, 454.

163 R. R. Mitchell, B. M. Gallant, Y. Shao-Horn and C. V. Thompson, Mechanisms of Morphological Evolution of Li_2O_2 Particles during Electrochemical Growth, *J. Phys. Chem. Lett.*, 2013, **4**, 1060.

164 L. M. Moshurchak, W. M. Lamanna, M. Bulinski, R. L. Wang, R. R. Garsuch, J. Jiang, D. Magnuson, M. Triemert and J. R. Dahn, High-Potential Redox Shuttle for Use in Lithium-Ion Batteries, *J. Electrochem. Soc.*, 2009, **156**, A309.

165 G. A. Mabbott, An introduction to cyclic voltammetry, *J. Chem. Educ.*, 1983, **60**, 697.

166 I. Noviandri, K. N. Brown, D. S. Fleming, P. T. Gulyas, P. A. Lay, A. F. Masters and L. Phillips, The Decamethylferrocenium/Decamethylferrocene Redox Couple: A Superior Redox Standard to the Ferrocenium/Ferrocene Redox Couple for Studying Solvent Effects on the Thermodynamics of Electron Transfer, *J. Phys. Chem. B*, 1999, **103**, 6713.

167 H. Schneider, C. Gollub, T. Weiß, J. Kulisch, K. Leitner, R. Schmidt, M. M. Safont-Sempere, Y. Mikhaylik, T. Kelley, C. Scordilis-Kelley, M. Laramie and H. Du, On the Electrode Potentials in Lithium-Sulfur Batteries and Their Solvent-Dependence, *J. Electrochem. Soc.*, 2014, **161**, A1399.

168 S. Schaltin, G. Vanhoutte, M. Wu, F. Barde and J. Fransaer, A QCM study of ORR-OER and an in situ study of a redox mediator in DMSO for Li-O_2 batteries, *Phys. Chem. Chem. Phys.*, 2015, **17**, 12575.

169 Y. Qiao and S. Ye, Spectroscopic Investigation for Oxygen Reduction and Evolution Reactions with Tetrathiafulvalene as a Redox Mediator in Li-O_2 Battery, *J. Phys. Chem. C*, 2016.

170 H.-D. Lim, K.-Y. Park, H. Gwon, J. Hong, H. Kim and K. Kang, The potential for long-term operation of a lithium-oxygen battery using a non-carbonate-based electrolyte, *Chem. Commun.*, 2012, **48**, 8374.

171 J. Hassoun, F. Croce, M. Armand and B. Scrosati, Investigation of the O_2 Electrochemistry in a Polymer Electrolyte Solid-State Cell, *Angew. Chem.*, 2011, **123**, 3055.

172 V. Giordani, D. Tozier, H. Tan, C. M. Burke, B. M. Gallant, J. Uddin, J. R. Greer, B. D. McCloskey, G. V. Chase and D. Addison, A Molten Salt Lithium–Oxygen Battery, *J. Am. Chem. Soc.*, 2016, **138**, 2656.